博士論文

Study on CFD-based Evaluation Methods of Thermal Loading at Tee Junction for Thermal Fatigue Evaluation

（配管合流部における熱疲労評価のための熱流体数値解析による熱荷重評価方法に関する研究）

Shaoxiang Qian
（銭　紹祥）

Contents

List of Figures

List of Tables

Nomenclature

c_p	Specific heat at constant pressure [J/(kg·K)]
D_b	Internal diameter for branch pipe [m]
D_m	Internal diameter for main pipe [m]
k	Turbulent kinetic energy [J/kg]
h	Enthalpy [J/kg]
M_b	Momentum of branch pipe flow interacting with main pipe flow [kg.m/s^2]
M_m	Momentum of main pipe flow interacting with branch pipe flow [kg.m/s^2]
M_R	Interacting momentum ratio of main pipe flow to branch pipe flow [-]
n	Parameter in power-law velocity profile of fully developed turbulent pipe flow [-]
p	Pressure [Pa]
Pr	Prandtl number [-]
Pr_T	Turbulent Prandtl number [-]
R	Internal radius of a pipe [m]
Re	Reynolds number based on the averaged velocity [-]
t	Time [sec]
T	Temperature [^{o}C]
T_b	Fluid temperature at inlet of branch pipe [^{o}C]
T_m	Fluid temperature at inlet of main pipe [^{o}C]
u	Time-averaged velocity at a distance of y from pipe wall for pipe inlet [m/s]
u_i	Component of flow velocity (i=1, 2, 3) [m/s]
u_{max}	Time-averaged velocity at the center of pipe inlet [m/s]
V_b	Mean flow velocity at inlet of branch pipe [m/s]
V_m	Mean flow velocity at inlet of main pipe [m/s]

x_i	Coordinates (i=1, 2, 3) [m]
y	Distance from the center of a cell to the nearest pipe wall [m]
y^+	Dimensionless distance from the center of cell to the nearest pipe wall [-]
y_F^+	Dimensionless thickness of the flow boundary sub-layer [-]
y_T^+	Dimensionless thickness of the thermal boundary sub-layer [-]

Greek symbols

α	Angle between main pipe and branch pipe [Deg.]
α_{bf}	Blending factor [-]
ε	Turbulent kinetic energy dissipation rate [J/(kg·s)]
λ	Thermal conductivity [J/(m·K·s)]
λ_T	Turbulent thermal conductivity [J/(m·K·s)]
μ	Fluid viscosity [kg/(m·s)]
μ_T	Turbulent eddy viscosity [kg/(m·s)]
ρ	Fluid density [kg/m^3]
ρ_b	Fluid density at inlet of branch pipe [kg/m^3]
ρ_m	Fluid density at inlet of main pipe [kg/m^3]

Superscripts

$\overline{q}$	Time- or space-averaged value of any quantity q
q'	Fluctuation of any quantity q

Chapter 1 Introduction

1-1 High Cycle Thermal Fatigue

T-junctions are widely used to mix fluids of different temperatures in nuclear power plants, and process plants including chemical plants and refineries and liquefied natural gas (LNG) plants. However, incomplete mixing of hot and cold fluids at T-junction can produce random fluid temperature fluctuations that may cause high cycle thermal fatigue (HCTF) failure of piping, which is also called thermal striping [1] [2] [3] [4] [5]. Thermal striping phenomena are very complicated and, include the turbulent mixing of fluids with different temperatures, attenuation of heat transfer from fluid to structure, repetition of thermal stresses in structure, initiation and propagation of thermal fatigue cracks [6]. Therefore, these phenomena involve multiple disciplines such as thermo-hydraulics, thermo-mechanics, fracture mechanics and material science [7] [8].

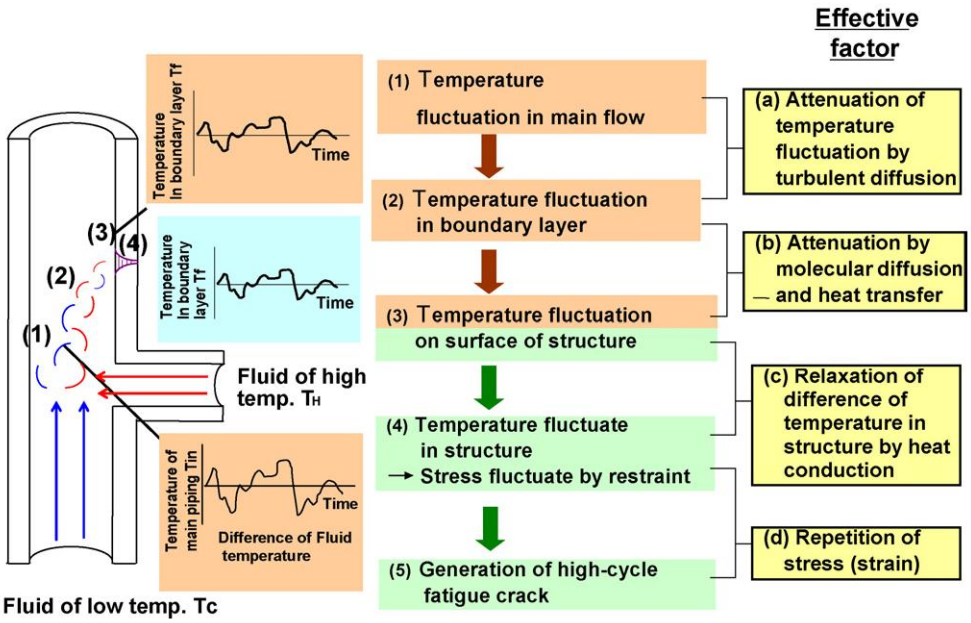

Fig. 1-1 Mechanism of High Cycle Thermal Fatigue Induced by Fluid Temperature Fluctuation at Tee Junction [9]

Kasahara et al. [6] and Shibamoto et al. [9] investigated in detail the mechanism of HCTF induced by random fluid temperature fluctuations, which contributes to the sound understanding

of thermal striping phenomena. As shown in **Fig. 1-1**, the process of HCTF failure can be considered to comprise 5 steps. Random fluid temperature fluctuations (FTF) induced by incomplete mixing of hot and cold fluids at first take place in the fluid bulk and then transfer to the boundary layer. Further, temperature fluctuations are transferred to the pipe wall through heat transfer between fluid and pipe, and to pipe structure through thermal conduction. Hence, thermal stress fluctuations occur in structure due to constraint and eventually high cycle fatigue crack may initiate. In addition, it should be noted that, as demonstrated in (a)-(c), attenuation of temperature fluctuation occurs during each phase from step (1) through step (4). As a result, the temperature fluctuations in structure may be attenuated significantly. **Fig. 1-2** shows a typical example of attenuation of the structure temperature fluctuations during heat transfer from fluid to structure [10].

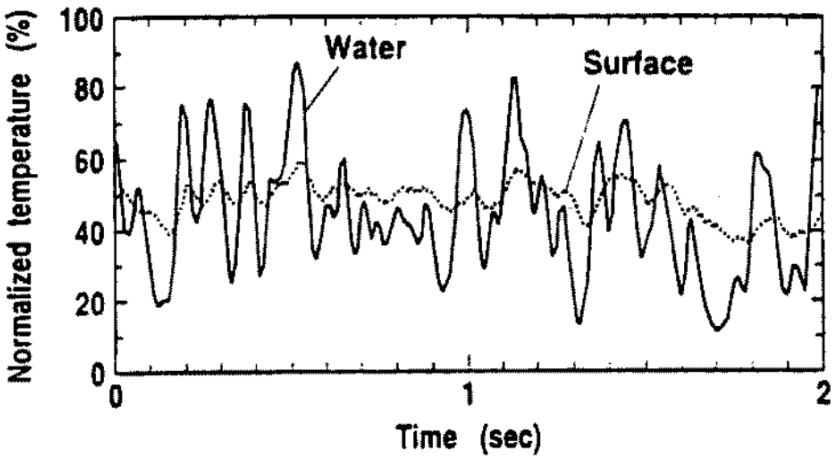

Fig. 1-2 A Typical Example of Attenuation of Structure Temperature Fluctuations [10]

At the same time, Kasahara et al. [6] and Shibamoto et al. [9] also found that the attenuation of structure temperature fluctuations (STF) closely depends on the frequency of fluid temperature fluctuations (FTF). As shown in **Fig. 1-3**, the heat conduction tends to make the temperature in the structure uniform and thus the temperature through the entire thickness of pipe wall can respond to fluid temperature, if the FTF frequency is very low. Therefore, only a small temperature gradient across the wall thickness is produced and hence no large thermal stress is induced in structure. On the other hand, a structure cannot respond to an FTF with very high

frequency, as the structure has an inherent time constant of thermal response. Hence, very high frequency fluctuations do also not induce large thermal stress in structure. As a result, there is an intermediate frequency range that induces very large thermal stress. It is considered that the intermediate frequency range corresponds to the inherent time constant of thermal response for structure. The finding of such frequency effect is very helpful for understanding the thermal striping phenomena and investigations of thermal fatigue evaluation methods.

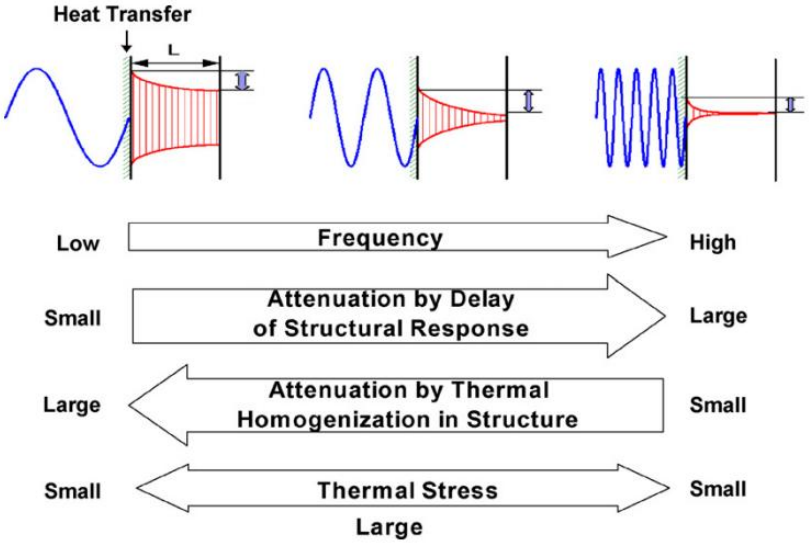

Fig. 1-3 Frequency Response Characteristics of Structure to Fluid Temperature Fluctuation [9]

1-2 Examples of Thermal Fatigue Failure

There have been many reports of thermal fatigue incidents in nuclear power plants (NPP). Jungclaus et al. [11] listed many examples of thermal fatigue incidents that had occurred in pressurized water reactors (PWR) up until that time, including Farley 2 (1987, US), Tihange 1 (1988, Belgium), Dampierre 2 (1992, France), Loviisa 2 (1997, Finland) and so on. Also, some leakage incidents caused by thermal striping occurred in liquid-metal-cooled fast breeder reactors (LMFBR), such as French Super Phenix in 1990 and Phenix in 1992 [12]. Recently, there occurred coolant leak incidents in the French PWR Civaux 1 in 1998 [13], and the Japanese PWR Tsuruga-2 in 1999 and Tomari-2 in 2003 [14] [15]. As a typical example in the NPP incidents, the French PWR Civaux 1 incident occurred in the residual heat removal (RHR) system. As shown in

Fig. 1-4, the hot coolant stream from the horizontal branch pipe met the cold coolant stream flowing upwards at tee junction and then a mixing zone was formed near the extrados of the immediate downstream elbow, where large and random fluid temperature fluctuations caused large structural temperature fluctuation in the elbow part. As a result, a 180mm long penetrating crack was generated on the extrados of the elbow and consequently a coolant leak occurred. [16].

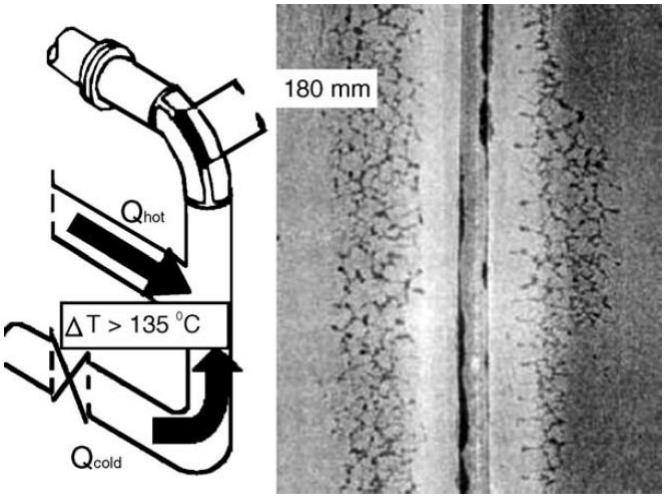

Fig. 1-4 Thermal Fatigue Crack in the Incident of French PWR Civaux 1 [16]

Maegawa [17] also reported a pipe rupture due to thermal fatigue in a refinery plant, which took place downstream of a T-junction used for mixing quench hydrogen (80°C) with hot feed gas (400°C), as shown in **Fig.1-5**. The hot effluent exiting the first-stage hydro-cracking reactor was first mixed with the cold quench hydrogen from a branch pipe and then fed into the second-stage hydro-cracking reactor. In this case, the flow pattern was wall jet and hence the mixing of the effluent and the quench hydrogen occurred near the pipe wall at the branch side. The large fluid temperature fluctuations caused by the fluid mixing were transferred to the pipe wall. As a result, a pipe rupture occurred and led to leakage.

In addition, only within the present author's knowledge, there are many unpublished examples of thermal fatigue failure in process plants, including LNG plants, refineries and petrochemical plants. **Table 1-1** showed some examples of thermal fatigue failure in such process plants. Furthermore, there are many unpublished reports of equipment on the brink of thermal fatigue failure, where thermal fatigue cracks were found during turnaround (TA) or regular shut-down

maintenance (SDM) and fortunately the relevant parts were repaired or replaced before failure could occur. Therefore, it is necessary to evaluate the integrity of in-service and newly designed structures where the potential HCTF may occur.

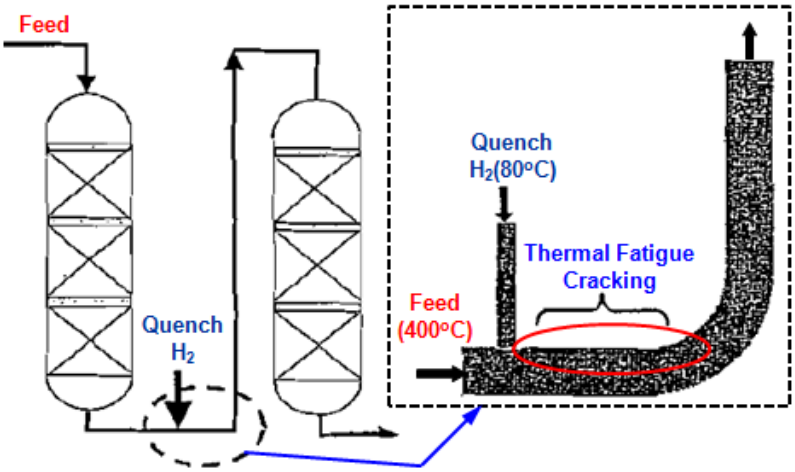

Fig. 1-5 Pipe Rupture due to Thermal Fatigue Crack in a Refinery Plant [17]

Table 1-1 Some Examples of Thermal Fatigue Failure in Process Plants

Case No.	Type of Plant	Type of Fluid		Fluid Temperature [°C]			Pipe Material	Failure Location
		Main Pipe	Branch Pipe	T_m	T_b	ΔT		
1	LNG	Vapor	Vapor	320	21	299	SS304H	Weld
2	Refinery	H2(Vapor) + VGO(Liquid)	H2	398	79	319	SUS	Weld
3	Ethylene	Steam	Naphtha	500	150	350	Incoloy 800H	Weld
4	Petro-chemical	Ethane Gas	Steam	560	170	390	SS321	Parent Mat.
5		Vapor	Vapor	370	215	155	SS321	Weld
6		Water	Water	135	31	104	SS304L	Weld /Parent Mat.

1-3 Past Studies of High Cycle Thermal Fatigue

1-3-1 Jet in Crossflow

At first, the past studies of transverse jets in crossflow are briefly reviewed, as the flow patterns at T-junctions are very similar to those for transverse jets in cross flow [18] [19]. To date, a lot of

studies on transverse jets in cross flow have been performed through experiments and numerical simulations. Fric et al. [20] investigated the vortex structure in the wake of a transverse jet. As shown in **Fig. 1-6**, four different types of coherent vortex structure were confirmed: the counter rotating vortex pair, the horseshoe vortex, the jet shear layer vortices and the wake vortices. Blanchard et al. [21] studied the influence of the counter rotating vortex pair on the stability of a jet in a crossflow by flow visualizations. They showed that a counter rotating vortex pair with elliptical cross-sections can cause the instability of the jet, according to the theory of Landman et al. [22]. The experimental study of Kelso et al. [23] showed that the horseshoe vortex system can be steady, oscillating, or coalescing, depending on the flow conditions. Also, it was found that the Strouhal numbers of the observed oscillating and coalescing systems for a round transverse jet agree reasonably well with those for wall-mounted circular cylinders.

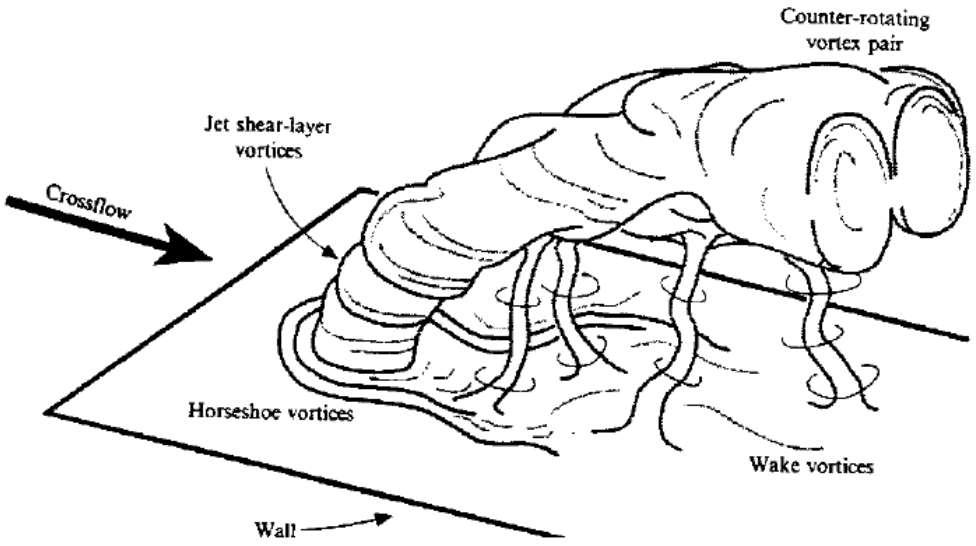

Fig. 1-6 Schematic Diagram of the Flow Structure of a Jet in Crossflow [20]

Recently, CFD simulations, especially large-eddy simulations (LES), have also been widely applied for investigations of the flow structure of jet in crossflow. Yuan et al. [24] preformed a series of LES simulations of a round jet in crossflow. Simulations were performed at two jet-to-crossflow velocity ratios and two Reynolds numbers, based on crossflow velocity and jet diameter. Simulation results for mean and turbulent statistics match experimental measurements reasonably well. Large-scale coherent structures observed in experimental flow

visualizations were reproduced by the simulations, and the mechanisms for formation of these structures were revealed. Schluter et al. [25] reported that the counter rotating vortex pair, the horseshoe vortex and the jet shear layer vortices of jets in crossflow were reproduced through LES simulations. Majander et al. [26] also performed the LES-based simulations of a round jet in a crossflow and reproduced the shear layer ring vortices and the counter-rotating vortex pair well.

Mahesh and his group performed many investigations of a jet in crossflow using direct numerical simulations (DNS). For example, Babu and Mahesh [27] studied the effect of entrainment near the inflow nozzle on spatially evolving round jets using DNS. The results suggest that the consideration of inflow entrainment for turbulent jets is important. Also, Muppidi and Mahesh [28] investigated the trajectories and near field of round jets in crossflow using DNS. The simulations were performed at velocity ratios of 1.5 and 5.7, and the effects of jet velocity profile and boundary layer thickness on the jet trajectory are examined. As well, Muppidi and Mahesh [29] used DNS to study a round turbulent jet in a laminar crossflow. The simulation results agreed well with the available experimental results. Some additional data, not available from experiments, were presented. They included the locations of peak kinetic energy production and peak dissipation, and the existence of region dominated by pressure transport. In addition, Sau and Mahesh [30] investigated the effect of crossflow on the dynamics, entrainment and mixing characteristics of vortex rings of jet exiting a circular nozzle using DNS.

1-3-2 Thermal Striping for Liquid Metal Cooled Fast Breeder Reactors

Thermal striping phenomena in liquid metal cooled fast breeder reactors (LMFBRs) were already perceived in the early 1980s by Wood [1] and Brunings [2] and hence, studies of thermal striping were initially undertaken for LMFBRs from that time on. The fluid temperature fluctuations are transferred to structure with a relatively small attenuation due to the high thermal conductivity of liquid metal coolant in LMFBR [4] [10]. In the core outlet region of LMFBR, the components vulnerable to thermal striping include core upper plenum, flow guide tube and control rod upper guide tubes. Outside the core region, the components, where mixing of

hot and cold streams occurs, may also easily be affected. They include tee junctions, elbows, and valves with leakage. Subsequently, leakage incidents induced by thermal striping occurred in LMFBRs of French Super Phenix in 1990 and Phenix in 1992 [14]. In view of this, many studies of thermal striping in LMFRBs were carried out through experiments, analytical methods and numerical simulations.

The effects of different fluids (sodium, water and air) on the temperature fluctuations induced by turbulent mixing were studied in experiments by Kasza and Colwell [31] in mixing tee, by Betts et al. [32] in PFR scale test model and by Wakamatsu et al. [33] in coaxial jet tests. Also, the effects of dimensionless parameters (Reynolds number and Pelect number) on the temperature fluctuations were investigated by Moriya and Ohshima [34] through experiments using sodium, water and air. Tokuhiro and Kimura [35] carried out a water experiment with vertical, parallel triple-jet configuration and evaluated the effects of discharge velocities and temperature difference on convective mixing by jets using ultrasound Doppler velocimetry and thermocouples. Tenchine and coworkers [36] [37] [38] [39] [40] carried out a series of co-axial jet experiments using air and water and sodium as working fluids, and found that air tests can be used to predict temperature fluctuation behavior in a sodium reactor.

JAEA constructed SPECTRA test facility, which was designed to generate temperature fluctuation in liquid sodium in a T-junction of the test section and initiate cracks on the inner surface of the test section [41]. The SPECTRA loop can generate sinusoidal temperature fluctuation in sodium with constant flow velocity. The high (525ºC) and low (325ºC) temperature liquid sodium flows alternately into the test section made of 304 type stainless steel, with a pipe thickness of 4.7mm at test section inlet and 11.1mm at outlet. Umaya et al. [42] carried out the CFD benchmark simulations using three different turbulence models ($k-\varepsilon$, SST and DES), based on the SPECTRA experimental results.

Additionally, CEA and JNC [43] built the facilities, FAENA and TIFFSS, for thermal fatigue experiments under the framework of CEA/JNC cooperation in fast reactor technologies, aiming to develop evaluation procedures for thermal striping based on design-by-analysis methodologies.

Also, Fukuda et al. [44] investigated crack propagation and arrest behavior under thermal striping load through experiments, using liquid sodium as working fluid.

For investigating the thermal hydraulic behavior for thermal striping, Muramatsu et al. developed numerical methods [45] [46] [47] and evaluated thermal hydraulics and heat transfer from fluid to structure [48] [49]. The numerical results showed that attenuation of temperature fluctuations occurred during heat transfer process from the fluid to the structure. Such temperature fluctuation attenuation has large effects on fatigue damage [50]. Nishimura et al. [51] simulated the mixing behavior of triple-jet using low Reynolds number turbulence stress and heat flux equation model (LRSFM) [52], which modeled turbulence near structure based on a database constructed by direct numerical simulation (DNS). Kimura et al. [53] performed a water experiment using vertical and parallel triple-jet with a cold jet at the center and hot jets in both sides to investigate the convective mixing behavior. Meanwhile, three kinds of calculations based on the finite difference method (FDM) were carried out. Two types of turbulence models used were the k-ε two-equation turbulence model and LRSFMs. Additionally, a quasi-direct numerical simulation was also performed. The DNS could simulate the time-averaged temperature field. The prominent frequency in temperature fluctuation obtained by the LRSFM was in good agreement with that in the experiment. The profile of power spectrum density of temperature fluctuations calculated by the DNS was close to the experimental results. Choi and Kim [54] performed the CFD predictions of thermal striping in a triple jet using three RANS-based turbulence models, which included the two-layer model, the shear stress transport (SST) model and the V2-f model. The results showed that the former two models could not predict the fluid temperature fluctuations well, and only the last model was capable of predicting the behavior of fluid temperature fluctuations better. However, this model predicted a slower mixing far downstream of the jet. Velusamy et al. [55] also undertook the thermal striping studies of LMFRB using CFD simulation in two steps. They first made CFD benchmark investigations and then performed CFD simulations for the real reactor. However, the conjugate heat transfer between fluid and structure was not done in the CFD simulations. The calculation of heat conduction was

implemented using a separate in-house program, based on the obtained fluid temperature and an empirical equation of heat transfer coefficient.

The analytical models were also proposed by some researchers, to investigate the transfer characteristics of temperature fluctuation from fluid to structure and the behaviors of thermal fatigue failure in structure for thermal striping. For the former, Moriya [56] proposed two methods of predicting metal surface temperature fluctuation from fluid temperature fluctuation data – "Improved Time Range Method" and "Frequency Range Method" using the effective heat transfer coefficient predicted by the power spectrum method. The prediction accuracy of these two methods was investigated using parallel impinging jet test data. It was found that the metal temperature fluctuations predicted by both of two methods were close to the corresponding experimental data, and hence, the validity of the methods was confirmed. No significant difference in prediction accuracy was found between the two methods. For the latter, an analytical model is presented for the assessment of thermal fatigue damage, based on linear elastic fracture mechanics and the frequency response method. The power spectral densities of temperature-time histories for various shapes of surface were examined. The model was compared with the impulse response method and good agreement is found [57]. This model was further developed to investigate the effects of various plate-constraint conditions for thermal striping [58] and assess thermal striping of cylindrical geometries [59]. A comparison between the finite element and frequency response methods was also made for the assessment of thermal striping damage and good agreement was found [60]. An impulse response method was also presented for assessing thermal striping fatigue damage in flat plates and thin cylinders [61] and applied to the analysis of the thermally striped internal surface of a hollow cylinder containing a circumferential crack on this surface [62]. Additionally, Jones [63] assessed the stress intensity factor (SIF) fluctuations induced by thermal striping for single edge-cracked and multiple edged-cracked geometries based on fracture mechanics, and showed that the results single edge-cracked geometries were overly conservative relative to those for multiple edged-cracked geometries. Kasahara et al. [64] [65] [66] proposed a structural response diagram approach to evaluate thermal striping fatigue

phenomena. This approach was applied to conduct structural analysis for investigating possibility of crack initiation and propagation induced by thermal striping for a tee junction of the PHÉNIX secondary circuit [67]. Attenuation of temperature fluctuations occurs during heat transfer process from fluid to structure [49] and consequently has an effect of mitigating thermal striping fatigue damage [50]. Kasahara [68] proposed a frequency response approach, where the effective heat transfer function was developed, for evaluating temperatures on the structural surfaces induced by fluid temperature fluctuation. This approach was applied to evaluate thermal striping fatigue of cylinders and plates subjected to fluid temperature fluctuations [43].

In addition, Meshii and Watanabe [69] investigated the normalized stress intensity factor (SIF) range of an inner-surface circumferential crack in a thin- to thick-walled finite-length cylinder under thermal striping. The inner surface of the cylinder was heated by a fluid with sinusoidal temperature fluctuation and the outer surface was adiabatically insulated. An analytical temperature solution for the problem and semi-analytical numerical SIF evaluation method for the crack were combined. The results showed that the transient SIF solution can be expressed in a generalized form by dimensionless parameters such as mean radius to wall thickness ratio, Biot number, normalized striping frequency and Fourier number. They also analyzed transient SIF range of a circumferential crack in a finite-length thick-walled cylinder under thermal striping load [70]. The results showed that the maximum SIF range decreases monotonously when crack depth becomes deeper than a specific value, which corresponds to the crack arrest tendency. Lee et al. [71] carried out the crack propagation analysis of the mixing tee for LMFBR secondary piping under thermal striping load using Green's function method (GFM). The analysis results were in agreement with the actual observation for piping structure subjected to thermal striping load.

1-3-3 Thermal Striping for Light Water Reactors

Subsequently, there occurred several piping failure incidents, which were induced by thermal striping and led to coolant leak incidents for light water reactors (LWRs), for example, the French PWR Civaux 1 in 1998 [11], and the Japanese pressurized water reactor (PWR) Tsuruga-2 in 1999

[12]. As a result, the focus of thermal striping studies shifted to LWRs. A lot of studies of thermal striping for LWRs have been carried out through the experiments, numerical simulations and analytical methods.

Following a leak of primary coolant from a pipe in the residual heat removal (RHR) system, a large research program was started to reveal the root causes of thermal fatigue failure in France. For example, Chapuliot et al. [6] carried out the overall analysis of thermal-hydraulic and thermo-mechanical behaviors for the complex 3D geometry of the Civaux 1 RHR system, which includes a mixing tee and bends and straight sections. The numerical simulations were performed using a single computer code CAST3M developed by the CEA, in order to evaluate the thermal loading caused by turbulent mixing at tee junctions and understand the mechanism of initiation and propagation of thermal fatigue cracks. However, the thermal-hydraulic and thermo-mechanical analyses were performed separately, and moreover, a constant was used for the heat transfer coefficient between fluid and structure. Also, Pasutto et al. [72] implemented the LES analysis of a mock-up T-junction using EDF's in-house CFD code Code_Saturne coupled with the finite element code Syrthes for thermal analysis of structure. Different meshes and LES subgrid-scale turbulence models (Smagorinsky and dynamic) were used in their study. The simulation results for the fluid temperature agree with the mock-up measurements well. The Smagorinsky model had difficulties dealing with the reattachment after the flow separation. The dynamic model shows a more uniform behavior, but remarkably overestimates the temperature fluctuations at the wall and the temperature in the lower part of the mixing zone. At the fluid-structure interface, heat transfer from the fluid to the wall was taken into account by standard wall functions (or log law). Although they seem to work quite well in some parts of the flow, they significantly overestimate the attenuation of the temperature fluctuations for the fluid-structure heat transfer in specific areas, like the recirculation zone, leading to a large error in structure temperature fluctuations. In addition, Taheri [73] gave an explanation of thermal crazing of some RHR systems in nuclear power plants through the analysis of observed phenomena and numerical simulations.

T-junction mixing experiments have been conducted at a number of facilities in Japan and Europe (France, Germany, Sweden and Switzerland). Of them, the three well-known facilities are the Water Experiment on Fluid Mixing in T-pipe with Long Cycle Fluctuation (WATLON) facility in Japan [74], the Vattenfall facility in Sweden [75] and the mixing tee test facility at Swiss Federal Institute of Technology in Zurich (ETHZ), Switzerland [76]. The experimental data obtained in these facilities were extensively used for the benchmark studies. Especially, the data for the tests carried out in November 2008 at the Vattenfall facility became available, and were used for the OECD/NEA international blind CFD benchmarking exercise in many countries [77]. Smith [78] summarized the CFD benchmarking activities for nuclear reactor safety (including thermal fatigue issue), which were jointly sponsored by OECD/NEA and IAEA.

WATLON: Igarashi et al. [74] carried out the water experiments to investigate thermal striping phenomena in a T-junction, as shown in **Fig. 1-7**. The influence of flow velocity ratios and temperature differences were investigated. The parametric experiments showed that the flow patterns at T-junction could be classified into four types: (1) impinging jet, (2) deflecting jet, (3) re-attachment jet and (4) wall jet based on a momentum ratio between the two pipes. The measured results for fluid temperature showed that the temperature fluctuation intensity was high along the edge of the jet exiting from branch piping. A database of temperature fluctuation and frequency characteristics was established for an evaluation rule of thermal striping at T-junction. The results for velocity measurement showed that the vortices like Karman vertex were generated in the wake region behind the branch pipe jet for the wall jet case [18]. The prominent frequency of temperature fluctuation was closely related to the frequency of vertex-shedding. Igarashi et al. [79] also investigated thermal striping phenomena in a mixing tee through another water experiment. The measured results showed that, for the transfer of temperature fluctuation from fluid to structure, higher frequency component was greatly attenuated. Additionally, a constant heat transfer coefficient was applied to the prediction of transfer function.

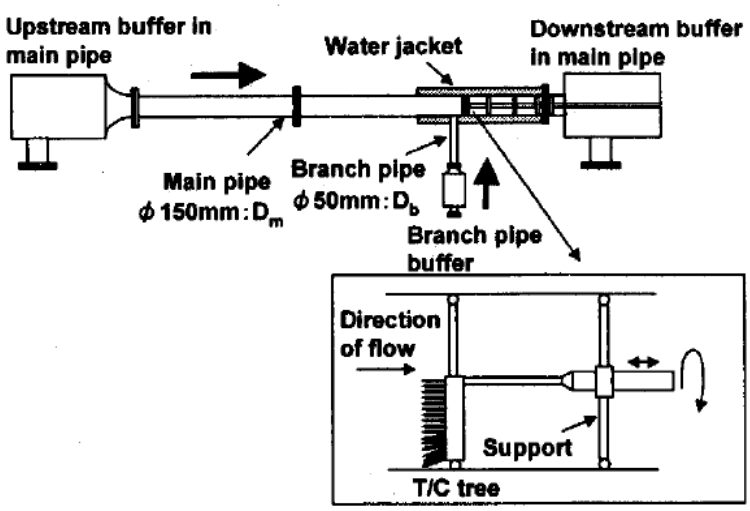

Fig. 1-7 Schematic of Test Section for T-Junction [18]

Kimura et al. [80] performed the experiments in the Water Experiment on Fluid Mixing in T-pipe with Long Cycle Fluctuation (WATLON) facility to investigate the influence of upstream elbow in the main pipe. Temperature distribution in the mixing tee was measured using a movable thermocouple tree and velocity field was measured by high speed PIV. The measured results showed that the temperature fluctuation intensity near the wall was larger in a case with the elbow than that in a straight pipe for a wall jet condition, and biased flow velocity distribution and fluctuation occurred, as the elbow affected bending of branch pipe jet and the temperature fluctuation intensity around the jet. Tanaka et al. [81] [82] performed simulations of flow and temperature at T-junctions using a very large eddy simulation (VLES) approach, in which an LES model is combined with the wall function for the coarse mesh. The results suggested the possibility of reproducing the fluid temperature fluctuations using an LES model.

Kamide et al. [83] carried out the investigation into the temperature fluctuations of water by making a series of tests using the WATLON apparatus. They also performed the numerical simulations under the same conditions as the WATLON tests using their in-house AQUA code, and the results for velocity and temperature distribution exhibited good agreement with the experimental ones. Kamaya et al. [84] and Miyoshi et al. [85] implemented thermal fatigue analysis through fluid-structure coupling simulations for the T-junction used in the WATLON experiment. Flow and thermal interaction between fluid and structure were simulated using

detached eddy simulation (DES) [86]. The T-junction was made from acrylic resin for visualizing the flow, but the simulation was performed virtually assuming a stainless pipe with 7.1 mm wall thickness. Heat transfer between fluid and pipe wall was solved using the wall functions. However, no experimental data for structure temperature were provided for verifying the accuracy of CFD-predicted structure temperature. The time series data of structure temperature obtained by CFD simulation were used to carry out thermal stress analysis and then, the obtained thermal stress was further used to evaluate thermal fatigue.

Kimura et al. [87] conducted a water experiment of T-junction in the WATLON facility to evaluate the transfer characteristics of temperature fluctuation from fluid to structure. In the experiment, temperatures in fluid and structure were measured simultaneously at 20 positions to obtain spatial distributions of the effective heat transfer coefficient. In addition, temperatures in structure and local velocities in fluid were measured simultaneously to evaluate the correlation between the unsteady temperature and velocity fields. The large heat transfer coefficients were registered in the regions with the high local velocity. Moreover, it was found that the heat transfer coefficients were correlated with the time-averaged turbulent heat flux near the pipe wall.

Vattenfall: Westin et al. [88] carried out the experiments in a 2/3-scale model of a typical T-junction in a nuclear power plant, as shown in **Fig. 1-8**. Temperature fluctuations were measured near the pipe walls by means of thermocouples for three different flow rate ratios between the hot and cold waters. Meanwhile, thermal mixing in the T-junction was studied for validation of CFD simulations. The CFD results showed that both steady and unsteady RANS failed to predict the experimental results. On the other hand, the results were significantly better with scale-resolving methods such as LES and DES, showing fairly good predictions of the mean temperatures near the wall. However, the CFD simulations predicted larger fluctuations than observed in the model tests, and the predicted frequencies were also different from the tests. The CFD results for grid refinements showed that more small-scale fluctuations appeared in the calculated flow fields, although the predicted mean and temperature fluctuations near the walls were only moderately affected. Also, the LES prediction results showed good agreement with the

experimental data even using fairly coarse meshes [89]. However, grid refinement studies revealed a fairly strong sensitivity to the grid resolution, and a simulation using a fine mesh with nearly 10 million cells significantly improved the results in the entire flow domain. The DES-based simulations improved the near-wall velocity predictions, but failed to predict the temperature fluctuations due to the over-evaluated turbulent viscosity that damped temperature fluctuation.

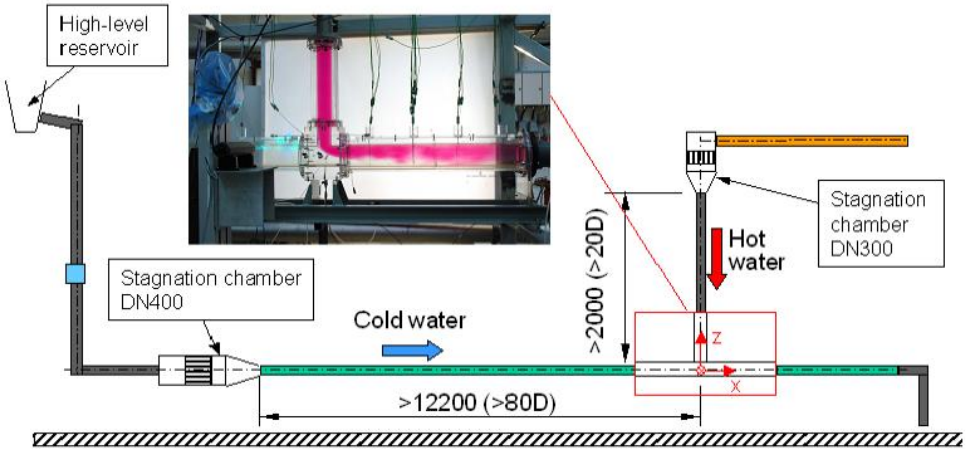

Fig. 1-8 Side View of the Test Rig with a Photo of the Test Section [89]

Jayaraju et al. [90] performed LES based benchmark simulations in a T-junction of Vattenfall facility [88] to confirm whether the wall-functions are capable of accurately predicting the thermal fluctuations acting on the pipe walls. The wall-function based simulation showed good agreement with the wall-resolved LES and the experimental results for the bulk velocity and temperature field, but the corresponding RMS components were consistently under-estimated near the wall boundaries. Kuczaj et al. [91] made an assessment of the accuracy of LES predictions for T-junction using Vreman subgrid-scale turbulence model [92] through a direct comparison with the experimental results. It is shown that the mesh resolution with the average cell-sizes three times smaller than the Taylor micro-scale length is sufficient to give very similar results to these obtained on much finer meshes. Hence, it is recommended that this may serve as an initial engineering guideline for construction of computational meshes that allow for an accurate prediction of turbulent mixing. Also, Kim et al. [93] performed LES simulation at the conditions of

Vattenfall experiment to investigate the phenomena of turbulent mixing affecting the thermal fatigue in a T-junction, based on the dynamic Vreman SGS turbulence model. LES results show that mean velocity turbulence intensity, and Reynolds shear stress profiles agree well with those measured in the Vattenfall experiment. However, the simulation of temperature fields was not made in their investigation.

Obabko et al. [94] performed the OECD/NEA blind benchmark simulations of T-junction thermal striping problem using three computational fluid dynamics codes CABARET, Conv3D, and Nek5000, which utilize finite-difference implicit large eddy simulation (ILES), finite-volume LES on fully staggered grids, and an LES spectral element method (SEM), respectively. The simulation results for flow velocity field are in a good agreement with experimental data. They also presented results from a study of sensitivity to computational mesh and time integration interval. Also, Ayhan et al. [95] joined the OECD/NEA blind benchmark exercise and performed CFD predictions of the frequency of velocity and temperature fluctuations in the mixing region of T-junction using RANS and LES models. CFD results were compared with the experimental results. Predicted LES results agree well with the experimental results for the amplitude and frequency of temperature and velocity fluctuations, even using relatively coarse mesh. The results for the power spectrum densities (PSD) of temperature fluctuations show that the peak frequency is within 2-5 Hz, which is characteristic for thermal fatigue. Hohne [96] also carried out CFD validation simulations as a part of the OECD CFD benchmark exercise, using the data of T-junction thermal mixing test at Vattenfall in Sweden. The simulation results showed that RANS SST model failed to predict the mixing phenomena between two fluids with different temperature. However, the CFD results for LES WALE simulation were significantly better and showed fairly good predictions of the velocity field and mean temperatures. The LES simulation also predicted similar fluctuations and frequencies observed in the model test.

ETHZ: Zboray and his colleagues [69] [97] carried out the mixing experiments of T-junction using wire-mesh sensors in a test facility, as shown in **Fig. 1-9**, at the Laboratory for Nuclear Energy Systems, Institute for Energy Technology, ETH Zurich, Switzerland. The main and branch

pipes were supplied by waters with different electrical conductivity, which replaced the temperature in the thermal mixing process. Besides the measurement of profiles of the time averaged mixing scalar over extended measuring domains, the high resolution in time and space of the mesh sensors allowed a statistic characterization of the stochastic fluctuations of the mixing scalar in a wide range of frequencies. Information on the scale of turbulent mixing patterns was obtained by cross-correlating the signal fluctuations recorded at different locations within the measuring plane of a sensor.

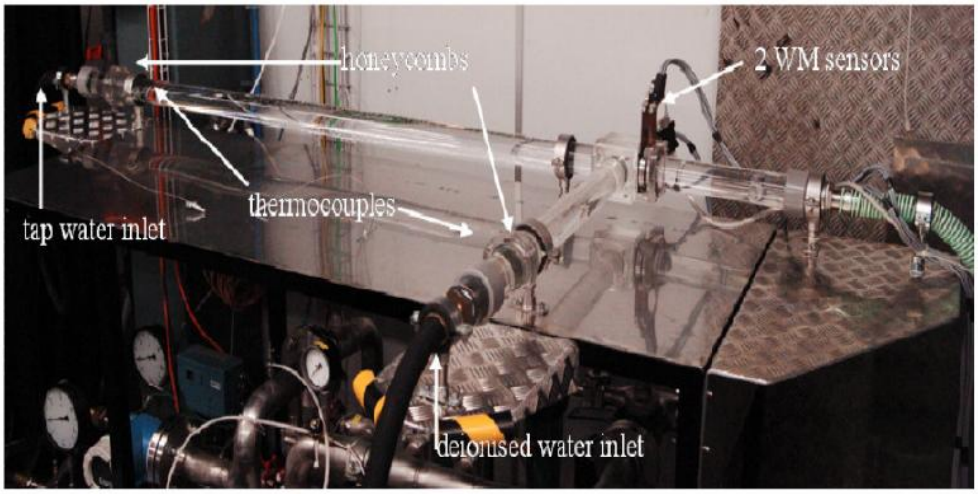

Fig. 1-9 Mixing-Tee Test Facility of ETHZ [76]

Manera et al. [98] made an attempt to predict temperature fluctuations using the steady-state RANS simulations by solving the Reynolds stress equations together with a transport equation for the temperature fluctuations. However, the CFD simulations could not reproduce the experimentally measured temperature fluctuations. Frank et al. [99] undertook the CFD investigations for two different experimental tests, which are the ETHZ test by Prasser et al. [76] and the Vattenfall test by Westin et al. [88] respectively. The RANS turbulence models of SST and BSL RSM) as well as the scale-resolving SAS-SST turbulence model were used in the CFD simulations. The turbulent mixing in the ETHZ test case could be reproduced in good quantitative agreement with the experimental data. The LES-like simulation results could not reproduce the detailed measurement data well, although the transient thermal striping phenomena and large-scale turbulence structure development were well reproduced in the simulations. Li et al.

[100] carried out the CFD simulation of T-junction in the ETHZ experiment using the commercial CFD code ANSYS CFX 11.0. It was shown that different turbulence models (BSL-RSM, $k-\varepsilon$) and different turbulent Prandtl number affected the simulation results of temperature fluctuations. The computational results are in qualitative good agreement with experimental data. For smaller turbulent Prandtl number, the predictions are in good agreement with measurements.

In addition, Tanaka et al. [101] performed the experimental investigation of thermal striping phenomena in a simplified T-junction piping system using water. T-junction comprised a rectangular duct for main stream and a circular pipe for branch stream, and was made of acrylic resin for visualization. Time series of instantaneous two-dimensional velocity fields were obtained by PIV in the mixing area, and fluid temperature fluctuation at several positions being 2 mm away from the wall were also measured by thermal-couples. Focusing on the frequency characteristics, formation of eddy structure in the mixing area and mutual relation between the temperature fluctuation generation and the flow structure were presented. Tanaka et al. [102] [103] also carried out the water experiment in the simplified T-junction piping system, where a part of rectangular duct around and downstream of the branch was changed from acrylic resin to aluminum plate for measuring both fluid and structure temperatures. At the same time, LES simulations were also performed for thermal interaction between fluid and structure using standard Smagorinsky model and the wall functions. Tanaka [104] implemented verification and validation (V&V) studies of an in-house CFD code MUGTHES, which comprises two analysis modules for unsteady thermal-hydraulics analysis and unsteady heat conduction analysis in structure, based on the existing V&V guidelines. The V&V study was conducted in fundamental laminar flow problems for the thermal-hydraulics analysis module, and also uncertainty for the structure heat conduction analysis module and conjugate heat transfer model was quantified in comparison with the theoretical solutions of unsteady heat conduction problems. Following the V&V study, MUGTHES was validated for a practical fluid-structure thermal interaction problem in T-junction piping system by comparison with the measured results of velocity and temperatures

of fluid and structure [103]. The validation was carried out for a relatively coarse mesh, using LES standard Smagorinsky model and the wall functions.

Takahashi et al. [105] investigated the characteristics of fluid temperature fluctuation in the mixing tee pipe through experiments. They presented the mixing flow patterns, the location of the maximum fluid temperature fluctuation and the characteristics of fluid temperature fluctuation downstream of the tee pipe. The experimental results showed that the characteristics of fluid temperature fluctuation were closely related to the flow pattern in the tee pipe and the flow pattern of the turned jet (or deflecting jet) in the tee pipe could suppress the fluid temperature fluctuation. Hibara et al. [106] investigated the flows downstream of T-junction experimentally, and installed a turbulence promoter in T-junction in order to reduce fluid temperature fluctuations. The experimental results showed that secondary streams in pipe cross-sections became stronger and diffusion of momentum was promoted. Also, the range of flow velocity ratio for transition from deflecting jet to impinging jet became narrow. Shigeta et al. [107] carried out the experiments in the mixing tee with fluid temperature fluctuation through flow visualization, measurement of fluid temperature and heat transfer using a micro heat flux sensor. The velocity ratio K of flows in the branch and main ducts was changed from K=0.25 to K=4.0. The periodic vortical flow was observed through flow visualization for the cases of K=0.6 and 0.8, and this induced both the fluid temperature and the wall heat flux fluctuations.

Kuhn et al. [108] investigated the mixing in T-junctions made of different materials (brass and steel) and having two different pipe wall thicknesses. The temperature difference between the inlets of main and branch pipes was 75°C and the mass flow rate in the main pipe was three times larger than that in the branch pipe. They first performed a set of simulations by using different LES subgrid-scale (SGS) turbulence models including standard Smagorinsky model (SSM) and dynamic Smagorinsky model (DSM), to identify the effect of SGS turbulence models on the simulation results. The near-wall mesh size has the maximum y^+ of 5.0 in the mixing zone. Such mesh can resolve the flow boundary layer and however, is insufficient to resolve the thermal boundary layer for Prandtl number of 7.0. The calculation method of heat transfer between fluid

and solid was not described in the article. The comparison of the DSM numerical results with available experimental data (only the contours of temperature and its RMS on the outer surface measured by infrared thermography) showed a qualitative agreement. Then, they carried out LES simulation of T-junction with different wall thickness using DSM. The wall thickness had a damping effect on the temperature fluctuations across the pipe thickness.

Hu et al. [109] undertook the simulation of flow and temperature at T-junctions based on the RNG LES model using the commercial CFD code, FLUENT. The simulation results for the temperature fluctuations have significant difference from the experimental ones, although the calculated results for the time-averaged temperature agree well with the experimental ones. Lee et al. [110] carried out numerical analyses of the temperature fluctuations using LES simulation based on the RNG SGS turbulence model and compared CFD results with the experimental data. For the thermal stress fatigue analysis, a model was developed to reveal the relative importance of various parameters affecting fatigue-cracking failure. The investigation results showed that the temperature difference between the hot and cold fluids at a tee junction and the heat transfer coefficient enhanced by turbulent mixing were the predominant factors of thermal fatigue failure at a tee junction.

As reviewed in Sub-section 1-3-2 and 1-3-3, a large number of investigations of thermal loading evaluation have been carried out using CFD simulations so far. RANS-based turbulence models were mainly applied in the earlier studies. RANS-based CFD simulations could not predict the fluid temperature fluctuations well. Recently, DES and LES were also widely applied for thermal loading evaluation with availability of high performance computing (HPC) computers and advancement of CFD simulation technology. Some LES-based simulations reproduced the experimental results especially when using dynamic Smagorinsky model (DSM) for the SGS turbulence model. However, specific guidelines, which show which numerical methods (including turbulence models and differencing schemes) can provide high-accuracy predictions of the fluid temperature fluctuations with moderate conservativeness, have not yet been established. Particularly, to date, the predictions of structure temperature fluctuations (or thermal fatigue

loading) were performed either using heat transfer coefficient (including a constant) evaluated from the empirical equation (e.g. Dittus-Boelter equation) [42] [55], or using the wall functions [72] [84] [85]. So far, there have been almost no cases where predictions have been carried out of the structure temperature fluctuations through the direct conjugate heat transfer between fluid and structure with high accuracy.

1-3-4 Flow Pattern Classification for Evaluation of Thermal Loading

Many investigations have been carried out over the years to enhance the understanding of the important parameters affecting the extent of damage induced by thermal fatigue. Both experiments [111] and numerical analysis [83] [110] have confirmed that the flow pattern is one of the most important parameters that determines the degree of damage associated with the mixing of fluids with different temperatures. Igarashi et al. [19] found that flow pattern at a tee junction can be classified using the momentum ratio defined as follows:

$$M_m = D_m D_b \rho_m V_m^2 \tag{1-1}$$

$$M_b = \frac{\pi}{4} D_b^2 \rho_b V_b^2 \tag{1-2}$$

$$M_R = M_m / M_b \tag{1-3}$$

Based on Eqs. (1-1)~(1-3) and the criteria given in **Table 1-2, s**everal authors [19] [83] [109] [111] have classified the flow patterns at tee junctions into three groups of wall jet, deflecting jet and impinging jet, as shown in **Fig. 1-10**. The currently accepted method for classifying the flow patterns is based on the momentum ratio. Other authors (e.g. [112]) have classified them into four groups of wall jet, re-attached jet, turn jet and impinging jet, based on Eqs. (1-1)~(1-3) and the criteria given in **Table 1-3**. Despite this slight difference in the classification, all of these authors have applied the same approach to relate the flow patterns to the momentum ratio between the branch and main pipe flows. In addition, all of these authors have made the flow pattern classifications based on visualizations or experimental observations.

Table 1-2 Criteria 1 for T-Junctions [19]

Wall jet	$1.35 \leq M_R$
Deflecting jet	$0.35 < M_R < 1.35$
Impinging jet	$M_R \leq 0.35$

Table 1-3 Criteria 2 for T-Junctions [112]

Wall jet	$4.0 \leq M_R$
Re-attached Jet	$1.35 < M_R < 4.0$
Turn jet	$0.35 < M_R \leq 1.35$
Impinging jet	$M_R \leq 0.35$

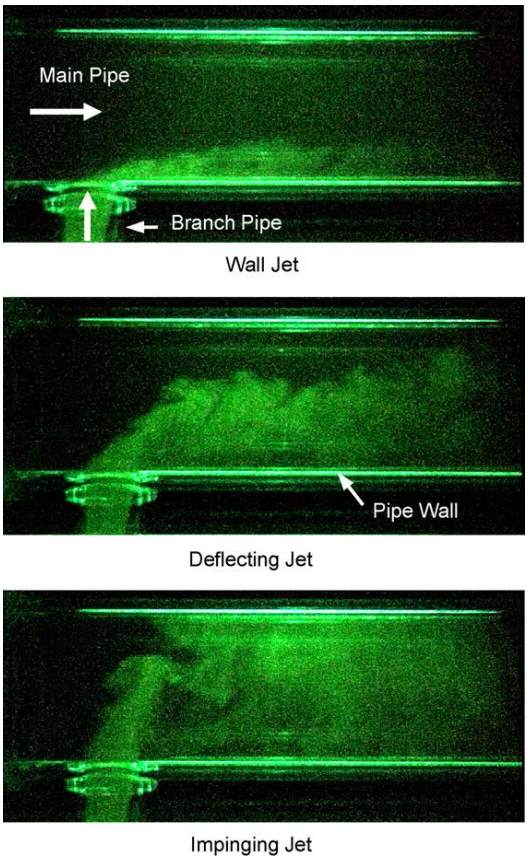

Fig. 1-10 Flow Patterns at Tee Junctions [83]

As shown in **Fig. 1-10**, the mixing of the hot and cold fluids from the main pipe and branch pipe takes place near the downstream main pipe wall on the same side as the branch pipe for the wall jet, and takes place in the central region away from the wall of main pipe for the deflecting jet, and takes place near the wall surface of main pipe opposite the branch pipe for the

impinging jet. Many researchers have shown comprehensively, through experiments and numerical analysis, that the more damaging flow patterns are the wall jet and impinging jet flow patterns, with the impinging jet being the worst, because intensive temperature fluctuations induced by the mixing of the hot and cold fluids are produced near the wall surface of the main pipe in those cases. However, the deflecting jet is less damaging flow pattern, as the intensive temperature fluctuations occur in the central region of main pipe away from the pipe wall. Therefore, it is very important to perform the classification of flow patterns when evaluating the high cycle thermal fatigue induced by the fluid temperature fluctuations.

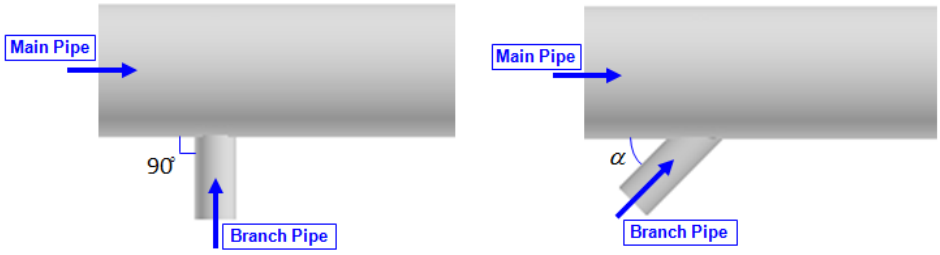

(a) T-junction **(b) Y-junction**

Fig. 1-11 Schematic for T-Junction and Y-Junction

It should be pointed out that the conventional characteristic equations used for determining the flow patterns are only applicable to 90° tee junctions (T-junctions), as shown in **Fig. 1-11 (a)**. A small amount of work carried out by Oka [90] has studied the effect on energy loss of angled tee junctions. However, work has not yet been done regarding the flow pattern classification of tee junctions with angles other than 90° (Y-junctions), as shown in **Fig. 1-11 (b)**.

1-4 JSME Guideline for Evaluation of High Cycle Thermal Fatigue

Following the leakage accident in LWR, the effort was made to develop a guideline of thermal fatigue evaluation in Japan. Fukuda et al. [114] described the effort to establish a JSME guideline for evaluation of high-cycle thermal fatigue. The evaluation flow of thermal striping in a mixing tee and thermal stratification in a branch pipe with a closed end, where the thermal fatigue may occur, was examined. The procedure for evaluation of thermal striping in a mixing tee comprises four steps with three charts to screen the design parameters one-by-one according to the severity

of the thermal load predicted under the design conditions. In order to create the charts, visualization experiments with acrylic pipes and temperature measurement tests with metal pipes were performed [115], [116], [117]. The influences of the configuration of mixing tee, flow velocity ratio, etc. were investigated through the experimental tests. The evaluation procedure for thermal stratification includes two steps with two charts to screen horizontal branch pipe length according to the position of elbow and penetration length. In order to evaluate penetration length, the visualization tests under high temperature and pressure conditions were conducted. At the same time, the influences of buoyancy and pipe diameter, main flow velocity, etc. were also investigated through the experiments. Also, Kasahara et al. [118] proposed a structural response function approach to evaluate thermal striping fatigue phenomena, taking into account the fact that the thermal stress fluctuation amplitude varies with the frequency. In this approach, the structural response characteristics depend upon Biot number and constraint conditions of structure. These efforts as well as other relevant researches provide a foundation for establishing a guideline of thermal fatigue evaluation.

In 2003, the Japan Society of Mechanical Engineers (JSME) published "Guideline for Evaluation of High Cycle Thermal Fatigue of a Pipe (JSME S017)" [119] based on the experimental and analytical results, to evaluate HCTF at 90º tee junctions (T-junctions) in nuclear power plants. JSME S017 provides the procedures and methods for evaluating the integrity of structures with the potential for HCTF induced by thermal striping and thermal stratification. Shown in **Fig. 1-12** are the evaluation procedures for HCTF at T-junctions, which comprise the following 4 steps.

Step 1: This step is an initial screening, which evaluates the structural integrity of the piping based on the assumption that the difference between the fluid temperatures at the inlets of main pipe and branch pipe will be equal to the temperature fluctuation range seen by the structure. If the fluid temperature difference (ΔT_{in}) is below the temperature difference corresponding to the structural fatigue limit (or critical temperature difference, ΔT_{cr}), there will

be no risk of thermal fatigue, and thus, the evaluation is complete. Otherwise, the evaluation will proceed to the following step.

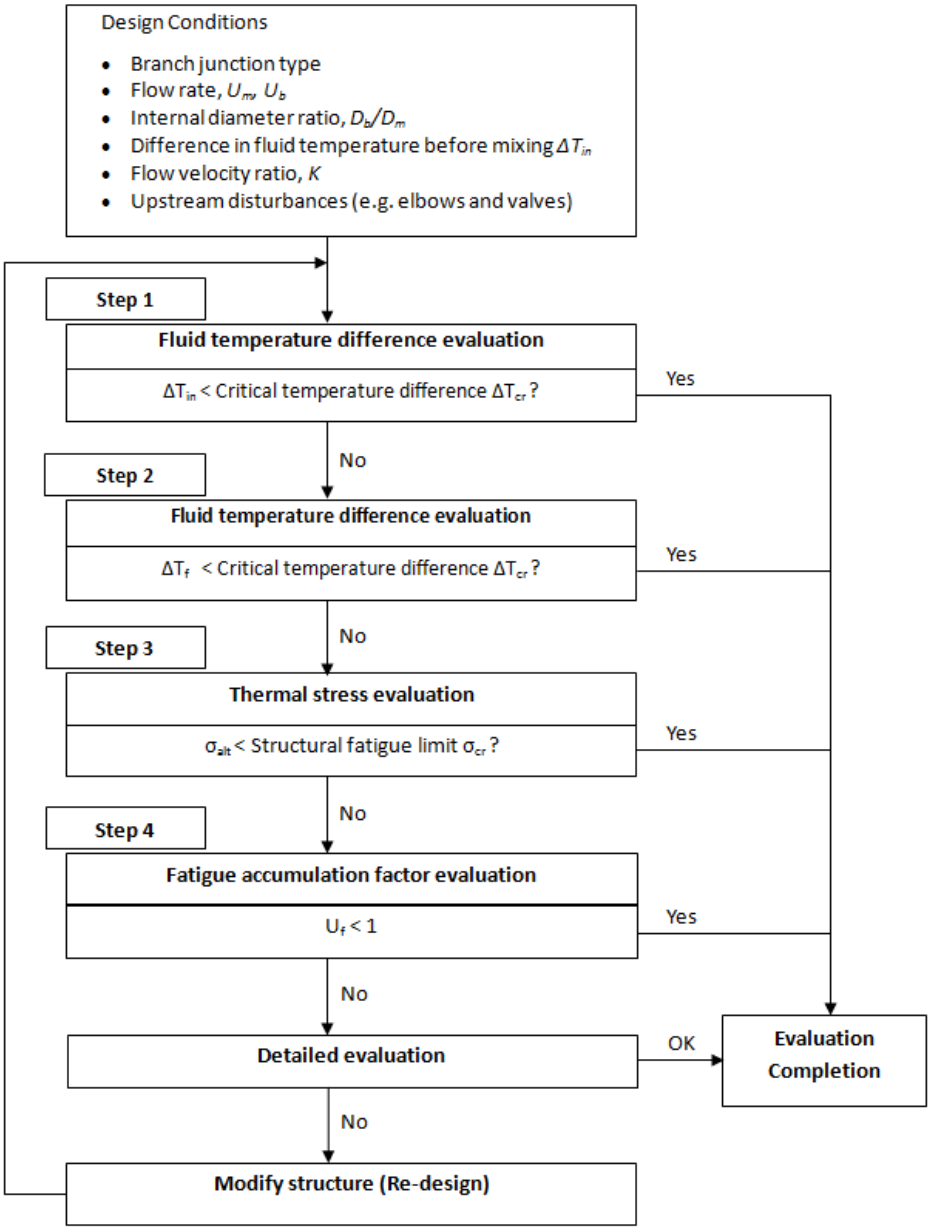

Fig. 1-12 Evaluation Procedures for Thermal Fatigue at T-junction in JSME S017

Step 2: In this step, attenuation of the fluid temperature fluctuations induced by turbulent diffusion in the mixing areas is considered. The attenuation factor is evaluated based on the flow pattern. If the fluid temperature fluctuation range (ΔT_f) evaluated with the consideration of attenuation effect is below the critical temperature difference (ΔT_{cr}), there will be no risk of

thermal fatigue, and thus, the evaluation is complete. Otherwise, the evaluation will proceed to the following step.

Step 3: Applying the attenuated fluid temperature fluctuation range (ΔT_f) and the heat transfer coefficient between the fluid and structural surface, the structure temperature fluctuation range (ΔT_s) and the amplitude of the thermal stress (σ_{alt}) in the structure generated by the fluid temperature fluctuations are sequentially evaluated. The heat transfer coefficient is evaluated also based on the flow pattern. If the fluctuating range of thermal stress is below the material fatigue endurance limit (σ_{cr}), there will be no risk of thermal fatigue, and thus, evaluation is complete. Otherwise, the evaluation will further proceed to the following step.

Step 4: A cumulative fatigue factor U_f is calculated from the fatigue evaluation method which considers the attenuation effects of the temperature fluctuations of both fluid and structure. If the calculated cumulative fatigue factor U_f is smaller than 1.0, there will be no risk of thermal fatigue, and thus, the entire evaluation is complete. Otherwise, it becomes necessary to redesign the structure for avoiding thermal fatigue and repeat the above evaluation loop.

Obviously, it can be found that one of the important procedures of thermal fatigue evaluation is to classify the flow pattern at a T-junction for evaluating thermal load in Step 2~4 in JSME S017, as the attenuation effect of fluid temperature fluctuations and the heat transfer coefficient between fluid and structure surface, which are needed for evaluation of thermal load, are evaluated based on flow pattern. It should be pointed out that classification of the flow pattern intended for thermal fatigue evaluation here is to identify whether the mixing zone of the hot and cold fluids from the main and branch pipes is near the wall surface of main pipe or far from the wall surface. When the mixing takes place near the pipe wall surface, the fluid temperature fluctuations caused by mixing are easily transferred to the structure, and hence, the risk of thermal fatigue will be high. That is to say, the extent of damage caused by thermal fatigue is different for different flow patterns, even though the temperature difference between the fluids before mixing is the same.

However, when applying JSME S017 to evaluate the thermal fatigue at tee junctions, the evaluation accuracy is not high and especially the evaluation margin varies greatly from one case to another case [120]. In addition, it should be pointed out that for JSME S017, the fatigue evaluation method in Step 4 was developed based on the experimental data and hence, its application is limited to the range where the experimental data were obtained. Also, the dependence of thermal stress attenuation on the fluctuation frequency of fluid temperature was not considered in Step 4. In view of this, the thermal fatigue research project had been carried out as a part of the Japan Aging Management Program on System Safety (JAMPSS) sponsored by Nuclear Regulation Authority (NRA) from 2009 through 2013, in order to rationalize the existing JSME S017 [121] [122]. The present author also joined the thermal fatigue research project.

1-5 Objectives of the Present Study

As described above, when applying JSME S017 for evaluation of thermal fatigue, one of the important procedures of thermal fatigue evaluation is to classify flow patterns at tee junctions because the degree of thermal fatigue damage is closely related to flow pattern at a tee junction. When evaluating the thermal load, the attenuation effect of fluid temperature fluctuations and the heat transfer coefficient between fluid and structure surface need to be determined based on flow pattern at a T-junction. The conventional characteristic equations for classifying flow patterns are only applicable to 90º tee junctions (T-junctions) [19]. It seems that almost only T-junctions are used in nuclear power plants. However, angled tee junctions other than 90º (Y-junctions), are also used for mixing hot and cold fluids in process plants, such as petrochemical plants, refineries and LNG plants, to mitigate erosion of the main pipe due to impingement of the branch pipe flow against the main pipe and reduce the pressure drop produced by the mixing of fluids. As a result, it is necessary to evaluate the structural integrity of Y-junctions in the operating plants and newly designed plants by extending the conventional guideline JSME S017. Therefore, it is essential to establish a generalized classification method of flow patterns applicable to both T-junctions and Y-junctions.

In addition, the accuracy of evaluation results based on JSME S017 is not high and especially the evaluation margin varies greatly depending on the case [120], as JSME S017 was developed based on limited experimental data and simplified one-dimensional (1D) FEA. Moreover, for JSME S017, the fatigue evaluation method in Step 4 was established based on the experimental data and thus, its application is limited to the range where the experimental data were obtained. As well, dependence of thermal stress attenuation on the frequency of fluid temperature fluctuations was not considered in Step 4. Hence, it is desirable to establish a more accurate method of HCTF evaluation with moderate conservativeness and extended applicable area. CFD/FEA coupling analysis is expected to be a useful and effective tool for developing such an evaluation method.

As reviewed above, many investigations on CFD-based evaluation methods of thermal loadings have been carried out for evaluating thermal fatigue at T-junctions. However, specific guidelines, which show which numerical methods (including turbulence models and differencing schemes) are capable of providing high-accuracy prediction of thermal loadings with moderate conservativeness, have not yet been established. The goal of this study is to establish an integrated, high-accuracy evaluation method for high-cycle thermal fatigue based on CFD/FEA coupling analysis. Such an evaluation method is expected to be capable of more accurately predicting the fluctuation amplitudes and cycle numbers (or frequencies) of thermal stress caused by the structure temperature fluctuations using FEA, in order to perform fatigue damage prediction. The coupled CFD/FEA analysis will be used as a tool of numerical experiment for upgrading JSME S017, instead of the conventional experiments. As a result, the integrated evaluation method of thermal fatigue will be able to enhance the accuracy of thermal fatigue evaluation and extend the applicable area and take into account the dependence of thermal stress attenuation on the frequency of fluid temperature fluctuations.

Therefore, one objective of the present study is to propose a generalized classification method of flow patterns applicable to both T-junctions and Y-junctions, in order to apply JSME S017 to evaluate thermal fatigue for both of them. At the same time, the validity of generalized

classification method of flow patterns is verified by CFD simulations of fluid flow and temperature fields for T-junctions and Y-junctions.

Another more important objective of the present study is to establish high-accuracy CFD prediction methods of thermal loading for developing a more accurate evaluation method of thermal fatigue based on CFD/FEA coupling analysis. The root cause of thermal fatigue is the fluid temperature fluctuations induced by incomplete mixing of hot and cold fluids at a T-junction. Hence, accurate prediction of the fluid temperature fluctuations is first needed for high-accuracy prediction of thermal loading. There are various factors affecting prediction accuracy of the fluid temperature fluctuations. At the same time, it is also necessary to find a method capable of accurately calculating heat transfer between fluid and structure for high-accuracy prediction of thermal loading. Therefore, in order to establish high-accuracy CFD prediction methods of thermal loading with high efficiency, the CFD benchmark investigations are carried out in the following two steps:

- First, the high-accuracy CFD prediction methods of fluid temperature fluctuations at a T-junction are established by CFD benchmark simulations for fluid region only.
- Then, the high-accuracy CFD prediction methods of structure temperature fluctuations (or thermal loading) at a T-junction are established through CFD benchmark simulation of fluid flow and thermal interaction between fluid and structure, using a model including both fluid and structure regions.

It should be pointed out that CFD is just used as a tool of thermal loading prediction for thermal fatigue evaluation in the present study. It is not the aim of the present study to develop a new CFD numerical scheme or turbulence model.

1-6 Outline of the Present Thesis

In this thesis, the main contents in the subsequent chapters are as follows.

In **Chapter 2**, the governing equations of fluid flow, relevant turbulence models and numerical difference schemes used in CFD simulations in the later chapters, and especially their main features are concisely described.

In **Chapter 3,** the generalized classification method of flow pattern at all angles of tee junctions is first proposed for thermal loading evaluation, by investigating the mechanism of the interaction of momentum between main and branch pipes. Then, CFD simulations of flow and temperature fields are carried out for different angles (including 30°, 45°, 60° and 90°) of tee junctions, in order to identify validity of the proposed generalized classification method of flow pattern.

In **Chapter 4**, LES-based CFD benchmark simulations of fluid temperature fluctuations at a T-junction are performed to investigate comprehensively the effects of various turbulence models and numerical schemes on the accuracy of simulation results. The simulation results are compared with the experimental results for establishing high-accuracy CFD prediction methods of fluid temperature fluctuations.

In **Chapter 5**, based on the research results obtained in **Chapter 4**, the numerical methods of predicting temperature fluctuations for both fluid and structure at a T-junction are proposed, and applied to evaluate thermal fatigue loading. Then, the simulation results are compared with the experimental results, in order to prove that the proposed numerical methods are capable of providing high-accuracy prediction of thermal fatigue loading.

Chapter 6 presents some proposals of applications of the research results, which have been obtained in **Chapters 3~5**, to thermal fatigue evaluation.

Finally, the conclusions and some suggestions for future work are presented in **Chapter 7**.

Chapter 2 Governing Equations for Fluid Flow and Turbulence Models and Numerical Difference Schemes

The present study aims at establishing the CFD-based evaluation methods of thermal fatigue loadings, which are fluid and structure temperature fluctuations caused by incomplete mixing of hot and cold fluids at tee junctions. At first, the governing equations of fluid flow and relevant turbulence models and numerical difference schemes used in CFD simulations in the subsequent chapters are concisely introduced in this chapter.

2-1 Governing Equations of Fluid Flow

The governing equations of fluid flow can be derived, based on the laws of the mass conservation, the momentum conservation (or Newton's second law of motion) and the energy conservation (or first law of thermodynamics) [100]. The mass conservation equation and momentum conservation equations are also called the continuity equation and the Navier-Stokes (N-S) equations, respectively. The continuity equation, N-S equations and energy equation can be expressed as follows:

$$\frac{\partial \rho}{\partial t}+\frac{\partial(\rho u_i)}{\partial x_i}=0 \tag{2-1}$$

$$\frac{\partial(\rho u_i)}{\partial t}+\frac{\partial(\rho u_i u_j)}{\partial x_j}=-\frac{\partial p}{\partial x_i}+\frac{\partial}{\partial x_j}\left[\mu\left(\frac{\partial u_i}{\partial x_j}+\frac{\partial u_j}{\partial x_i}\right)\right] \tag{2-2}$$

$$\frac{\partial(\rho h)}{\partial t}+\frac{\partial(\rho u_j h)}{\partial x_j}=\frac{\partial}{\partial x_j}\left(\lambda\frac{\partial T}{\partial x_j}\right) \tag{2-3}$$

where ρ stands for the fluid density, u for the flow velocity, μ for the fluid viscosity, p for the pressure, h for the enthalpy of fluid, λ for the thermal conductivity of fluid and T for the fluid temperature.

The CFD simulations aim to numerically solve the above governing equations of fluid flow. According to Bardina et al. [124], there are six categories for the approaches of predicting

turbulent flows. Among them, the major numerical approaches for CFD simulations include the following three categories.

- Direction Numerical Simulation (DNS):

  The governing equations are directly solved for all the scales of flow motions without use of turbulence model.

- Large Eddy Simulation (LES):

  The space-averaged governing equations are solved in combination with a sub-grid scale (SGS) turbulence model (e.g., standard Smagorinsky model (SSM) and dynamic Smagorinsky model (DSM)). In LES, the larger eddies above the grid scale (GS) are directly solved, but the smaller SGS eddies need to be modeled using SGS turbulence model.

- Reynolds-Averaged Navier-Stokes (RANS) Equations Based Simulation:

  The RANS equations are solved in combination with a RANS-based turbulence model (e.g., various $k-\varepsilon$ models and $k-\varpi$ model).

Table 2-1 Main Features of Three Major CFD Approaches

	DNS	LES	RANS
Governing Equations	N-S equations	Space-averaged N-S equations	RANS equations
Turbulence Model	Not needing turbulence model	SGS turbulence models: SSM, DSM, etc.	$k-\varepsilon$ models, $k-\varpi$ model, etc.
Mesh	Very fine	Moderately fine	Coarse
Numerical Accuracy	Very high (unsteady solution)	High (unsteady solution)	Relatively low (time-averaged solution)
Cost	Very high	Moderate	Low
Computing Time	Very long	Relatively long	Short
Application Areas	Fundamental studies to reveal the detailed turbulence structure of flow filed	Unsteady simulations: thermal loading evaluation, flow-induced vibration (FIV), flow-induced acoustics (FIA), etc.	Steady simulations in various industries: time-averaged flow field (or flow pattern), temperature field, concentration field, etc.

The main features of above three major CFD approaches are briefly described in **Table 2-1**. At the present time, it is still impractical to use DNS for industrial applications due to its high cost and long computation time. The flow simulation approaches applicable for industrial applications are still RANS and LES, one of which needs to be chosen for the specific purpose. The governing equations and relevant turbulence models for RANS and LES are briefly described in the next sections, for the applications in the present study.

2-2 Reynolds-Averaged Governing Equations and Turbulence Models

2-2-1 Reynolds-Averaged Governing Equations

The Reynolds-averaged (or ensemble-averaged, which is a sort of time-averaged) continuity and Navier-Stokes and energy equations can be written as:

$$\frac{\partial \rho}{\partial t}+\frac{\partial(\rho \overline{u_i})}{\partial x_i}=0 \tag{2-4}$$

$$\frac{\partial(\rho \overline{u_i})}{\partial t}+\frac{\partial}{\partial x_j}(\rho \overline{u_i}\,\overline{u_j}+\rho \overline{u_i' u_j'})= \frac{\partial \overline{p}}{\partial x_i}+\frac{\partial}{\partial x_j}\left[\mu\left(\frac{\partial \overline{u_i}}{\partial x_j}+\frac{\partial \overline{u_j}}{\partial x_i}\right)\right] \tag{2-5}$$

$$\frac{\partial(\rho \overline{h})}{\partial t}+\frac{\partial}{\partial x_j}(\rho \overline{u_j}\,\overline{h}+\rho \overline{u_j' h'})=\frac{\partial}{\partial x_j}\left(\lambda \frac{\partial \overline{T}}{\partial x_j}\right) \tag{2-6}$$

Reynolds-averaging any linear term in the conservation equations produces the identical term for the averaged quantity. Hence, the Reynolds-averaged continuity equation has the same form as the original equation. However, as a result of Reynolds-averaging Navier-Stokes equations, a new term $\rho \overline{u_i' u_j'}$, which is usually called Reynolds stresses, is produced in the RANS equations (2-5). Similarly, Reynolds-averaging energy equation introduces a new term $\rho \overline{u_j' h'}$, known as the turbulent energy flux. These new terms cannot be represented uniquely in terms of the averaged quantities and thus need to be modeled to close the averaged governing equations for numerical simulations. Traditionally, the Reynolds stresses $\rho \overline{u_i' u_j'}$ are expressed below, in a form similar to the viscous stresses, based on the Boussinesq hypothesis [126]:

$$-\rho\overline{u_i'u_j'} = \mu_T\left(\frac{\partial\overline{u_i}}{\partial x_j}+\frac{\partial\overline{u_j}}{\partial x_i}\right)-\frac{2}{3}\rho k\delta_{ij} \tag{2-7}$$

where μ_T stands for turbulent eddy viscosity, k for turbulent kinetic energy ($k=\overline{u_i'u_i'}/2$), δ_{ij} for Kronecker's delta and ε for dissipation rate of turbulent kinetic energy.

In addition, the turbulent energy flux $\rho\overline{u_j'h'}$ in Eq.(2-3) is also traditionally expressed in a form similar to the molecular thermal diffusion, as follows:

$$-\rho\overline{u_i'h'} = \lambda_T\frac{\partial\overline{T}}{\partial x_j} \tag{2-8}$$

where λ_T stands for turbulent thermal conductivity. Introducing the turbulent Prandtl number ($\mathrm{Pr}_T = c_p\mu_T/\lambda_T$), Equation (2-8) can be rewritten as below

$$-\rho\overline{u_i'h'} = \frac{c_p\mu_T}{Pr_T}\frac{\partial\overline{T}}{\partial x_j} \tag{2-9}$$

Substituting Eq.(2-7) into Eq.(2-2), Reynolds-averaged Navier-Stokes (RANS) equations can be rewritten as:

$$\frac{\partial(\rho\overline{u_i})}{\partial t}+\frac{\partial(\rho\overline{u_i}\overline{u_j})}{\partial x_j} = \frac{\partial\overline{p}}{\partial x_i}+\frac{\partial}{\partial x_j}\left[(\mu+\mu_T)\left(\frac{\partial\overline{u_i}}{\partial x_j}+\frac{\partial\overline{u_j}}{\partial x_i}\right)\right] \tag{2-10}$$

Meanwhile, by substituting Eq.(2-9) into Eq.(2-3), Reynolds-averaged energy equation can be rewritten as follows:

$$\frac{\partial(\rho\overline{h})}{\partial t}+\frac{\partial(\rho\overline{u_j}\overline{h})}{\partial x_j} = \frac{\partial}{\partial x_j}\left((\lambda+\frac{c_p\mu_T}{Pr_T})\frac{\partial\overline{T}}{\partial x_j}\right) \tag{2-11}$$

The turbulent eddy viscosity μ_T needs to be determined to solve the equations (2-10) and (2-11). How to evaluate the turbulent eddy viscosity is the task of turbulence modeling. Only the standard $k-\varepsilon$ model and the realizable $k-\varepsilon$ model of interest are briefly described in the next two sections, although a number of RANS-based turbulence modeling methods have been developed [125].

2-2-2 Standard k-ε Turbulence Model

In the standard $k-\varepsilon$ model, the turbulent eddy viscosity μ_T is evaluated using the turbulent energy k and its dissipation rate ε [127] [128] with the assumption that the turbulence is isotropic. The turbulent energy and its dissipation rate transport equations can be derived from Navier-Stokes equations [123]. Their most commonly used forms are as follows:

$$\frac{\partial \rho k}{\partial t}+\frac{\partial}{\partial x_j}\left(\rho k\overline{u_j}\right)=\frac{\partial}{\partial x_j}\left[\left(\mu+\frac{\mu_T}{\sigma_k}\right)\frac{\partial k}{\partial x_j}\right]+G_k+G_b-\rho\varepsilon \tag{2-12}$$

$$\begin{aligned}\frac{\partial \rho \varepsilon}{\partial t}+\frac{\partial}{\partial x_j}\left(\rho \varepsilon\overline{u_j}\right)&=\frac{\partial}{\partial x_j}\left[\left(\mu+\frac{\mu_T}{\sigma_\varepsilon}\right)\frac{\partial \varepsilon}{\partial x_j}\right]\\&+\frac{\varepsilon}{k}\left[C_{\varepsilon 1}G_k+C_{\varepsilon 3}max(0,G_b)-C_{\varepsilon 2}\rho\varepsilon\right]\end{aligned} \tag{2-13}$$

where the turbulence-induced source term G_k and buoyancy-induced source term G_b are defined respectively, as follows:

$$G_k=\left[\mu_T\left(\frac{\partial\overline{u_i}}{\partial x_j}+\frac{\partial\overline{u_j}}{\partial x_i}\right)-\frac{2}{3}\rho k\delta_{ij}\right]\frac{\partial\overline{u_i}}{\partial x_j} \tag{2-14}$$

$$G_b=\frac{\mu_T}{\mathrm{Pr}_T}\frac{g_i}{T}\frac{\partial T}{\partial x_i}=-\frac{\mu_T}{\mathrm{Pr}_T}\frac{g_i}{\rho}\frac{\partial \rho}{\partial x_i} \tag{2-15}$$

After the turbulent energy k and its dissipation rate ε are solved from Eqs. (2-12) and (2-13), the turbulent eddy viscosity μ_T can be evaluated as follows:

$$\mu_T=\rho C_\mu\frac{k^2}{\varepsilon} \tag{2-16}$$

The model parameters used in the above equations are listed in **Table 2-1**.

Table 2-2 Parameters in the Standard k−ε Model

C_μ	σ_k	σ_ε	Pr_T	$C_{\varepsilon 1}$	$C_{\varepsilon 2}$	$C_{\varepsilon 3}$
0.09	1.0	1.3	0.9	1.44	1.92	1.3

The standard $k-\varepsilon$ model is widely used for the steady CFD simulations especially in various industrial applications, as it is relatively simple to implement and the numerical simulations converge relatively easily. However, it over-predicts the production of turbulence, which leads to the over-evaluation of turbulent eddy viscosity for most cases and moreover, it provides poor predictions for the complex flows, such as swirling and rotating flows, flows with strong separation, and axis symmetric jets. Therefore, many efforts were made for improving the standard $k-\varepsilon$ model.

2-2-3 Realizable k-ε Turbulence Model

The realizable $k-\varepsilon$ model [129] is one of the modified two-equation $k-\varepsilon$ models and differs from the standard $k-\varepsilon$ model in two important aspects:

- A new transport equation for the dissipation rate (ε) was derived from an exact equation for the transport of the mean-square vorticity fluctuation.
- The realizable $k-\varepsilon$ model modified the evaluation of turbulent eddy viscosity using a variable C_μ instead of using a constant.

The realizable $k-\varepsilon$ model uses the same turbulent kinetic energy equation as the standard $k-\varepsilon$ model and only the equation for turbulent kinetic energy dissipation rate ε was improved. The turbulent energy and its dissipation rate transport equations are expressed as follows:

$$\frac{\partial \rho k}{\partial t}+\frac{\partial}{\partial x_j}\left(\rho k\overline{u_j}\right)=\frac{\partial}{\partial x_j}\left[\left(\mu+\frac{\mu_T}{\sigma_k}\right)\frac{\partial k}{\partial x_j}\right]+G_k+G_b-\rho\varepsilon \tag{2-17}$$

$$\begin{aligned}\frac{\partial \rho \varepsilon}{\partial t}+\frac{\partial}{\partial x_j}\left(\rho \varepsilon\overline{u_j}\right)&=\frac{\partial}{\partial x_j}\left[\left(\mu+\frac{\mu_T}{\sigma_\varepsilon}\right)\frac{\partial \varepsilon}{\partial x_j}\right]\\&\quad+\rho C_1 S\varepsilon-\rho C_2\frac{\varepsilon^2}{k+\sqrt{\upsilon\varepsilon}}+C_{1\varepsilon}\frac{\varepsilon}{k}C_{3\varepsilon}G_b\end{aligned} \tag{2-18}$$

The turbulent eddy viscosity μ_T is evaluated from Eq.(2-19) below, after the turbulent energy k and its dissipation rate ε are solved from Eqs. (2-17) and (2-18). It should be pointed out that the parameter C_μ is a variable, differing from the standard $k-\varepsilon$ model.

$$\mu_T = \rho C_\mu \frac{k^2}{\varepsilon} \tag{2-19}$$

The parameters used in the realizable $k-\varepsilon$ model are calculated or given as follows:

$$C_1 = \max\left[0.43, \frac{\eta}{\eta+5}\right], \quad \eta = S\frac{k}{\varepsilon}, \quad S = \sqrt{2S_{ij}S_{ij}}$$

$$C_\mu = \frac{1}{A_0 + A_s \dfrac{kU^*}{\varepsilon}}$$

$$U^* \equiv \sqrt{S_{ij}S_{ij} + \tilde{\Omega}_{ij}\tilde{\Omega}_{ij}}$$

$$\tilde{\Omega}_{ij} = \Omega_{ij} - 2\varepsilon_{ijk}\omega_k$$

$$\Omega_{ij} = \overline{\Omega}_{ij} - \varepsilon_{ijk}\omega_k$$

$$A_0 = 4.04, \quad A_s = \sqrt{6}\cos\phi$$

$$\phi = \frac{1}{3}\cos^{-1}(\sqrt{6}W), \quad W = \frac{S_{ij}S_{jk}S_{ki}}{\tilde{S}^3}, \quad \tilde{S} = \sqrt{S_{ij}S_{ij}}, \quad S_{ij} = \frac{1}{2}\left(\frac{\partial \overline{u_i}}{\partial x_j} + \frac{\partial \overline{u_j}}{\partial x_i}\right)$$

$$C_{1\varepsilon} = 1.44, \quad C_2 = 1.9, \quad \sigma_k = 1.0, \quad \sigma_\varepsilon = 1.2$$

The term "realizable" means that the model was improved to satisfy certain mathematical constraints on the Reynolds stresses and be consistent with the physics of turbulent flows. As a result, the realizable $k-\varepsilon$ model is capable of more reasonably predicting the turbulent eddy viscosity and improves the prediction performance for flows, such as flows with strong adverse pressure gradients or separation, rotating and swirling and recirculation flows, planar and round jets, and flows with strong streamline curvature [130] [131].

2-3 Large Eddy Simulation

2-3-1 Space-Averaged Governing Equations

The spatially filtered (space-averaged) Navier-Stokes equations are solved for the large eddy simulation (LES). The filtering operation decomposes the flow field into larger eddies above the

grid scale (GS) and smaller sub-grid scale (SGS) eddies. The larger eddies are directly solved, but the smaller ones need to be modeled using an SGS turbulence model. Hence, LES is suitable for the simulation of three dimensional (3D), time-dependent flow field. For simplicity, the one-dimensional filtered velocity can be defined below.

$$\bar{u}(x,t)=\int G(x,x')u(x',t)dx' \tag{2-20}$$

where the filter kernel $G(x,x')$ is a localized function. Filter kernels which have been proposed for application in LES include a Gaussian filter, a cutoff filter (which cuts all Fourier coefficients with wave-numbers above a cutoff) and a top-hat filter (a simple local volume-averaging). Every filter has a length scale Δ (or filter width). As a result, large eddies with size larger than Δ can directly be resolved, while those small eddies with size smaller than Δ need to be modeled. When the Navier-Stokes equations for incompressible flow are filtered, the obtained space-averaged equations are very similar to the RANS equations in the form:

$$\frac{\partial \rho}{\partial t}+\frac{\partial(\rho\overline{u_i})}{\partial x_i}=0 \tag{2-21}$$

$$\frac{\partial(\rho\overline{u_i})}{\partial t}+\frac{\partial(\rho\overline{u_i}\,\overline{u_j})}{\partial x_j}=-\frac{\partial \overline{p}}{\partial x_i}+\frac{\partial}{\partial x_j}\left[\mu\left(\frac{\partial\overline{u_i}}{\partial x_j}+\frac{\partial\overline{u_j}}{\partial x_i}\right)\right]-\frac{\partial}{\partial x_j}(\rho\overline{u_iu_j}-\rho\overline{u_i}\,\overline{u_j}) \tag{2-22}$$

The third term on the right-hand side of Eq.(2-22) is called SGS Reynolds stresses and can be written as:

$$\overline{u_iu_j}-\overline{u_i}\,\overline{u_j}=L_{ij}+C_{ij}+R_{ij} \tag{2-23}$$

$$L_{ij}=\overline{\overline{u_i}\,\overline{u_j}}-\overline{u_i}\,\overline{u_j} \tag{2-24}$$

$$C_{ij}=\overline{\overline{u_i}u_j'}+\overline{u_i'\overline{u_j}} \tag{2-25}$$

$$R_{ij}=\overline{u_i'u_j'} \tag{2-26}$$

where, L_{ij}, C_{ij}, R_{ij} are the apparent stresses acting on the large eddies and produced by filtering operation. They are called Leonard term, Cross term and Reynolds term respectively.

So far, many SGS turbulence models have been proposed for LES. In the standard Smagorinsky model and dynamic Smagorinsky model, the Leonard term and Cross term are neglected and only the Reynolds term is modeled. Hence, the SGS Reynolds stresses can be rewritten as follows:

$$\tau_{ij} = \rho R_{ij} = \rho \overline{u_i' u_j'} \tag{2-27}$$

The SGS stress τ_{ij} is modeled below, in a form similar to the viscous stresses, based on the Boussinesq hypothesis [126]:

$$\tau_{ij} - \delta_{ij}\tau_{kk}/3 = -2\mu_T \overline{S}_{ij} \tag{2-28}$$

where μ_T is the SGS turbulent eddy viscosity. As a result, the space-averaged Navier-Stokes equations (2-22) can be rewritten as:

$$\frac{\partial(\rho\overline{u_i})}{\partial t} + \frac{\partial(\rho\overline{u_i}\overline{u_j})}{\partial x_j} = -\frac{\partial \overline{p}}{\partial x_i} + \frac{\partial}{\partial x_j}\left[(\mu + \mu_T)\left(\frac{\partial \overline{u_i}}{\partial x_j} + \frac{\partial \overline{u_j}}{\partial x_i}\right)\right] \tag{2-29}$$

In addition, the space-averaged energy equation has the same form as the Reynolds-averaged energy equation (2-11) as follows:

$$\frac{\partial(\rho\overline{h})}{\partial t} + \frac{\partial(\rho\overline{u_j}\overline{h})}{\partial x_j} = \frac{\partial}{\partial x_j}\left((\lambda + \frac{c_p\mu_T}{Pr_T})\frac{\partial \overline{T}}{\partial x_j}\right) \tag{2-30}$$

For the LES, the turbulence modelling task is to evaluate the SGS turbulent eddy viscosity μ_T using the resolved velocity field $\overline{u_i}$. The standard Smagorinsky model and dynamic Smagorinsky model used in the present research are briefly described in the next two subsections.

2-3-2 Standard Smagorinsky Model

In the standard Smagorinsky model (SSM) [132], the SGS turbulent eddy viscosity μ_T is modeled as follows:

$$\mu_T = \rho(C_s f_\mu \overline{\Delta})^2 \sqrt{2\overline{S}_{ij}\overline{S}_{ij}} \tag{2-31}$$

$$f_\mu = 1 - \exp\left(-y^+ / 25\right) \tag{2-32}$$

$$\overline{\Delta} = V^{1/3} \tag{2-33}$$

$$\overline{S}_{ij} = (\partial \overline{u}_i / \partial x_j + \partial \overline{u}_j / \partial x_i)/2 \tag{2-34}$$

where μ_T is the SGS turbulent eddy viscosity, C_s the Smagorinsky constant, f_μ the damping function for weakening the near-wall numerical turbulence, $\overline{\Delta}$ the spatial filter size, V the volume of grid cell and $\overline{S}_{ij}$ the strain-rate tensor of fluid.

The Smagorinsky constant C_s varies from 0.16 to 0.19 based on the experimental results. The maximum of C_s of 0.23 can be derived for the homogenous isotropic turbulent flow. However, $C_s = 0.1$ is frequently used, as better results can be obtained for the channel flow when using this value. In fact, it is desirable to choose the optimal value of C_s for a specific flow field. In the SSM model, besides C_s being treated as a constant, the damping function f_μ is evaluated only as a function of normalized distance y^+, without considering the effect of the local flow field. However, the SSM model has a relatively good numerical stability.

2-3-3 Dynamic Smagorinsky Model

The dynamic Smagorinsky model (DSM) has been proposed to overcome some shortcomings of SSM. In the DSM model, the model parameter C_s is calculated as a function of local flow field and moreover, no damping function f_μ is used. The SGS turbulent viscosity μ_T in Eq.(2-28) is modeled as follows:

$$\mu_T = \rho(\overline{C}\overline{\Delta}^2)\sqrt{2\overline{S}_{ij}\overline{S}_{ij}} \tag{2-35}$$

where $\overline{C}$ is equivalent to the square of Smagorinsky constant C_s in the SSM model. However, $\overline{C}$ is not treated as a constant in the DSM model. It varies in space and time and is calculated as a function of local flow field with the introduction of a test filer ($\overline{\overline{\Delta}}$). For the dynamic SGS

turbulence model proposed by Germano et al. [133], $\overline{C}$ is evaluated as follows by minimizing the mean square error [134] of Germano's identity L_{ij}.

$$\overline{C}\overline{\Delta}^2 = -L_{ij}^* M_{ij} / (2M_{ij}M_{ij}) \tag{2-36}$$

$$L_{ij}^* = L_{ij} - \delta_{ij} L_{kk} / 3 \tag{2-37}$$

$$L_{ij} = \overrightarrow{\overline{u}_i \overline{u}_j} - \overrightarrow{\overline{u}_i}\,\overrightarrow{\overline{u}_j} \tag{2-38}$$

$$M_{ij} = \alpha^2 |\overrightarrow{\overline{S_{ij}}}|\overrightarrow{\overline{S_{ij}}} - \overrightarrow{|\overline{S_{ij}}|\overline{S_{ij}}} \tag{2-39}$$

$$\alpha = \vec{\overline{\Delta}} / \overline{\Delta} \tag{2-40}$$

Here, the parameter α is usually taken as 2.0. The arrow ($\rightarrow$) over a variable represents the test filtering operation. The test filtering operation can be performed as follows:

$$\vec{\overline{u}}_i = \overline{u}_i + \tilde{\Delta}^2 \overline{u}_{i,kk} / 24 \tag{2-41}$$

$$\tilde{\Delta}^2 = (\alpha^2 - 1)\overline{\Delta}^2 \tag{2-42}$$

where $\tilde{\Delta}$ is the length of Gaussian filter and is evaluated from Eq.(2-42). For the DSM model, there is a possibility that the model parameter $\overline{C}$ becomes negative, or has a large value when the denominator in the right-hand side of Eq.(2-36) has a very small value. Therefore, the averaging of $\overline{C}$ is usually done along a homogeneous direction for maintaining numerical stability. If it is very difficult to do so, a local averaging can be used instead. In addition, a limit, for example [0, 0.053], is usually imposed on the calculated $\overline{C}$. Here, the value 0.053 corresponds to the maximum value 0.23 of the Smagorinsky constant C_s in SSM.

2-4 Numerical Difference Schemes

In the CFD simulations, the resolvable maximal wave number is $k_{\max} = \pi / \Delta x$ for a mesh with the size of Δx. All the high wave number components of $k > k_{\max}$ will be spuriously resolved as the component of $k_{\max}$. This is so called aliasing error [135]. Aliasing error will lead to the

concentration of energy of the component of wave number $k = k_{\max}$, and as a result, may cause the numerical stability. Therefore, not only is the high accuracy very important, but also the numerical stability is necessary for a high-accuracy numerical method in the CFD simulations. Below, several numerical difference schemes used in the present study are briefly introduced with the focus placed on both their numerical accuracy and stability.

2-4-1 Hybrid Scheme

The features of the 2nd-order accurate central difference scheme (2CD) and the 1st-order accurate upwind difference scheme (1UD) are firstly described separately, because they constitute a hybrid scheme. The 2CD scheme for the convective term of any physical quantity ϕ can be written as follows:

$$u\frac{\partial \phi}{\partial x} = u_i \frac{\phi_{i+1} - \phi_{i-1}}{2\Delta x} \tag{2-43}$$

By performing a Taylor expansion for the right-hand side of Eq.(2-43), the dominating truncation error of the 2CD scheme can be obtained:

$$TE_{2CD} = -\frac{u\Delta x^2}{6}\frac{\partial^3 \phi}{\partial x^3} \tag{2-44}$$

Obviously, the truncation error of the 2CD scheme contains the 3rd-order derivative which has no numerical diffusive effect. Therefore, the numerical instability probably occurs if using a pure 2CD scheme for a relatively coarse mesh.

On the other hand, the 1UD scheme for the convective term of any physical quantity ϕ can be written as follows:

$$u\frac{\partial \phi}{\partial x} = u_i \frac{\phi_{i+1} - \phi_{i-1}}{2\Delta x} - \frac{|u_i|\Delta x}{2}\frac{\phi_{i+1} - 2\phi_i + \phi_{i-1}}{\Delta x^2} \tag{2-45}$$

Similarly, the dominant truncation error of the 1UD scheme can also be obtained:

$$TE_{1UD} = \frac{|u|\Delta x}{2}\frac{\partial^2 \phi}{\partial x^2} \tag{2-46}$$

The truncation error of the 1UD scheme includes a 2nd-order derivative and hence has the same form as the physical diffusion. The 1UD scheme has good numerical stability due to the strong numerical diffusive effect, but leads to a low accuracy.

In view of these, a hybrid scheme, which is capable of incorporating the respective advantages of the 2CD and 1UD schemes, can be expressed as follows:

$$u\frac{\partial \phi}{\partial x} = \alpha_{bf} * 2CD + (1-\alpha_{bf}) * 1UD \tag{2-47}$$

Here, the blending factor α_{bf} varies between 0 and 1.0. The balance of high accuracy and good numerical stability can be maintained by choosing a proper blending factor when using the hybrid scheme.

2-4-2 TVD 2nd-Order Accurate Upwind Difference Scheme

At first, the ordinary 2nd-order accurate upwind scheme (2UD) is described. The 2UD scheme for the convective term of any physical quantity ϕ can be written as follows:

$$\begin{aligned} u\frac{\partial \phi}{\partial x} = & u_i \frac{-\phi_{i+2} + 4(\phi_{i+1} - \phi_{i-1}) + \phi_{i-2}}{4\Delta x} \\ & + \frac{|u_i|}{4} \frac{\phi_{i+2} - 4\phi_{i+1} + 6\phi_i - 4\phi_{i-1} + \phi_{i-2}}{\Delta x} \end{aligned} \tag{2-48}$$

By implementing a Taylor expansion for the right-hand side of Eq.(2-48), the dominating truncation error of the 2UD scheme can be obtained:

$$TE_{2UD} = \frac{u\Delta x^2}{3}\frac{\partial^3 \phi}{\partial x^3} \tag{2-49}$$

Similar to the 2CD scheme, the truncation error of the 2UD scheme also contains the 3rd-order derivative. Hence, numerical instability also easily occurs when applying the 2UD scheme for a relatively coarse mesh. Hence, similar to the hybrid scheme, blending of 2UD and 1UD schemes can also produce a TVD 2nd-order upwind difference scheme below, which is capable of maintaining both high numerical accuracy and good stability.

$$u\frac{\partial \phi}{\partial x} = \Phi * 2UD + (1-\Phi) * 1UD \tag{2-50}$$

where the parameter Φ is equivalent to the blending factor α_{bf} in Eq.(2-47) and can be evaluated from Eq.(2-52) below. In the finite volume method (FVM), Eq.(2-50) can be rewritten in integral form. Specifically, the cell face value ϕ_F can be evaluated from the following equation:

$$\phi_F = \phi_{UC} + (\nabla\phi)_{UC}\vec{r}\Phi \tag{2-51}$$

where ϕ_{UC} and $(\nabla\phi)_{UC}$ are the cell-centered value and its gradient in the upstream cell, $\vec{r}$ is the displacement vector from the upstream cell center to the surface center and Φ the flux limiter. Obviously, Eq.(2-51) becomes the 1UD scheme for $\Phi = 0$ and the 2UD scheme for $\Phi = 1$. The slope limiter [136] used is as follows:

$$\Phi = \frac{2\Delta_+\Delta_- + \varepsilon}{\Delta_+^2 + \Delta_-^2 + \varepsilon} \tag{2-52}$$

$$\varepsilon^2 = (K\Delta x)^3 \tag{2-53}$$

$$\Delta_- = (\nabla\phi)_{UC}\vec{r} \tag{2-54}$$

$$\Delta_+ = \begin{cases} \phi_{\max} - \phi_{UC} & if\ \Delta_- > 0 \\ \phi_{\min} - \phi_{UC} & if\ \Delta_- < 0 \end{cases} \tag{2-55}$$

$$\phi_{\max} = \max(\phi_{UC}, \phi_{DC}) \tag{2-56}$$

$$\phi_{\min} = \min(\phi_{UC}, \phi_{DC}) \tag{2-57}$$

where K is the model parameter (the recommended value being 0.3), Δx the mesh size and ϕ_{DC} the cell-centered value in the downstream cell.

In the TVD 2UD scheme, the slope limiter Φ is automatically calculated as a function of the local flow field and thus there is no need to give its value beforehand. However, it is perhaps desirable to limit Φ within a specified range to surely maintain both high accuracy and good numerical stability, depending on the situation.

Chapter 3 Proposal of Generalized Classification Method of Flow Pattern for Thermal Loading Evaluation

3-1 Introduction

As described in **Chapter 1**, tee junctions are widely used for mixing of fluids with different temperatures in various industries including nuclear power and process plants. The incomplete mixing of hot and cold fluids at tee junctions causes fluid temperature fluctuations that may result in high cycle thermal fatigue (HCTF) in pipes. There have occurred many thermal fatigue incidents in nuclear plants [11] [12] [13] [14] [15] and chemical plants [17]. Therefore, it is necessary to evaluate the integrity of structures with such potential HCTF.

In view of this, the Japan Society of Mechanical Engineers (JSME) published 'Guideline for Evaluation of High Cycle Thermal Fatigue of a Pipe (JSME S017)' [119] applicable to 90° tee junctions (T-junctions), in 2003. In JSME S017, one of the important procedures of thermal fatigue evaluation is classification of the flow pattern at a T-junction for evaluating thermal loading. Because the extent of damage caused by thermal fatigue is different for different flow patterns, even though the temperature difference between the incoming fluids from main and branch pipes is identical. When the mixing takes place near the pipe wall surface, the fluid temperature fluctuations caused by incomplete mixing are easily transferred to the structure and, hence, the risk of thermal fatigue will be high. Here, classification of the flow pattern is to identify whether the mixing zone of hot and cold fluids from the main and branch pipes is near the wall surface of main pipe or away from the wall surface.

The currently accepted approach for the flow pattern classification is to classify the flow patterns into different groups, based on the momentum ratio (refer to Eqs.(3-1)~(3-3) in **Subsection 3-2**) between the main and branch pipes. Several authors [19] [74] [111] have classified them into three groups: wall jet, deflecting jet and impinging jet, as shown in **Table 3-1**. Other authors (e.g. [112]) have classified them into four groups: wall jet, re-attached jet, turn jet and impinging jet as shown in **Table 3-2**. It should be noted that all these classification

methods of flow patterns are not based on the theoretically exact derivations, but based on visualizations or experimental observations. In JSME S017, the classification of flow patterns is based on the former classification method (Criteria 1 shown in **Table 3-1**), or the three-group classification method.

Table 3-1 Criteria 1 for T-junctions [19]

Wall jet	$1.35 \leq M_R$
Deflecting jet	$0.35 < M_R < 1.35$
Impinging jet	$M_R \leq 0.35$

Table 3-2 Criteria 2 for T-junctions [112]

Wall jet	$4.0 \leq M_R$
Re-attached Jet	$1.35 < M_R < 4.0$
Turn jet	$0.35 < M_R \leq 1.35$
Impinging jet	$M_R \leq 0.35$

The conventional characteristic equations used for calculation of the momentum ratio between main and branch pipes are only applicable to 90° tee junctions (T-junctions). A small amount of work undertaken by Oka [113] has investigated the effect on energy loss of angled tee junctions. However, work has not yet been done regarding the classification of tee junctions with angles other than 90° (Y-junctions).

It seems that almost only T-junctions are used in nuclear power plants. However, Y-junctions especially with a 45° branch angle, are also used for mixing hot and cold fluids in process plants, such as petrochemical plants, refineries and LNG plants, to mitigate erosion of the main pipe due to impingement of the branch pipe flow against the main pipe and reduce the pressure drop produced by mixing fluids. It is imperative to evaluate the structural integrity of Y-junctions in the operating plants and newly designed plants by extending the existing guideline JSME S017. Therefore, it is essential to establish a generalized classification method of flow patterns applicable to both T-junctions and Y-junctions.

It should be pointed out that the present research is not to pursue a theoretically exact classification of flow pattern at a tee junction, which is meant to exactly distinguish the

transition between two adjacent flow patterns. Here, the eventual aim of classifying flow pattern at a tee junction is to implement the thermal fatigue evaluation in engineering applications. Therefore, as a conservative classification, it is acceptable and desirable to classify the grey zone of visual observation between wall jet and deflecting jet as wall jet, and classify the grey zone between impinging jet and deflecting jet as impinging jet, in view of the facts that both the wall jet and impinging jet are more damaging flow patterns than the deflecting jet.

The objective of the present chapter is to propose generalized characteristic equations for classifying flow patterns at a tee junction with any angle of branch pipe. Furthermore, CFD simulations of T-junction and Y-junction flows are carried out to investigate the validity of the proposed characteristic equations.

3-2 Proposal of the Generalized Characteristic Equations for Classifying Flow Patterns

3-2-1 Conventional Characteristic Equations

Based on the momentum ratio of the main pipe flow to the branch pipe flow, the conventional characteristic equations for classifying the flow patterns of T-junctions can be expressed as follows [19]:

$$M_m = D_m D_b \rho_m V_m^2 \tag{3-1}$$

$$M_b = \frac{\pi}{4} D_b^2 \rho_b V_b^2 \tag{3-2}$$

$$M_R = M_m / M_b \tag{3-3}$$

In JSME S017 [119], these characteristic equations, together with Criteria 1 shown in **Table 3-1,** have been adopted for determining the flow patterns of T-junctions. However, these characteristic equations are only applicable for the classification of the flow patterns of T-junctions. It is necessary to understand the physical meanings of Eqs.(3-1)~(3-3) very well, prior to generalizing them to include Y-junctions.

3-2-2 Understanding of the Phenomena Behind the Momentum Ratio

For understanding the physical phenomena behind the momentum ratio, the mechanism of the interaction of momentum of main and branch pipes was investigated. The momentum of fluid flowing through a pipe can generally be expressed as follows:

(momentum per unit time) = (volumetric flow rate) × (momentum per unit volume)

For a main pipe shown in **Fig. 3-1**, $(D_m D_b)$ is the projection area of the branch pipe on the cross-section of the main pipe when imaging that the branch pipe is fully extended into the main pipe and, thus, represents the area of main pipe flow interacting with branch pipe flow. $(D_m D_b V_m)$ is the volumetric flow rate of the main pipe stream interacting with the branch pipe flow. $(\rho_m V_m)$ is the momentum per unit volume of fluid flowing into the main pipe. Hence, M_m represents the momentum per unit time of main pipe fluid interacting with the branch pipe stream as follows:

$$M_m = (D_m D_b V_m) \cdot (\rho_m V_m) \tag{3-4}$$

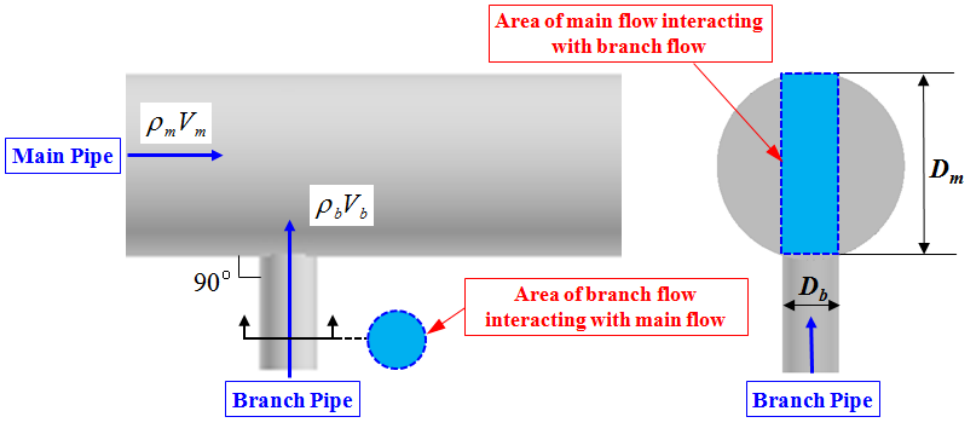

Fig. 3-1 Illustration for Investigation into the Interacting Mechanism of Momentum between Main and Branch Pipes for T-Junctions

For a branch pipe shown in **Fig. 3-1**, $(\pi D_b^2 / 4)$ is the cross-sectional area of the branch pipe and also the area of the branch pipe stream interacting with the main pipe stream. $(\pi D_b^2 V_b / 4)$ is the volumetric flow rate of the branch pipe stream interacting with the main pipe stream. $(\rho_b V_b)$ is the momentum per unit volume of fluid flowing into the branch pipe. As a result, M_b

represents the momentum per unit time of the branch pipe fluid interacting with the main pipe stream as follows:

$$M_b = (\frac{\pi}{4} D_b^2 V_b) \cdot (\rho_b V_b) \quad (3\text{-}5)$$

Here, equations (3-4) and (3-5), above, are equivalent to equations (3-1) and (3-2) respectively.

3-2-3 Proposal of the Generalized Characteristic Equations

Here, the task to be done is to extend equations (3-4) and (3-5) for T-junctions to Y-junctions based on the interacting mechanism of momentum of fluids from main and branch pipes. For the case of Y-junctions, shown in **Fig. 3-2**, the momentum M_m of main pipe stream interacting with branch pipe stream is evidently the same as that in Eq.(3-4) for a T-junction. However, the momentum M_b of the branch pipe stream interacting with the main pipe stream needs to be re-defined by considering the branch pipe jet direction relative to the main pipe stream. The first term $(\frac{\pi}{4} D_b^2 V_b)$ on the right-hand side (RHS) of Eq.(3-5) is the volumetric flow rate of the branch pipe stream, which is a scalar, and hence needs no modification. On the other hand, the second term $(\rho_b V_b)$ on the RHS of Eq.(3-5) is the momentum per unit volume of fluid flowing into the branch pipe, which is a vector, and hence needs to be modified. The momentum of branch pipe stream contributing to the interaction with the main pipe stream is the component $(\rho_b V_b \sin\alpha)$ perpendicular to the main pipe stream. Therefore, it is found that M_b for a Y-junction should be written as follows:

$$M_b = (\frac{\pi}{4} D_b^2 V_b) \cdot (\rho_b V_b \sin\alpha) \quad (3\text{-}6)$$

As a result, the characteristic equations for classifying the flow patterns of Y-junctions are as follows:

$$M_m = D_m D_b \rho_m V_m^2 \quad (3\text{-}7)$$

$$M_b = \frac{\pi}{4} D_b^2 \rho_b V_b^2 \sin\alpha \quad (3\text{-}8)$$

$$M_R = M_m / M_b \tag{3-9}$$

When the branch angle is 90° (or $\alpha = 90^\circ$), $\sin\alpha$ in Eq.(3-8) is equal to 1.0, and as a result, Eqs.(3-7)~(3-9) become identical to Eqs.(3-1)~(3-3). Therefore, it is obvious that Eqs.(3-7)~(3-9) are the generalized characteristic equations which are applicable to both T-junctions and Y-junctions.

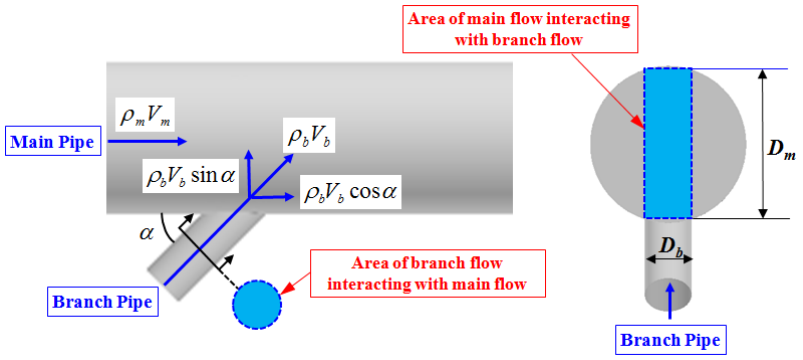

Fig. 3-2 Illustration Accounting for the Definition of Momentum Ratio for Y-Junctions

3-3 Methods for Confirming the Validity of Proposed Characteristic Equations

3-3-1 Computational Models

In the present chapter, CFD simulations of flow and temperature fields were used to confirm the validity of Eqs.(3-7)~(3-9) for classifying the flow patterns of Y-junctions. CFD simulations were carried out for both Y-junctions and T-junctions, to compare the flow patterns of Y-junctions with those of T-junctions for the same momentum ratios. Flow patterns for T-junctions have been identified through the experiments and numerical simulations by many authors [19, 67, 74, 88, 89], so they can be regarded as the basis of comparison. For Y-junctions, three models, with branch angles of $\alpha = 30^\circ, 45^\circ, 60^\circ$ were investigated to verify the general validity of Eqs.(3-7)~(3-9). Selection of branch angles for CFD verification was based on the fact that most of the Y-junctions used in process plants is 45° branch angle and a few is 60°. The Y-junctions with branch angle below 45° are not yet used for mixing of hot and cold fluids in process plants because it is difficult to ensure sufficient welding strength of junctions with small branch angle. Additionally, a very small branch angle is also unfavorable for mixing of fluids

with different temperatures and, as a result, a longer straight pipe downstream of junction is needed for achieving full mixing, which can lower the economic efficiency of plant layout.

The computational models for 90° T-junction and 45° Y-junction (as an example of three Y-junctions) are shown in **Fig. 3-3**. The length of the inlet section is taken as $2D_m$ (D_m=0.4m) for the main pipe and $2D_b$ (D_b=0.12m) for the branch pipe, and the length of the outlet section is taken as $10D_m$ for the models of T-junction and three Y-junctions. The flow patterns investigated here are determined by the momentum ratio between two streams from main pipe and branch pipe [83] and, thus, are independent of the ratio of D_m to D_b. The diameters (D_m and D_b) of main and branch pipes used here are close to those at a T-junction in an industrial plant.

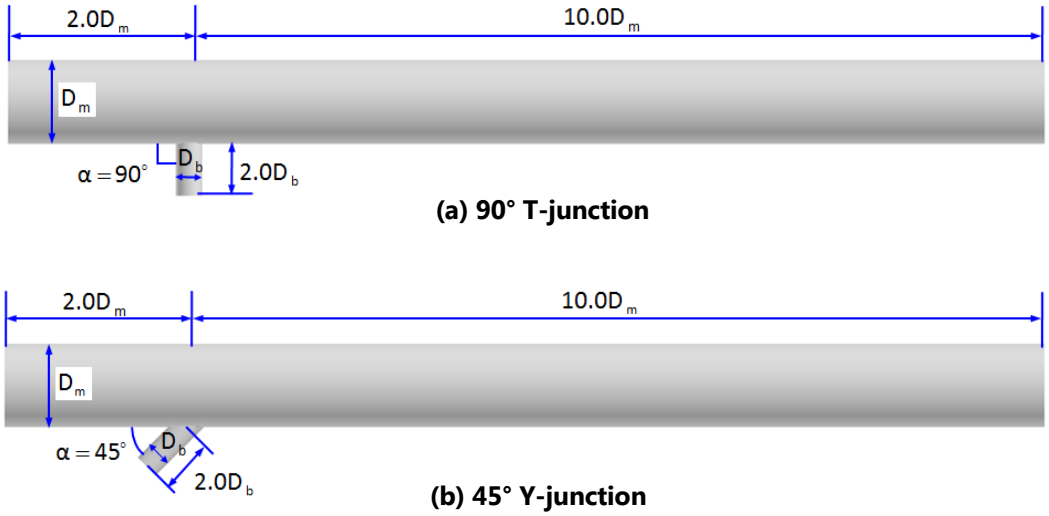

Fig. 3-3 Computational Models of the Tee Junctions

3-3-2 CFD Simulation Methods

Since the lengths of the inlet and outlet sections are relatively short, some measures are taken when setting the inlet and outlet boundary conditions. As the fully developed turbulent flow, a 1/7-power law [137] is applied for the inlet velocity profile to reduce the effects of the short inlet section as much as possible. At the same time, a free outflow condition was applied at the outlet. Specifically, the condition of zero-gradient along the direction normal to the outlet for each quantity (including velocity components, pressure and temperature) is applied.

Here, the CFD simulations aim mainly at confirming the flow patterns noted above, so the steady-state calculations are considered sufficient. The turbulence model used is the realizable $k-\varepsilon$ (RKE) turbulence model [129] rather than the standard $k-\varepsilon$ (SKE) turbulence model [127]. As described in **Chapter 2**, the SKE model provides poor predictions for the complex flows with strong separation, but the RKE model, however, is capable of more reasonably predicting the turbulent eddy viscosity and improves the prediction performance for flows with strong separation. In fact, the prediction accuracy of the RKE-based simulation has been verified to be sufficient for the present investigations by comparison with both the experimental results and the time-averaged results of LES simulation. The details for the verification of RKE-based prediction accuracy are shown in **Appendix 3-1**.

Half models are used in the present research, based on the geometrical symmetry. Meshes for 90° T-junction and 45° Y-junction (as an example of three Y-junctions) are shown in **Fig. 3-4**. The near-wall cell size for the meshes is $y^+ < 40$, and hence, such meshes are sufficiently fine for the $k-\varepsilon$ model. The number of cells of the mesh is nearly 350,000 for the models of T-junction and three Y-junctions. The results for mesh sensitivity study show that it is adequate to use the mesh with nearly 350,000 cells for the present simulations. The details for the mesh sensitivity study are shown in **Appendix 3-2**.

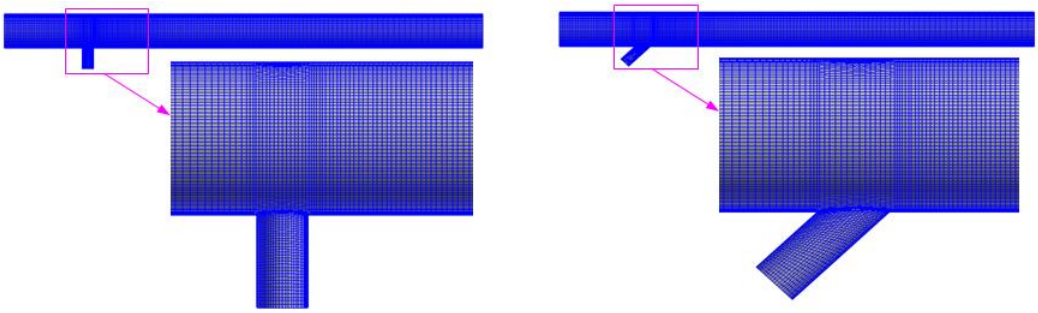

(a) 90° T-junction (b) 45° Y-junction

Fig. 3-4 Meshes for the Computational Models

The fluid used for CFD simulations is water. The water temperatures at the main pipe and branch pipe inlets are 50°C and 20°C, respectively. The fluid density and viscosity are 1000 kg/m^3 and 0.001 Pa.sec, separately, for the fluid physical properties used for the CFD

simulations. The main numerical methods used in the present simulations are described in **Table 3-3**.

Table 3-3 Main Numerical Methods Used

CFD Code	Modified FrontFlow/Red [138] (See **Appendix A** for its details)
Simulation Mode	Steady-State Simulation
Turbulence Model	Realizable $k-\varepsilon$ Turbulence Model
Spatial Discretization Method	Convective Term: 1st-Order Accurate Upwind Differencing Other Terms: 2nd-Order Accurate Central Differencing

In the CFD simulations, the iterative solution was performed for any quantity ϕ (including velocity components, pressure, temperature, turbulent kinetic energy (k) and its dissipation rate (ε)). The root-mean-square (RMS) normalized residual used for the convergence judgment is defined as follows:

$$\varepsilon_{\phi}^{*}=\sqrt{\sum_{i=1}^{N}[(\phi_i^n-\phi_i^{n-1})/\phi_i^n]^2\Big/N} \tag{3-10}$$

where N is the total number of mesh cells to be solved, n and n-1 represent the current and last iterations, respectively. The convergence criteria were set as 1.0×10^{-5} for each velocity component, temperature, turbulent kinetic energy (k), its dissipation rate (ε), and 1.0×10^{-7} for pressure, respectively.

3-4 CFD Simulation Results and Discussions

The present simulations mainly aim to confirm the validity of Eq.(3-7)~Eq.(3-9) for classifying the Y-junction flow patterns. The flow patterns of 60°, 45° and 30° Y-junctions are compared with the flow patterns of the 90° T-junction for the same momentum ratio M_R. CFD simulations of 6 cases with different M_R values have been implemented for both T- and Y-junctions. The six M_R values (**Table 3-4**) around and near the three bounds (4.0, 1.35 and 0.35) in Criteria 2 (**Table 3-2**) were selected for the simulations. The two bounds in Criteria 1 (**Table 3-1**) are included in Criteria 2. The velocity at the main pipe inlet is fixed at 0.32m/sec (Re=128,000) for all cases. The velocity at the branch pipe inlet for all cases was calculated using Eqs.(3-7)~(3-9) for each

M_R value. The velocities and Reynolds numbers at the branch pipe inlets for 90° T-junction and 45° Y-junction (as an example of three Y-junctions) are listed in **Table 3-4** below.

Table 3-4 Velocities and Reynolds Numbers at Branch Pipe Inlets

Case No.	M_R	90° T-junction		45° Y-junction	
		V_b [m/s]	Reynolds Number [-]	V_b [m/s]	Reynolds Number [-]
Case 1	4.20	0.318	38,160	0.378	45,360
Case 2	3.80	0.334	40,080	0.397	47,640
Case 3	1.45	0.541	64,920	0.643	77,160
Case 4	1.25	0.582	69,840	0.692	83,040
Case 5	0.38	1.056	126,720	1.256	150,720
Case 6	0.33	1.133	135,960	1.348	161,760

It should be pointed out that, in the present investigation, the judgment of whether or not the flow patterns between T- and Y-junctions are similar is based on the impact of flow patterns on thermal fatigue. Here, the flow patterns are different from the usually called flow distributions or flow features. Specifically, the flow patterns stated here means whether the branch jet is bent near the main pipe wall on the same side as branch pipe (or Wall Jet) due to very strong main pipe jet, or the branch jet flows through the central part (or bulk) of main pipe (or Deflecting Jet) due to intermediately strong main pipe jet, or the branch jet impinges against the opposite side wall of main pipe (or Impinging Jet) due to weak main pipe jet.

In addition, the area of observation for classification of flow patterns is from mixing junction to 3.0D_m downstream of the junction here, as the results of experiments [19, 83] and numerical simulations (see **Fig. 5-9** in Chapter 5) have shown that the fluid temperature fluctuations are greatly attenuated within 2.0D_m downstream of the junction. For example, **Fig. 3-5** shows that axial distributions of maximum normalized fluid temperature fluctuation intensity (T^*_{rms}, as defined in Eq.(4-7) in Chapter 4) among circumferential positions 1mm away from the pipe wall, and they were the experimental results for three types of flow patterns obtained by Kamide et al. [83]. The peak was located at about 0.75Dm downstream for the wall jet case and at about 0.5Dm downstream for the impinging jet case. The deflecting jet case showed the lowest peak and hence had the least risk of thermal fatigue. The fluid temperature fluctuation intensity was

significantly attenuated at $2.0D_m$ downstream of the junction for all the three cases. Hence, it is sufficient to observe the flow patterns up to $3.0D_m$ downstream of the junction for thermal fatigue evaluation.

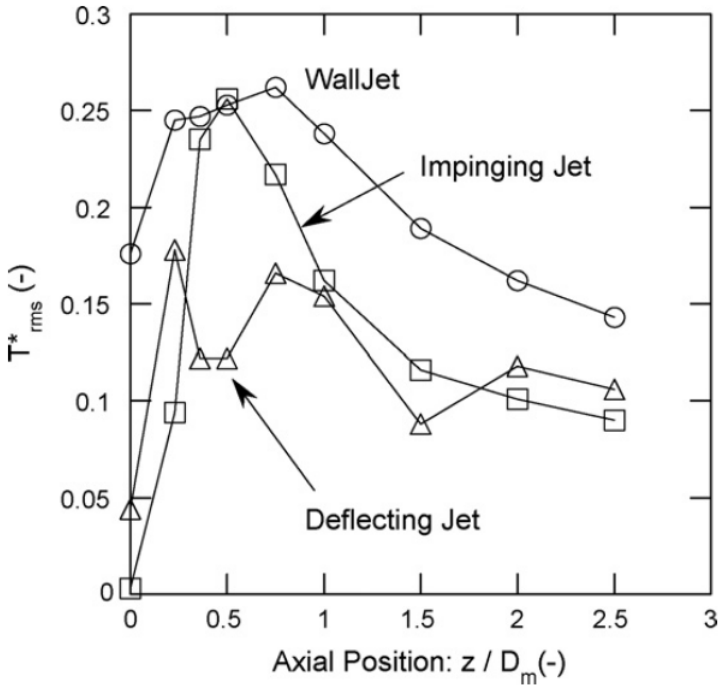

Fig. 3-5 Axial Distributions of Maximal Fluid Temperature Fluctuation Intensity among Circumferential Positions [83]

The simulation results have been visualized. The fluid temperature distributions and velocity vectors are shown in **Figs. 3-6 ~ 3-11**. The flow patterns are confirmed based on both the velocity vectors and the temperature distributions, with focus on viewing whether or not the branch jet flow is near the main pipe wall after being injected into the main pipe flow. The flow patterns for each M_R value are described below.

For the momentum ratios of M_R=4.20 (**Fig. 3-6**) and M_R=3.80 (**Fig. 3-7**), the 60°, 45° and 30° Y-junctions and 90° T-junction have similar flow patterns, and the branch jet is bent to the main pipe wall on the side of branch pipe due to relatively high flow velocity from the main pipe. However, the branch jet flow at M_R=3.80 is slightly away from the wall, relative to that at M_R=4.20. In addition, mixing zones for all the three Y-junctions are a little away from the pipe wall, compared with T-junction, for both M_R=4.20 and M_R=3.80. Hence, it is slightly conservative

and thus proper to classify flow patterns for all the three Y-junctions as the same as those for the T-junction for thermal fatigue evaluation, at M_R=4.20 and M_R=3.80, respectively.

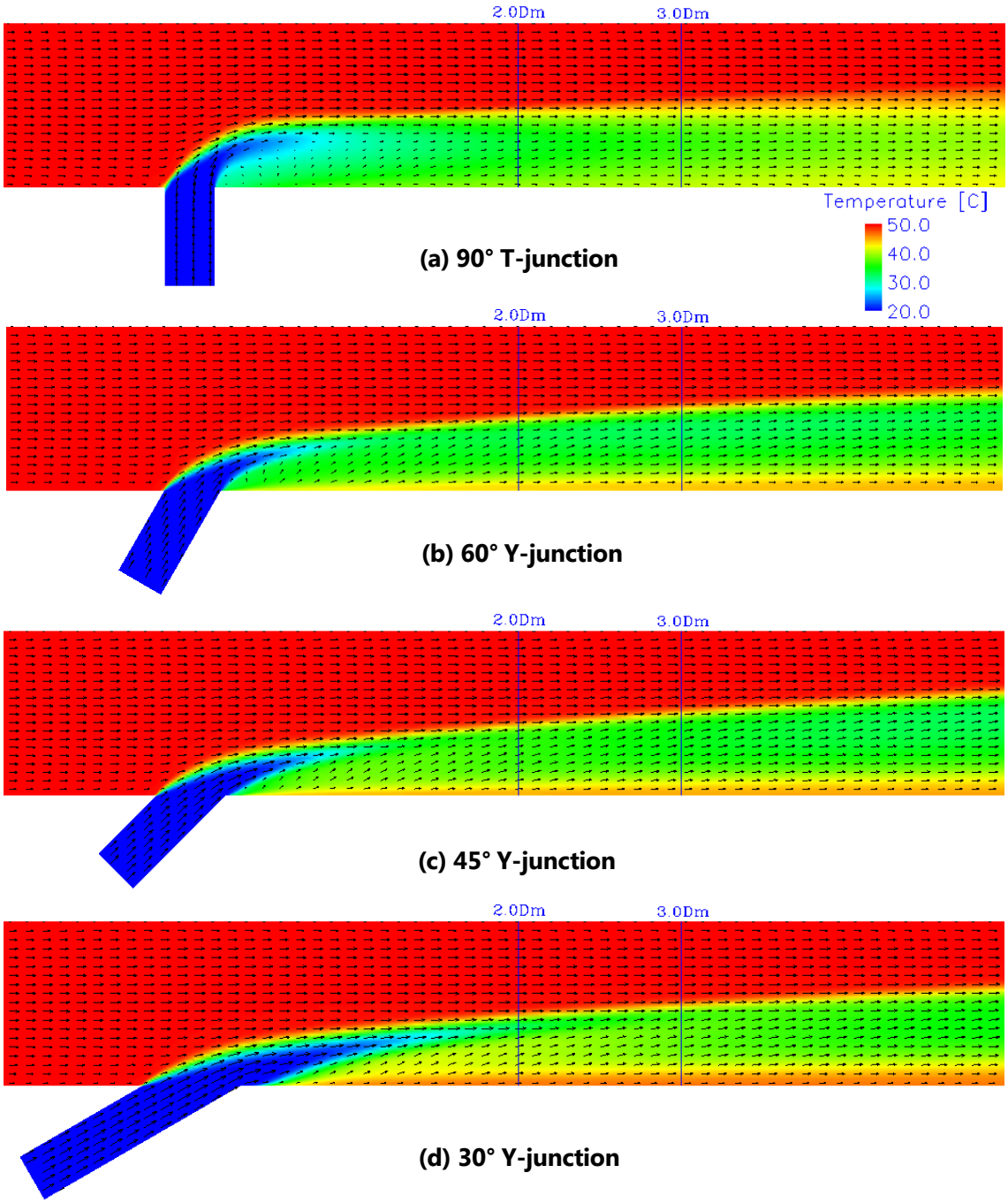

Fig. 3-6 Fluid Temperature Distribution and Velocity Vectors for M_R=4.20

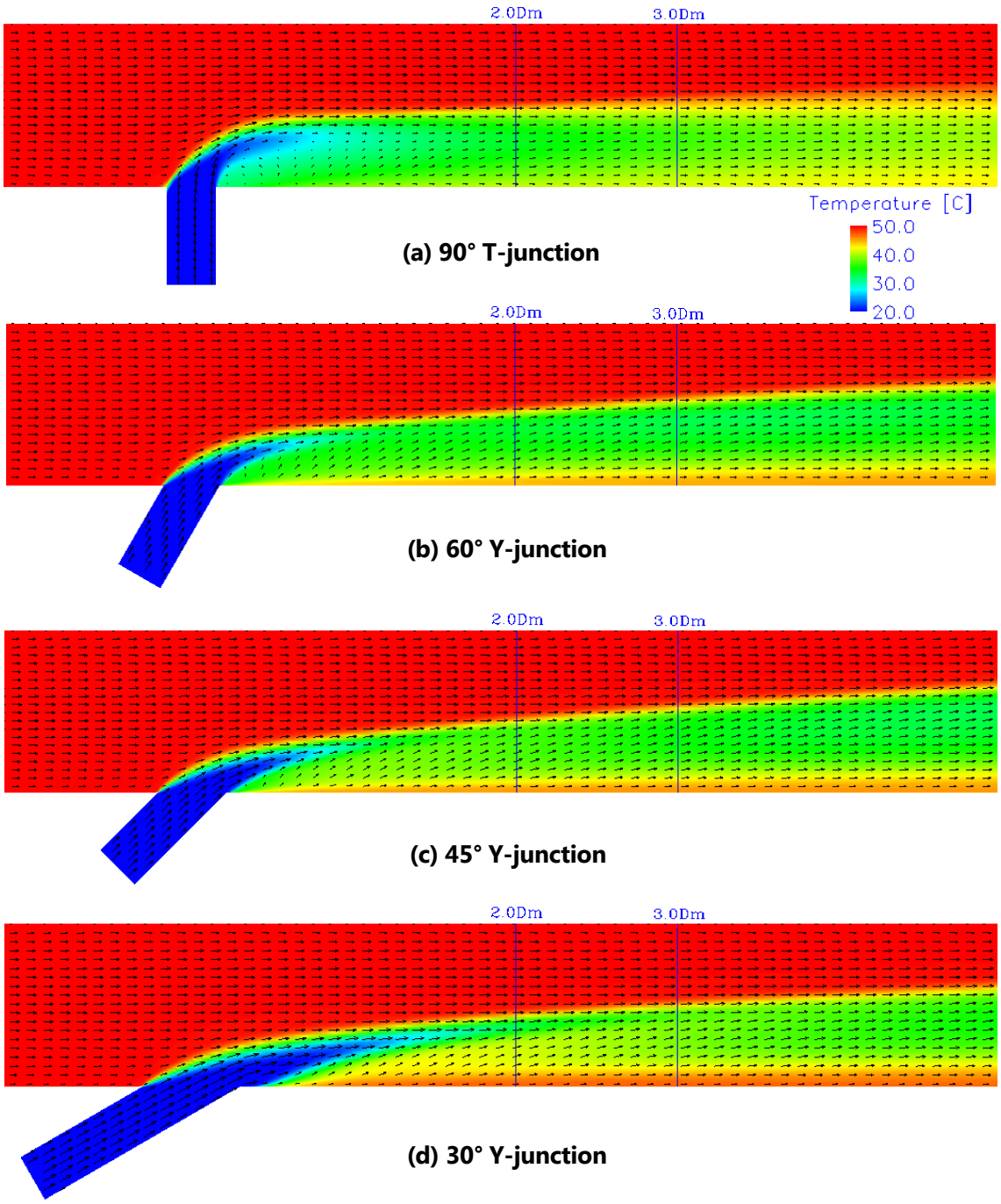

Fig. 3-7 Fluid Temperature Distribution and Velocity Vectors for M_R=3.80

For M_R=1.45 (**Fig. 3-8**) and M_R=1.25 (**Fig. 3-9**), the 60°, 45° and 30° Y-junctions and T-junction also have similar flow patterns, and the branch jet flows through the central part in the main pipe for both. In these cases, the Y-junction and T-junctions have comparable momentums. By the way, it should be pointed out that, although the branch jet reaches the opposite pipe wall downstream of junction for the Y-junctions, the location where the branch jet reach the pipe wall

is over 4.0D_m downstream of junction, where the fluid temperature fluctuations have greatly been attenuated. Such a location far downstream is beyond the area of flow pattern classification for thermal fatigue evaluation. Hence, it is proper to classify flow patterns for all the three Y-junctions as the same as those for the T-junction for thermal fatigue evaluation, at M_R=1.45 and M_R=1.25, respectively.

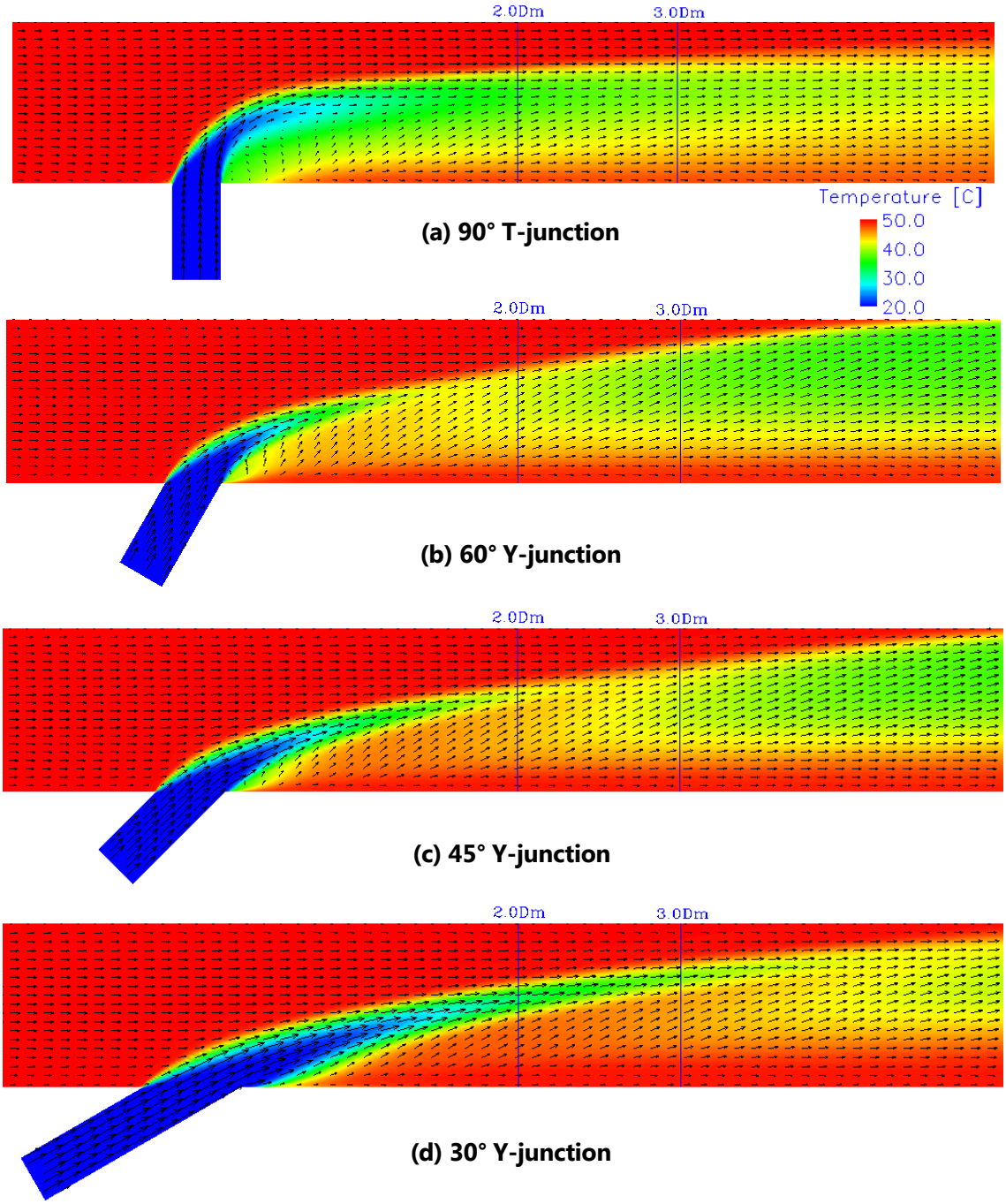

Fig. 3-8 Fluid Temperature Distribution and Velocity Vectors for M_R=1.45

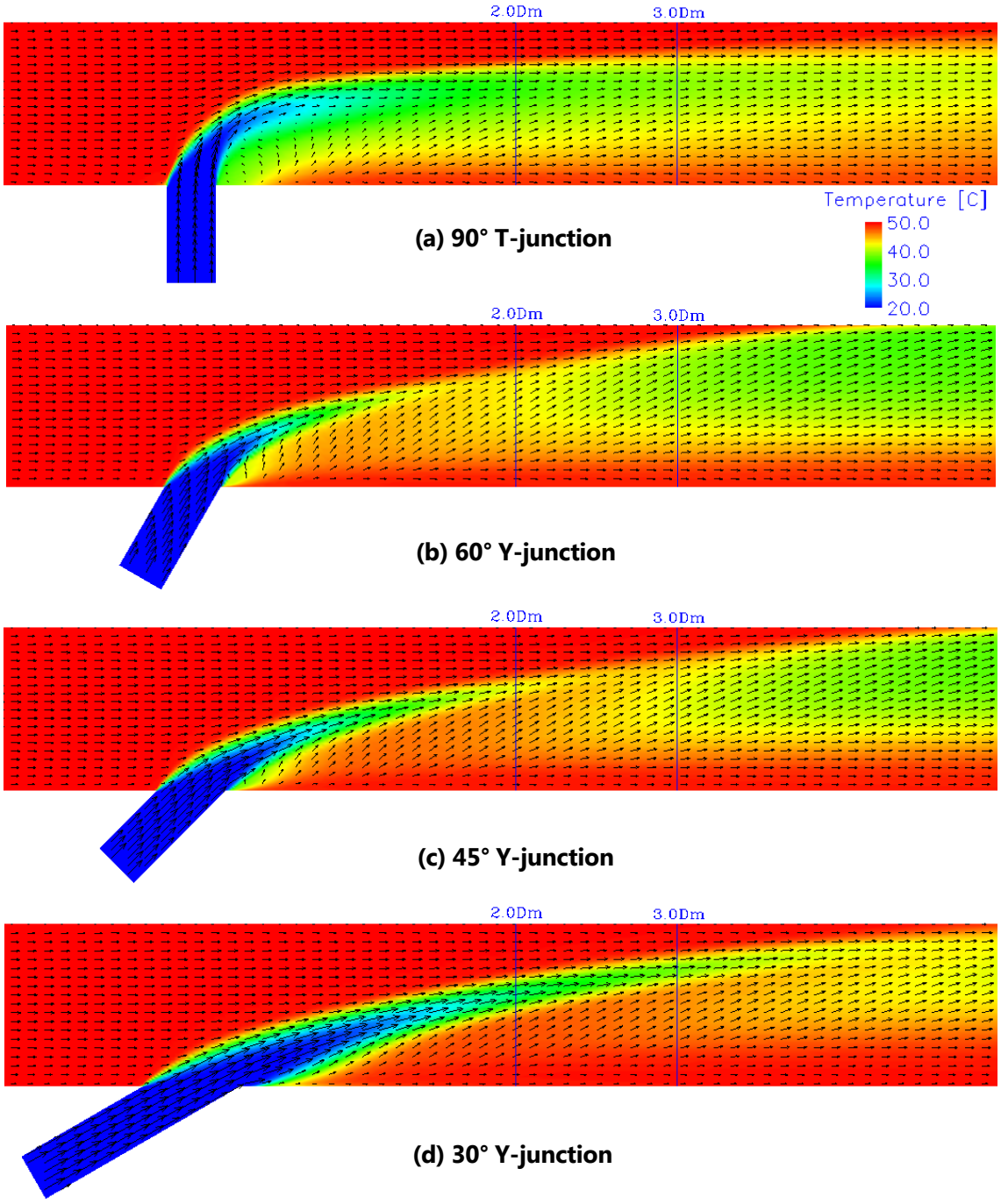

Fig. 3-9 Fluid Temperature Distribution and Velocity Vectors for M_R=1.25

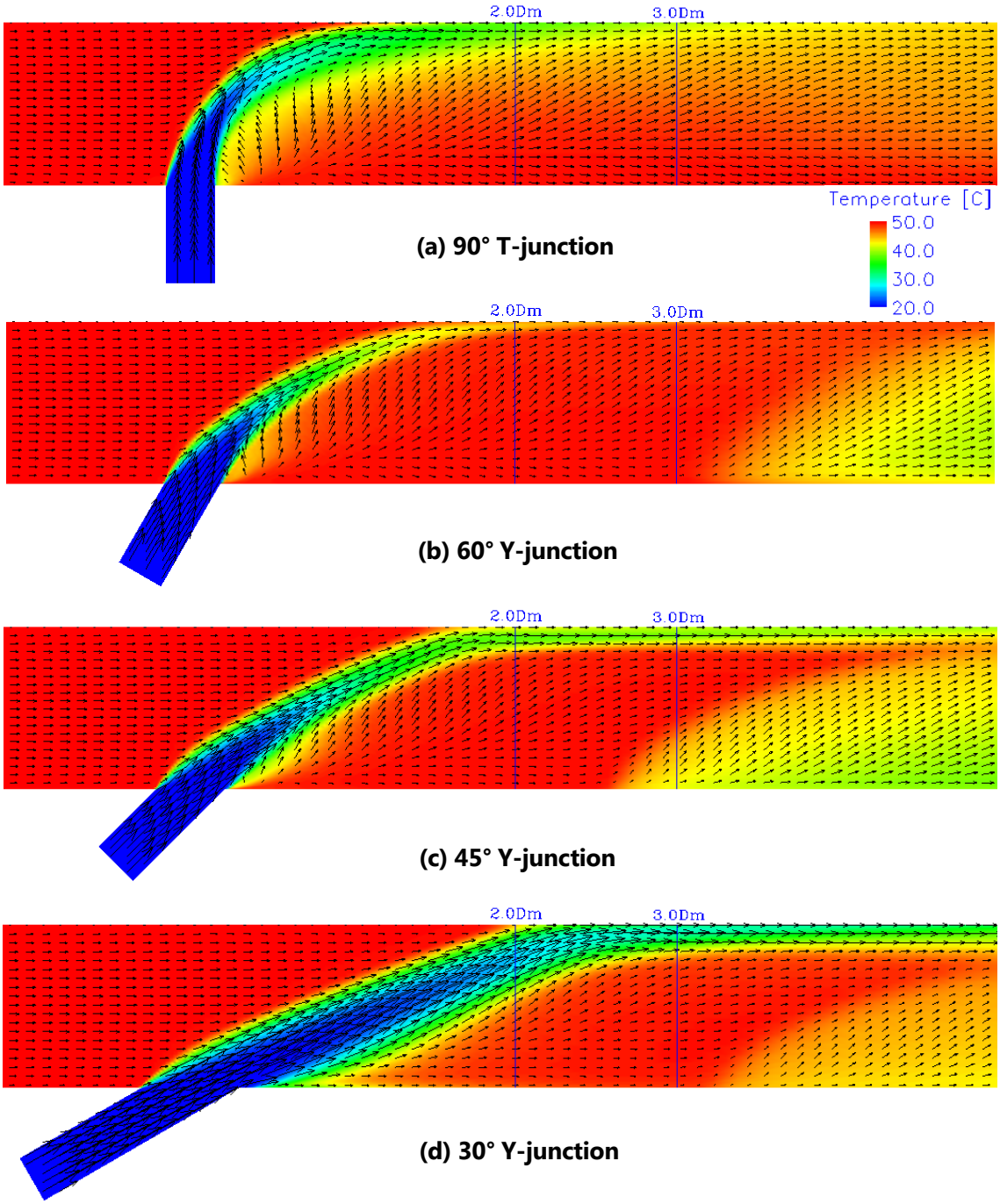

Fig. 3-10 Fluid Temperature Distribution and Velocity Vectors for M_R=0.38

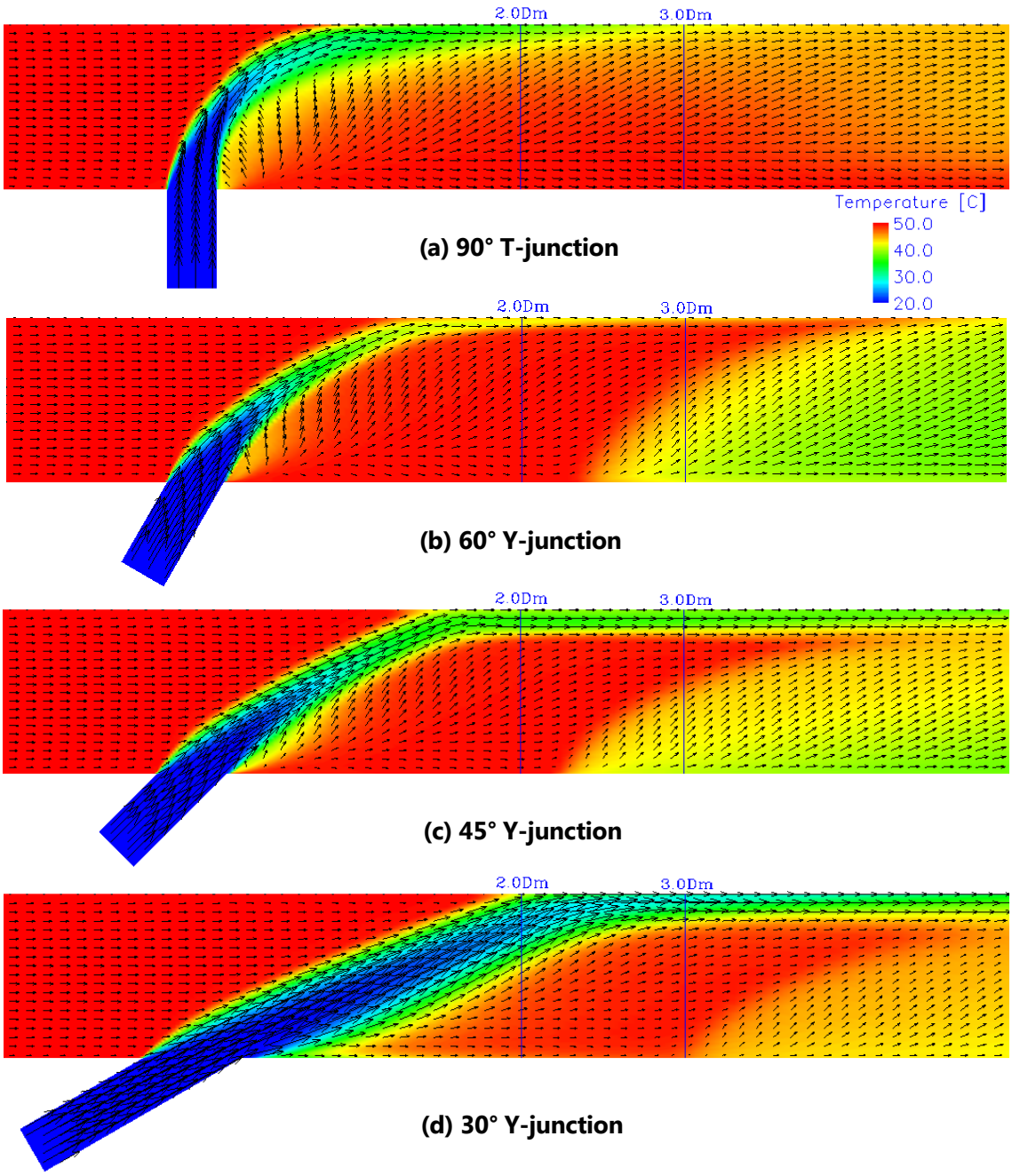

Fig. 3-11 Fluid Temperature Distribution and Velocity Vectors for M_R=0.33

For M_R=0.38 (**Fig. 3-10**) and M_R=0.33 (**Fig. 3-11**), the 60°, 45° and 30° Y-junction and T-junction have similar flow patterns as well and the branch jet impinges on the opposite wall of the main pipe due to relatively high flow velocity from the branch pipe. However, the branch jet flow at M_R=0.38 slightly moves away from the wall, compared to that at M_R=0.33. It can be found that the location where the branch jet impinges on the opposite pipe wall moves toward further downstream with decrease of branch angle for Y-junctions. It is considered that the fluid

temperature fluctuations at Y-junctions are partly attenuated through mixing in the bulk of fluid, before impinging on the pipe wall. The branch jet impinges on the opposite pipe wall relatively weakly for 60° Y-junction and nearly equivalently for 45° Y-junction, compared with 90° T-junction. However, it seems that the cold branch jet strongly impinges on the opposite pipe wall for 30° Y-junction, for both M_R=0.38 and M_R=0.33. It is inadequate to judge whether the flow patterns for 30° Y-junction can be classified as the same as those for 90° T-junction, just based on the results obtained from the steady-state CFD simulations. Therefore, the additional unsteady LES simulations were performed for 30° Y-junction and 90° T-junction at M_R=0.38 and M_R=0.33, to compare their fluid temperature fluctuation intensities around the impinging locations. As described in **Appendix 3-3**, the unsteady LES simulation results showed that the fluid temperature fluctuation intensities around the impinging location for 90° T-junction was obviously higher than that for 30° Y-junction. Hence, it is relatively conservative and thus proper to classify flow patterns for 30° Y-junction as the same as those for 90° T-junction for thermal fatigue evaluation, at M_R=0.38 and M_R=0.33, respectively. As a result, it is proper to classify flow patterns just for all the three Y-junctions of 60°, 45° and 30° as the same as those for the T-junction for thermal fatigue evaluation, at M_R=0.38 and M_R=0.33, respectively.

In summary, the flow patterns of 60°, 45° and 30° Y-junctions can be classified as the same as those of 90° T-junctions at the same M_R value for thermal fatigue evaluation, based on the CFD simulation results. Therefore, it can be concluded that Eqs.(3-7)~(3-9) are valid for classifying the flow patterns at T- and Y-junctions of 30°~90°, which is sufficient for practical use in industrial plants (see **Section 3-3-1**).

In addition, the simulation results indicates that Criteria 2 offers a more proper classification of the flow patterns than Criteria 1 does. For the bound of M_R=0.35, both Criteria 1 and Criteria 2, can predict the impinging jet pattern well. However, Criteria 1 could not predict the wall jet pattern well for the bound of M_R=1.35. In contrast, Criteria 2 can predict the wall jet pattern well for the bound of M_R=4.0. Specifically, the flow patterns in **Fig. 3-8** can clearly be classified as a deflecting jet, but Criteria 1 predicts a wall jet for M_R=1.45 (>1.35). On the other hand,

Criteria 2 predicts a reattached jet for M_R=1.45, which corresponds to a deflecting jet. It should be noted that the deflecting jet pattern is divided into two types of flow patterns, reattached jet and turn jet, in Criteria 2. Thus, it can be found that Criteria 1 is relatively conservative compared with Criteria 2, and however, is on the safe side. In the present investigations, Criteria 1, which is currently used in JSME S017, is recommended as the criteria for flow pattern classification of T- and Y-junctions of 30°~90° when applying JSME S017 to evaluate thermal fatigue, and is rewritten as Criteria 3 shown in **Table 3-5**. **Fig. 3-12** shows the flow pattern map based on Eqs.(3-7)~(3-9) and the Criteria 3. The six solid circles shown in **Fig. 3-12** represent the values of M_R for 6 cases in the present investigations.

Table 3-5 Criteria 3 Recommended for Classifying Flow Patterns at T- and Y-junctions of 30° ~ 90°

Wall jet	$1.35 \leq M_R$
Deflecting jet	$0.35 < M_R < 1.35$
Impinging jet	$M_R \leq 0.35$

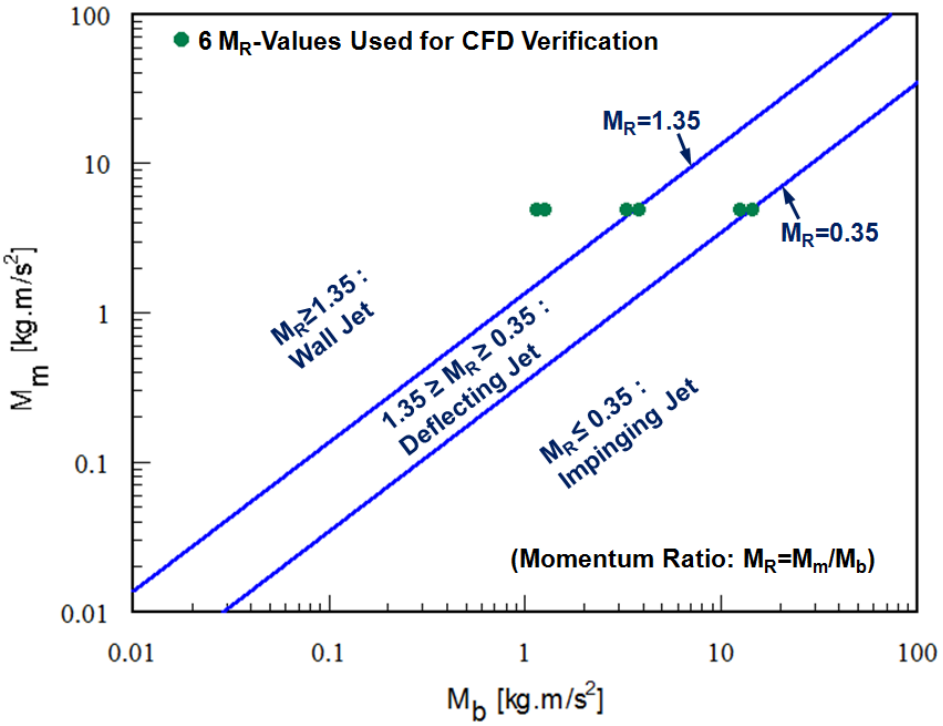

Fig. 3-12 Flow Pattern Map Based on Criteria 3 Shown in Table 3-5

Table 3-6 Computational Conditions for Investigating the Effect of Reynolds Number

M_R	Ratio of Fluid Viscosity [-]	90° T-junction		45° Y-junction	
		Re [-] (Main pipe)	Re [-] (Branch pipe)	Re [-] (Main pipe)	Re [-] (Branch pipe)
0.38	1/20	6,400	6,336	6,400	7,536
0.38	1000	1.28×10^8	1.27×10^8	1.28×10^8	1.51×10^8

Meanwhile, it should be pointed out that, as noted above, classification of the flow patterns here is to identify whether the mixing zone of hot and cold fluids from main pipe and branch pipe is located near the wall surface of main pipe or far away from the wall surface, for evaluating thermal fatigue. Such flow patterns are determined by the momentum ratio between two streams from main pipe and branch pipe [83]. To confirm the effect of Reynolds number, CFD simulations were carried out for 90° T-junction and 45° Y-junction at M_R=0.38 (Case 5 in **Table 3-4**) by adjusting the fluid viscosity, as shown in **Table 3-6**. The verified Reynolds numbers range from about 6,400 to 1.5×10^8. The CFD results show that, if the momentum ratio is kept constant (here M_R=0.38), the time-averaged flow patterns are almost identical for different Reynolds numbers at 90° T-junction and 45° Y-junction, respectively. It can be inferred that this is also true for 60° Y-junction. In industrial plants, the flow at tee junction is usually kept fully turbulent to achieve a good mixing performance and, hence, it is considered that Reynolds number is mostly above 10,000. Moreover, an very high flow velocity is not yet used in order to maintain a proper pressure drop and prevent flow-induced pipe vibration from occurring and, hence, it is considered that Reynolds number is below 1.5×10^8. Therefore, it is proper to consider that flow patterns are almost independent of the flow Reynolds number for engineering applications, if the momentum ratio is kept constant.

Furthermore, Eqs.(3-7)~(3-9) suggest that reducing the angle α of the branch pipe can increase the range of the branch pipe to main pipe velocity ratio V_b/V_m for preserving a less damaging deflecting jet flow pattern, which is an important finding that could be used to extend the current design options for tee junctions where high cycle thermal fatigue may be a concern. This means it is possible to change the flow patterns from the impinging jet to the less damaging

deflecting jet for the same branch pipe to main pipe velocity ratio using a Y-junction instead of a T-junction.

3-5 Summary

In the present investigations, the generalized characteristic equations have been proposed to classify the flow patterns for all angles of tee junctions, including both T-junctions and Y-junctions. The proposed equations have been proven to be valid for predicting the flow patterns for tee junctions with branch angles of 30° ~ 90°, which are sufficient for practical use in industrial plants, by CFD simulations of the flow and temperature fields.

Moreover, the Criteria 3 (**Table 3-5**), which is identical to the Criteria 1 currently used in JSME S017 and is on the safe side, is recommended as the criteria for flow pattern classification of T- and Y-junctions of 30°~90° when applying JSME S017 to evaluate thermal fatigue.

In addition, Eqs.(3-7)~(3-9), shown again below, suggest that adjusting the angle of the branch pipe can increase the range of branch pipe to main pipe velocity ratio to maintain a deflecting jet flow pattern, which is less damaging. This is an important finding that could be used to extend the current design options for tee junctions where high cycle thermal fatigue may be a concern.

$$M_m = D_m D_b \rho_m V_m^2 \tag{3-7}$$

$$M_b = \frac{\pi}{4} D_b^2 \rho_b V_b^2 \sin\alpha \tag{3-8}$$

$$M_R = M_m / M_b \tag{3-9}$$

Appendix 3-1 Validation of Prediction Accuracy of Flow Velocity and Fluid Temperature Profiles at T-Junction Using RKE Turbulence Model

A steady-state CFD simulation of flow and temperature fields at a T-junction was carried out to validate the accuracy of predicting flow velocity profile using the realizable $k-\varepsilon$ (RKE) turbulence model. The simulation conditions shown in **Table 3-7** are the same as those in the experiments conducted by Kamide et al. [83] and in **Chapter 4**. Except the turbulence model, the main numerical methods used in the present simulation are the same as in **Chapter 4**, where the

unsteady CFD simulations were performed using large eddy simulation (LES) sub-grid scale (SGS) turbulence model.

The RKE-based simulation results for normalized flow velocity profile and fluid temperature distribution were compared with the experimental [83] and LES-based CFD simulation results in **Chapter 4** to confirm its prediction accuracy. As shown in **Fig. 3-14**, compared are the normalized time-averaged axial velocity (U_{ave}) and fluid temperature (T_{ave}) distributions along the vertical direction in the cross-section of 0.5Dm downstream from the center-line of branch pipe (see **Fig. 3-13**). Time-averaged axial velocity distributions for the experimental and LES results are used for comparison. Moreover, the LES results used for comparison are those of Case 6, which are closest to the experimental results, for all the 6 cases investigated in **Chapter 4**. **Fig. 3-14** shows the RKE-based simulation results are close to both the experimental and LES results for the normalized axial velocity and fluid temperature distributions. Therefore, it is regarded that it is sufficient to use the RKE-based simulation for predicting the flow patterns at T-junctions and Y-junctions.

Table 3-7 Main Simulation Conditions

	Main Pipe	Branch Pipe
Mean Velocity at Inlet [m/s]	1.46	1.0
Fluid Temperature at Inlet [°C]	48	33
Inner Diameter [mm]	150	50
Reynolds Number [-]	$3.8x10^5$	$6.6x10^4$
Momentum Ratio [-]	8.14 (Wall Jet)	

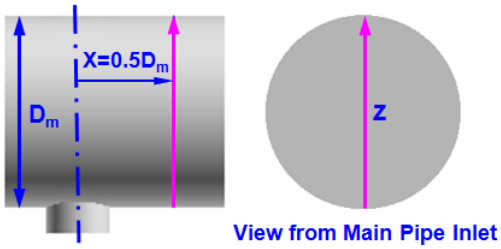

Fig. 3-13 Location and Direction (Arrowed Pink Lines) for the Plots in Fig. 3-14 & Fig. 3-15

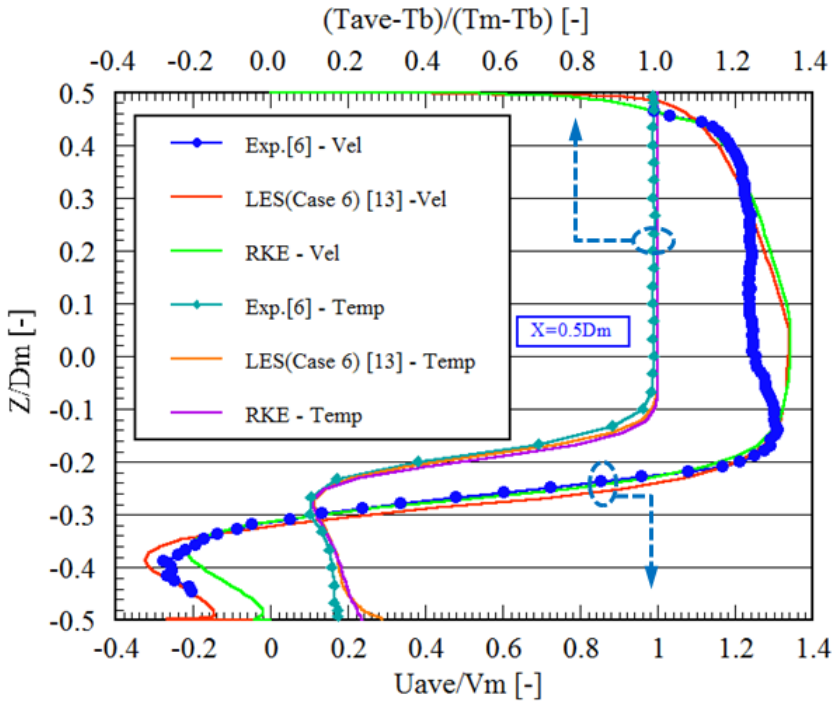

Fig. 3-14 Comparison of Normalized Time-Averaged Axial Velocity and Fluid Temperature Distributions along Vertical Direction at the Location of X=0.5D_m for Validation of CFD Prediction by RKE Turbulence Model

Appendix 3-2 Investigation of Mesh Sensitivity

The meshes used for the investigation of mesh sensitivity were generated referring to the mesh used in **Chapter 4**, where LES-based unsteady CFD validation simulations were carried out using a full model of T-junction with the number of cells being about 1,022,000 (equivalent to about 511,000 for a half model), and the CFD results agreed with the experimental results. A preliminary investigation of mesh sensitivity was made for the half model of T-junction using two meshes with the number of cells being nearly 350,000 (Coarse Mesh) and 700,000 (Fine Mesh) (equivalent to about 700,000 and 1,400,000 for a full model) respectively. CFD simulations with the two meshes were performed using the RKE turbulence model for momentum ratio M_R=3.80. As shown in **Fig. 3-15**, compared are the normalized time-averaged axial velocity and fluid temperature distributions along the vertical direction in the cross-section of 0.5Dm downstream of the center-line of branch pipe (see **Fig. 3-13**). The CFD results for Coarse Mesh agree with those for Fine Mesh very well. Therefore, it is considered that it is adequate to use the relatively coarse

mesh with nearly 350,000 cells for the present investigation.

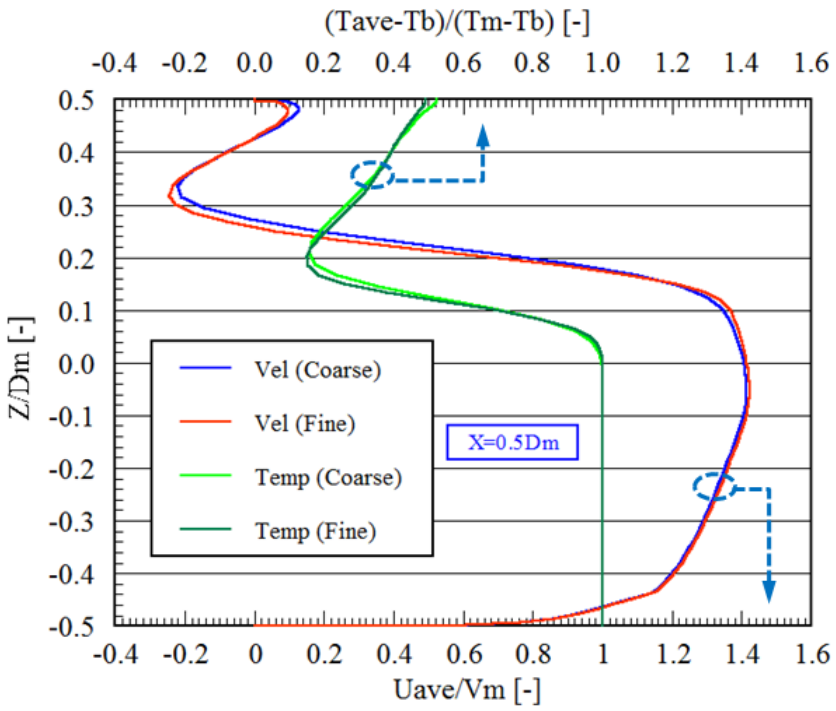

Fig. 3-15 Comparison of Normalized Time-Averaged Axial Velocity and Fluid Temperature Distributions along Vertical Direction at the Location of X=0.5D_m for Mesh Sensitivity Investigation

Appendix 3-3 LES Simulations of 30° Y-junction and 90° T-junction at M_R=0.33 and M_R=0.38

Computational Conditions and Numerical Methods:

The unsteady LES simulations are performed for 30° Y-junction and 90° T-junction at M_R=0.33 and M_R=0.38, to compare their fluid temperature fluctuation intensities around the impinging locations. Different from the steady-state simulations, the full models are used for the unsteady LES simulations. The meshes for 30° Y-junction and 90° T-junction are shown in Fig. 3-16 (a) and Fig. 3-16 (b), respectively. The near-wall cell size for the meshes is $y^+ < 40$, and hence, the wall functions are applied for the wall boundary condition of flow. As shown in **Appendix 5-1** in **Chapter 5**, the fluid temperature fluctuations can also be predicted well even using a combination of LES simulation and the wall functions for a relatively coarse near-wall

mesh. The number of cells of the mesh is nearly 920,000 for the models of both 30° Y-junction and 90° T-junction.

The computational conditions used are the same as those for the steady-state simulations described above. The LES SGS turbulence model applied is dynamic Smagorinsky model (DSM). The differencing scheme applied for calculating the convective terms is a hybrid scheme (HS) with a blending factor being 0.9 for the momentum equations and 0.8 for the energy equation. Procedures for the LES analyses and the convergence criteria for the iterative solution are the same as those shown in Section 4-4-3 in Chapter 4. The sampling time for the statistical calculation is 41.0 seconds with a time-step interval of Δt=0.005 sec.

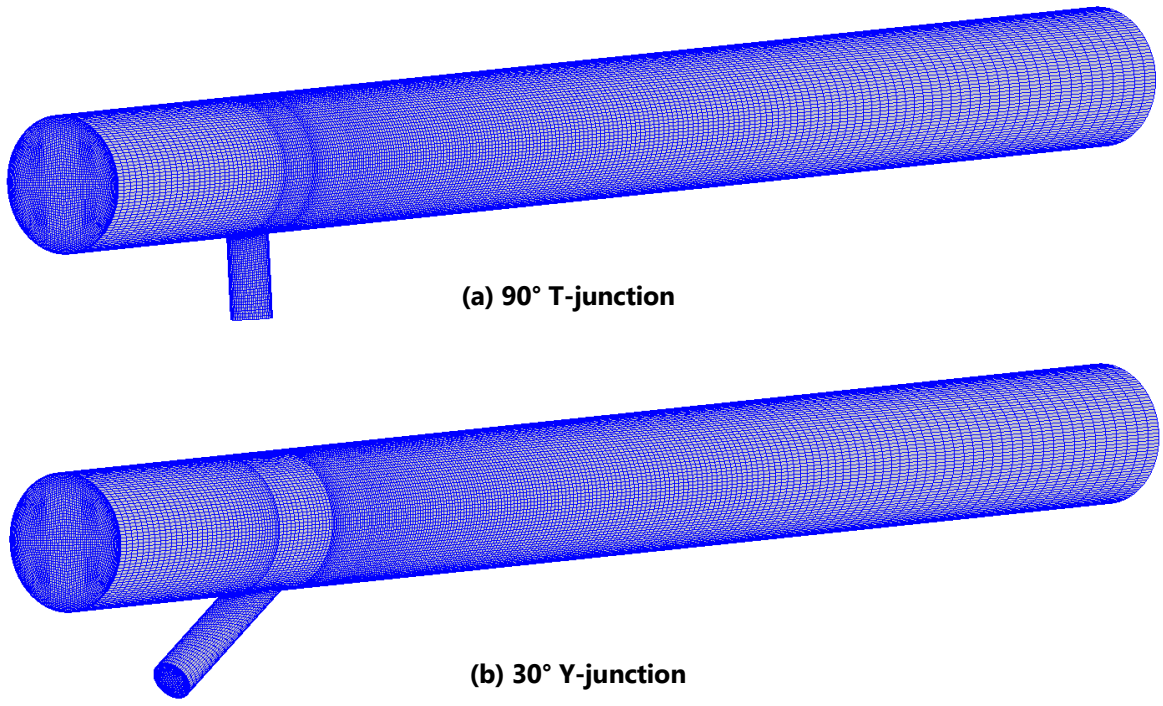

Fig. 3-16 Meshes for the Models of 90° T-junction and 30° Y-junction

LES Simulation Results:

Here, the LES simulation results only for M_R=0.33 are described in detail, as it is considered that the results for M_R=0.33 and M_R=0.38 are similar. For M_R=0.38, only the temperature fluctuation intensity distributions, which are important for flow pattern classification, are shown.

Fig. 3-17 show the LES results for the instantaneous flow velocity vectors and temperature distribution on the vertical cross-section along the flow direction at 41 sec after sampling start, for 90° T-junction and 30° Y-junction at M_R=0.33. The LES results indicate that the branch jet impinges against the opposite wall of main pipe at the locations around $0.5D_m$~$1.0D_m$ downstream of junction for 90° T-junction and around $1.5D_m$~$2.0D_m$ downstream for 30° Y-junction. This is the typical flow pattern of an impinging jet. In the mixing zone, the flow is very unstable and strongly fluctuating due to the interaction between the branch jet and the crossflow from the main pipe, and consequently, the temperature field also strongly fluctuates.

For M_R=0.33, the simulation results for the temperature fluctuation intensity distributions on the vertical cross-sections along and perpendicular to the flow direction are shown in **Fig. 3-18** and **Fig. 3-19**, respectively. At the same time, the temperature fluctuation intensity distributions on the cylindrical surface 1mm away from the wall of main pipe are shown in **Fig. 3-20**. Here, for M_R=0.38, just the temperature fluctuation intensity distributions on the cylindrical surface 1mm away from the wall of main pipe are shown in **Fig. 3-21**. It can be found that for both M_R=0.33 and M_R=0.38, the near-wall fluid temperature fluctuation intensities around the impinging location for 90° T-junction is obviously higher than those for 30° Y-junction.

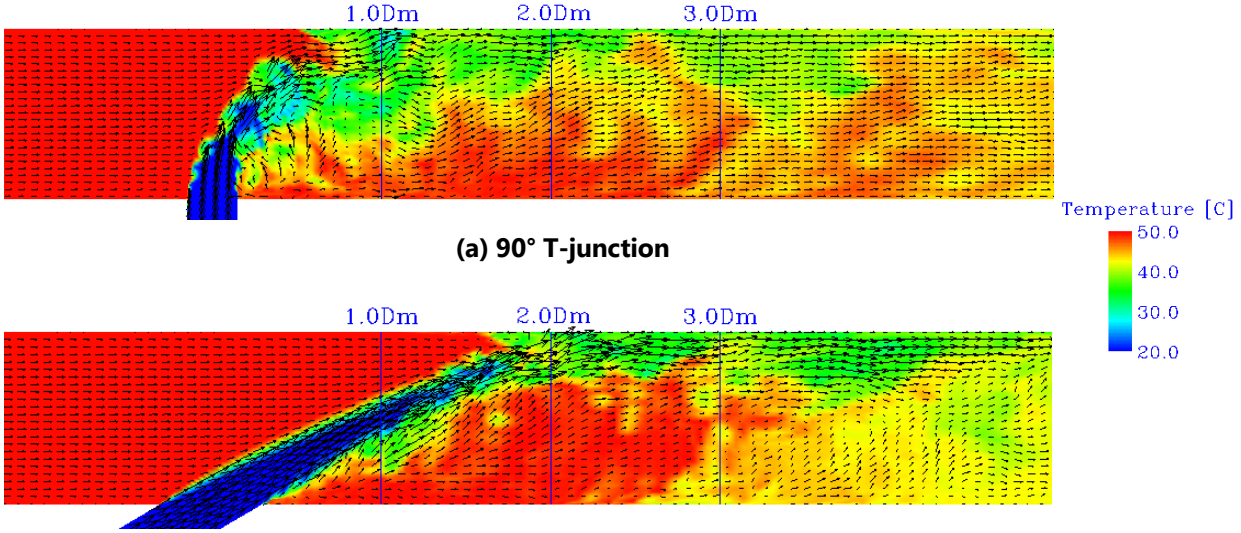

(a) 90° T-junction

(b) 30° Y-junction

Fig. 3-17 Instantaneous Flow Velocity Vectors and Temperature Distribution on Vertical Cross-section along Flow Direction in the Mixing Zone at t=41.0 sec for M_R=0.33

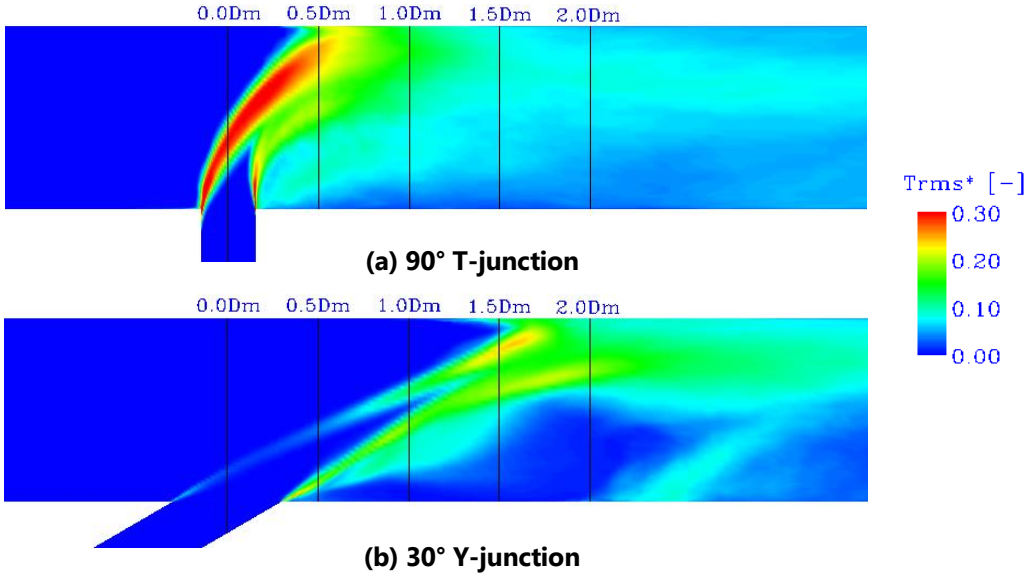

(a) 90° T-junction

(b) 30° Y-junction

Fig. 3-18 Distribution of Normalized Temperature Fluctuation Intensity on the Cross-section along the Flow Direction in the Mixing Zone for M_R=0.33

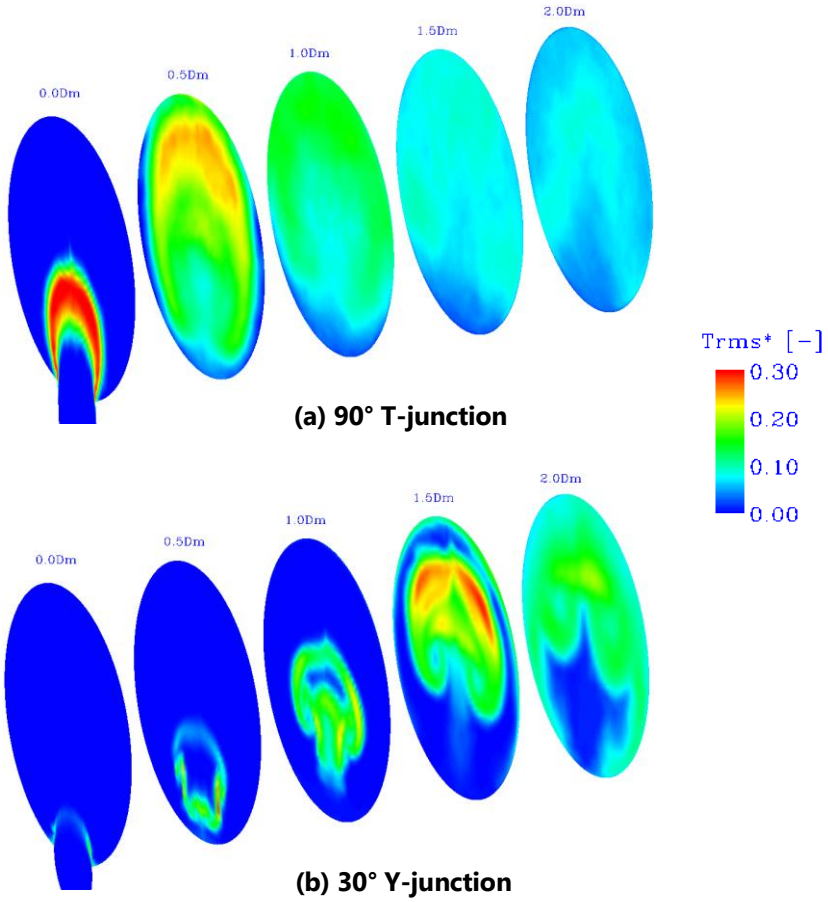

(a) 90° T-junction

(b) 30° Y-junction

Fig. 3-19 Distribution of Normalized Temperature Fluctuation Intensity on the Cross-sections Perpendicular to the Flow Direction in the Mixing Zone for M_R=0.33

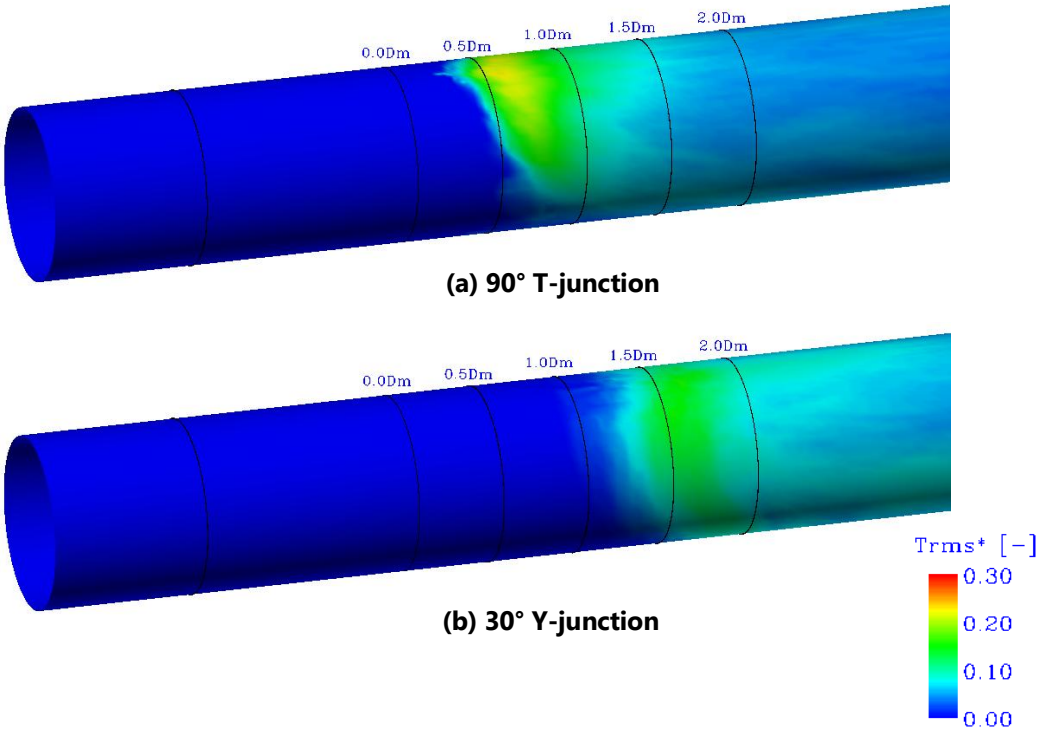

Fig. 3-20 Distribution of Normalized Temperature Fluctuation Intensity on the Cylindrical Surface 1mm away from the Main Pipe Wall in the Mixing Zone for M_R=0.33

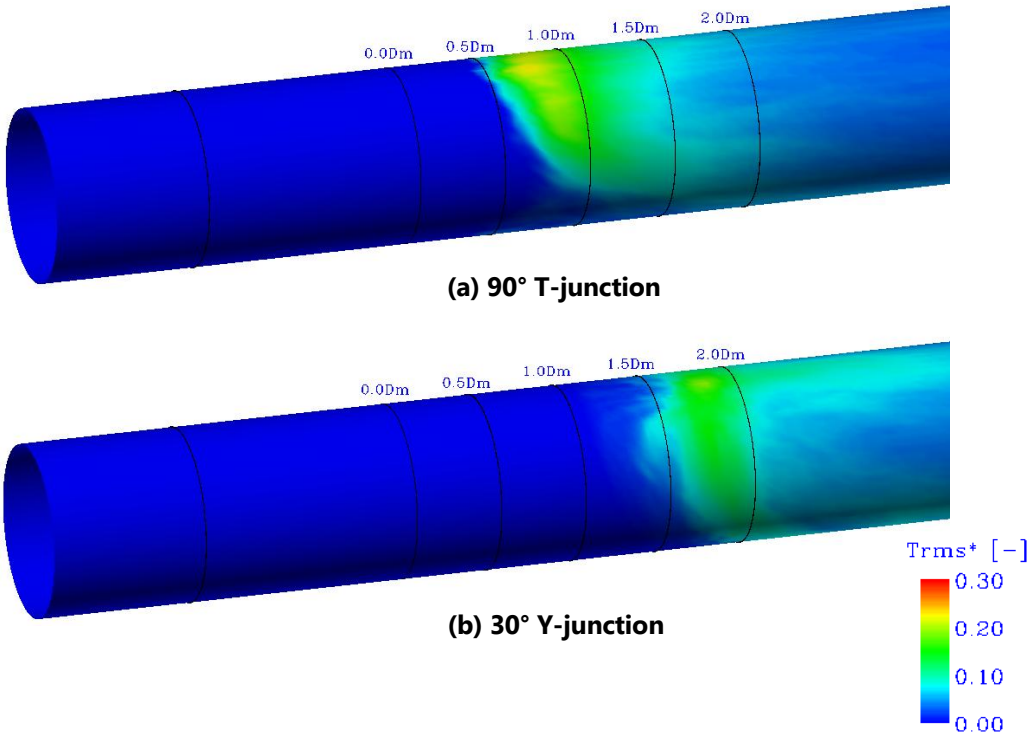

Fig. 3-21 Distribution of Normalized Temperature Fluctuation Intensity on the Cylindrical Surface 1mm away from the Main Pipe Wall in the Mixing Zone for M_R=0.38

Chapter 4 High-Accuracy CFD Prediction Methods of Fluid Temperature Fluctuations

4-1 Introduction

As a conventional guideline for thermal fatigue evaluation, JSME S017 provides the procedures and methods of evaluating the integrity of structures with potential high cycle thermal fatigue (HCTF). However, the accuracy of the evaluation results is not high and especially the evaluation margin varies greatly from one case to another case [120], as JSME S017 was developed based on limited experimental data and simplified one-dimensional (1D) FEA. In addition, for JSME S017, the fatigue evaluation method in Step 4 was established based on the experimental data and thus, its application is limited to the range where the experimental data were obtained. Also, the dependence of thermal stress attenuation on the fluctuation frequency of fluid temperature was not considered in Step 4. Therefore, it is desirable to establish a more accurate method of HCTF evaluation with a slight conservativeness.

CFD/FEA coupling analysis is expected to be a useful and effective tool for more accurately evaluating HCTF. It is very important to predict accurately the fluctuation amplitudes and cycle numbers (or frequencies) of thermal stress induced by the fluid and structure temperature fluctuations (STF) using FEA in order to perform fatigue damage evaluation. The fluid temperature fluctuations induced by incomplete mixing of hot and cold fluids at a T-junction are the root cause of thermal fatigue. Hence, it is first important to predict accurately the fluid temperature fluctuations by CFD simulations.

Many researchers have investigated the flow and temperature fields at T-junctions by the experiments and numerical simulations for evaluation of thermal fatigue loading. For example, Hu et al. [109] undertook the simulation of flow and temperature at T-junctions based on the RNG LES model using the commercial CFD code, FLUENT. The simulation results for the temperature fluctuations have significant difference from the experimental ones, although the calculated results for the time-averaged temperature agree well with the experimental ones.

Tanaka et al. [81] also performed the simulations of flow and temperature at T-junctions using the VLES approach, in which an LES model is combined with the wall function for the coarse mesh. The results suggested the possibility of reproducing the temperature fluctuations using the LES model. Kamide et al. [83] carried out the investigation into the temperature fluctuations of water by making a series of tests using the WATLON apparatus. They also performed the numerical simulations under the same conditions as the WATLON tests using their in-house AQUA code, and the results for velocity and temperature distribution exhibited good agreement with the experimental ones. However, a specific guideline showing what kinds of CFD numerical methods can provide high-accuracy prediction of thermal loadings has not yet been established.

The present investigation aims to establish high-accuracy methods of predicting fluid temperature fluctuations (or thermal loading) by systematic CFD benchmark simulations. The benchmark simulation conditions are the same as in the WATLON experiments [83] for comparison. It is very important to choose proper turbulence model and numerical schemes for the CFD simulation of unsteady phenomena, such as the highly fluctuating flow and temperature fields at a T-junction. LES turbulence models suitable for the simulation of unsteady phenomena were systematically investigated. LES sub-grid scale (SGS) turbulence models used included the standard Smagorinsky model (SSM) and the dynamic Smagorinsky model (DSM). Also, the effects of numerical schemes for calculating the convective term in the energy equation on the simulation results were thoroughly investigated. The CFD simulation results were compared with the experimental ones to verify the accuracy of the investigated numerical models.

4-2 The Choice of Numerical Methods

The temperature fluctuation of fluid is the root cause of thermal fatigue, and hence, its accurate prediction is very important for the precise evaluation of thermal fatigue. As described in **Chapter 2**, CFD approaches mainly include three types of direct numerical simulation (DNS), Reynolds-averaged Navier-Stokes (RANS) equations-based method and large eddy simulation

(LES). **Table 4-1** shows the features of major CFD simulation approaches. DNS directly solves the Navier-Stokes equations without the use of any turbulence model and, hence, needs a very fine mesh. As a result, it can achieve very accurate numerical solutions. However, a high cost and a long computational time are required. Thus, its application in engineering would not be practical. RANS solves time-averaged Navier-Stokes equations using a turbulence model (typically $k-\varepsilon$ model) and a coarse mesh. It has a low cost and a short computational time, but it is mainly suited for solving time-averaged flow and scalar fields. Hence, RANS was not suitable for the purpose of predicting accurate temperature fluctuation histories. However, LES solves space-averaged Navier-Stokes equations using a SGS turbulence model and a moderately fine mesh. It is expected that LES is able to achieve reasonably accurate numerical solutions in solving the unsteady flow and scalar fields if a proper SGS turbulence model is chosen. Moreover, the cost and computational time needed are moderate. Therefore, LES was chosen for simulating the temperature fluctuations of fluid in the present investigation.

For predicting the fluid temperature fluctuations accurately, two key points are as follows:

- Choose a proper LES SGS turbulence model capable of evaluating the actually existing turbulent diffusion accurately
- Choose a highly accurate finite difference scheme for calculating the convective terms in the governing equations which is able to reduce the numerical diffusion as much as possible while maintaining the numerical stability

This is because over-predicted turbulent diffusion, which easily occurs with some of the commonly-used turbulence models, and large numerical diffusion can significantly damp the amplitude of fluid temperature fluctuations. The main numerical methods chosen for investigations are shown in **Table 4-2**. The investigated LES SGS turbulence models include the standard Smagorinsky model (SSM) and the dynamic Smagorinsky model (DSM). The detailed features of SSM and DSM were described in **Chapter 2**. One of the most important features is that the model parameter is treated as a constant in the SSM model, while it is evaluated as a function of the local flow field in the DSM model. Therefore, it is regarded that the DSM model

can more accurately predict the turbulent eddy viscosity (or turbulent diffusion coefficient) than the SSM model.

Table 4-1 Features of Main CFD Approaches

Approach	Mesh	Accuracy	Cost	Computing Time	Suitability for Simulation of Fluid Temperature Fluctuations
DNS	Very fine	Very high	High	Long	Not practical (high cost and long time)
RANS	Coarse	Low	Low	Short	Not suitable (low accuracy)
LES	Moderately fine	High	Moderate	Moderate	Suitable (high accuracy, moderate cost and computational time)

Table 4-2 Adopted Numerical Methods

CFD Code		Modified FrontFlow/Red
Simulation Mode		Unsteady-state simulation
Turbulence Model		● LES standard Smagorinsky SGS model (**SSM**) ● LES dynamic Smagorinsky SGS model (**DSM**)
Numerical Scheme for Calculation of Convective Term	Momentum Equations	● Hybrid scheme (**HS**): α_{bf} *2CD+(1.0−α_{bf})*1UD where α_{bf} : Blending factor (α_{bf} =0~1.0) **2CD**: 2nd-order central difference scheme **1UD**: 1st-order upwind difference scheme
	Energy Equation	● 1st-order upwind difference scheme ● Hybrid scheme ● TVD 2nd-order upwind difference scheme
Time Integration		Implicit Eulerian time integration (1st-order accurate)

Also, the investigated difference schemes for calculating the convective terms of energy equation include the 1st-order upwind difference (1UD) scheme and a hybrid scheme (HS), which blends the 1UD scheme and 2nd-order central difference (2CD) scheme, and TVD 2nd-order upwind difference scheme. The details for various difference schemes are described in

Section 2-4 in **Chapter 2.** Hence, only the main features of them are briefly introduced here. The 1UD scheme has relatively strong numerical diffusion and, thus, can attenuate the fluid temperature fluctuation, although it has a good numerical stability. In contrast with this, the 2CD scheme has no numerical diffusion effect and, hence, has a high numerical accuracy, but numerical instability easily occurs. Therefore, the pure 2CD scheme is not applicable for the calculation of the convective terms. The hybrid scheme blends the 1UD scheme and 2CD scheme to combine their respective advantages (see **Table 4-2**). Therefore, the hybrid scheme should, simultaneously, be able to achieve high numerical accuracy and maintain numerical stability, if a sufficiently large blending factor is chosen.

In addition, similar to the 2CD scheme, the ordinary 2nd-order accurate upwind scheme (2UD) also has no numerical diffusion effect, as its truncation error of the 2UD scheme also contains the 3rd-order derivative. As a result, numerical instability also easily occurs when applying the 2UD scheme for a relatively coarse mesh. On the other hand, the TVD 2nd-order upwind difference scheme (hereafter, called the TVD scheme) blends the 2UD scheme with the 1UD scheme and hence can maintain the numerical stability. The slope limiter equivalent to the blending factor in the hybrid scheme is automatically calculated as a function of the local flow field and thus there is no need to give its value beforehand.

In the present research, the effects of LES turbulence models and the difference schemes on CFD simulation results are clarified by comparing the numerical simulation results with the experimental ones, in order to establish a highly accurate LES turbulence model and difference schemes that will be suitable for prediction of fluid temperature fluctuations.

4-3 Experimental Conditions for Benchmark Simulations

As described above, the present investigation aims to establish high-accuracy methods of predicting fluid temperature fluctuations (or thermal loading) by performing CFD benchmark simulations. Here, the adopted benchmark simulation conditions were the same as in the WATLON experiments conducted by Igarashi et al. [83] at JAEA, as described in Section 1-3-3

in **Chapter 1**. The test section was made of transparent acrylic resin and comprised a horizontal main pipe and a vertical branch pipe with the inner diameters being 150mm and 50mm, respectively, as shown in **Fig. 1-7**. The time series data for fluid temperature distribution in the main pipe were measured using a thermocouple tree with 17 thermocouples. The time series data for flow velocity distribution at the T-junction were also measured using a PIV system. By statistically treating the measured time series data, Igarashi et al. obtained the time-averaged fluid temperature and flow velocity distributions, and their fluctuation intensity distributions, which are used for comparison with the CFD benchmark results.

In the WATLON experiment, a series of tests were carried out under various conditions. In the present investigation, the conditions for the flow pattern of wall jet shown in **Table 4-3** were chosen for the numerical simulations, considering that the experimental conditions and results for this case have previously been reported in detail [83]. The flow pattern at a T-junction can be classified by the following criteria (or the Criteria 3 in **Chapter 3**), based on the interacting momentum ratio (M_R) between the main pipe and branch pipe streams.

Wall Jet $4.0 < M_R$

Deflecting Jet $0.35 < M_R < 4.0$

Impinging Jet $M_R < 0.35$

where the momentum ratio M_R is defined as follows [19]:

$$M_m = D_m D_b \rho_m V_m^2 \tag{4-1}$$

$$M_b = \pi D_b^2 \rho_b V_b^2 / 4 \tag{4-2}$$

$$M_R = M_m / M_b \tag{4-3}$$

The fluid used was water. The temperatures of the water at the inlets of the main pipe and the branch pipe were $T_m = 48^\circ C$ and $T_b = 33^\circ C$, respectively. The dependence of the physical properties of the fluid on temperature was negligible, as the range of temperature variation was narrow ($15^\circ C$) in the present simulations. Specifically, the variation of the fluid density was less than 0.5% between $33^\circ C$ and $48^\circ C$. As shown in **Table 4-4**, the physical properties of water at the temperature of $(T_m+T_b)/2$ were used in the simulations.

Table 4-3 Conditions for CFD Benchmark Simulations

	Main Pipe	Branch Pipe
Mean Velocity at Inlet [m/s]	1.46	1.0
Fluid Temperature at Inlet [$^{\circ}C$]	48	33
Inner Diameter [mm]	150	50
Reynolds Number [-]	3.8×10^5	6.6×10^4
Momentum Ratio (M_R) [-]	8.14 (Wall Jet)	

Table 4-4 Physical Properties of Water

Density [kg/m^3]	991.7
Viscosity [Pa.sec]	0.0006652
Specific Heat [J/kg/K]	4179.7
Thermal Conductivity [W/m/K]	0.6285

4-4 Computational Model and Boundary Conditions and CFD Analysis Methods

4-4-1 Computational Model

The computational model and main boundary conditions for the T-junction are shown in **Fig.4-1**. The lengths of the inlet section were set as $2D_m$ (D_m=150mm) for the main pipe and $2D_b$ (D_b =50mm) for the branch pipe, and the length of the outlet section was set as $5D_m$ to reduce the number of cells in the mesh for reducing the computational time. These settings were

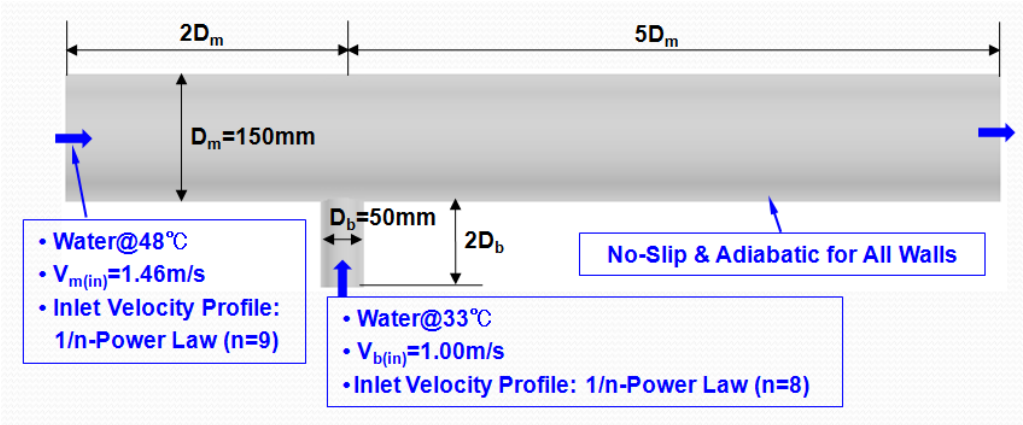

Fig. 4-1 Geometry of Computational Model and Boundary Conditions

reasonable because the reducer nozzles and fully long straight pipes were installed in the upstream of the main pipe and branch pipe for straightening the flow into the T-junction in the experimental apparatus [83] and the fully developed turbulent flow profiles were applied for the main pipe and branch pipe inlets in the present investigations (see below for details). The present investigation was intended to simulate the flow and temperature fluctuations of the fluid only, and hence the pipe thickness was not included in the simulations.

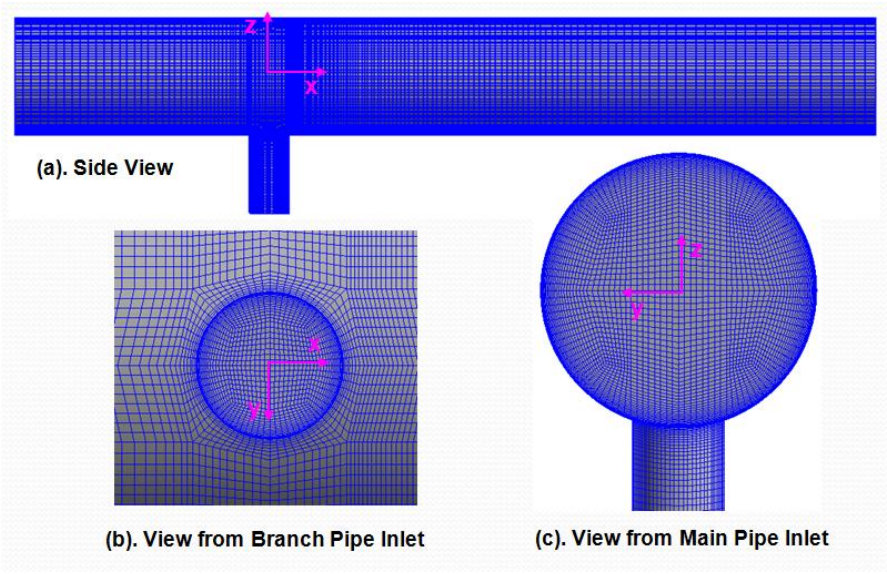

Fig. 4-2 Meshes for Computational Model

The present investigation aims at simulating the unsteady flow and temperature fields at the T-junction using the LES SGS turbulence model. A comparatively fine mesh, especially near the wall, is desirable for LES simulation. A rather fine mesh in proximity of the wall was generated, and the near-wall cell size was uniformly 0.0563mm and could keep $y_F^+ < 5.5$ for ensuring that all the near-wall grid points are located within the viscous sub-layer of flow boundary. However, the mesh in the central part of the pipe was relatively coarse to reduce the computing time as much as possible. The meshes used for the simulations are shown in **Fig.4-2**. The number of cells in the mesh was about 1,022,000. To investigate the effect of grid sizes on the CFD results, the LES simulations were beforehand performed using 3 different meshes with the number of cells being about 1,532,000, 1,022,000 and 680,000. The investigation shows that difference between the CFD results for three different meshes is very small, and all the CFD results are close to the

experimental ones (see **Appendix 4-1** for the details). Hence, it is considered that the spatial resolution of the mesh with about 1,022,000 cells is adequate for the present investigation.

4-4-2 Boundary Conditions

As shown in **Fig.4-1**, all the walls were set as adiabatic for the thermal boundary condition, as the pipe was made of acrylic resin with a low thermal conductivity and moreover its outside was thermally insulated. For the flow boundary condition, no slip was applied for all the walls, as all the near-wall cells ($y_F^+ < 5.5$) were located within the viscous sub-layer.

The mean flow velocities and water temperatures at inlets of the main and branch pipes are shown in **Table 4-3** and **Fig.4-1**. In view of the fact that the lengths of the inlet and outlet sections were relatively short, some measures were taken when setting the inlet and outlet conditions. For a fully developed turbulent flow, a 1/n-power law [137] was applied for the inlet velocity profile to reduce the effects of the short inlet section as far as possible. The 1/n-power law can be written as follows:

$$u / u_{\max} = (y / R)^{1/n} \tag{4-4}$$

$$n = 3.45\,\mathrm{Re}^{0.07} \tag{4-5}$$

where u is the time-averaged velocity at a distance of y to the pipe wall, u_{max} the velocity at the center of pipe inlet, R the inner radius of the pipe and Re the Reynolds number based on the averaged velocity. The values, n_m=9 and n_b=8, can be obtained by substituting the Reynolds numbers shown in **Table 4-3** into Eq.(4-5) and rounding off to the nearest whole number. However, the turbulence intensity at the inlet was not considered in the present simulations because the temperature fluctuations downstream of junction were dominantly caused by the intense mixing of the cold and hot fluids coming from the main and branch pipes. In fact, Nakamura et al. [139] also performed the LES analyses of the same T-junction for two cases with and without consideration of the turbulence intensity at the inlet respectively. The LES results showed that the difference of the results between two cases was relatively small and thus negligible.

In addition, a free outflow condition was applied at the outlet. Specifically, the condition of zero-gradient along the direction normal to the outlet for each quantity (including velocity components, pressure and temperature) is applied.

4-4-3 CFD Analysis Methods

Procedures for the LES analyses of flow and temperature fields mostly included the following 3 steps for each case:

(1) As the initial conditions of unsteady LES analysis, the flow and temperature fields were first calculated for 4.0 seconds using the realizable $k-\varepsilon$ turbulence model with a large time-step interval of Δt=0.001 sec.

(2) LES simulation was carried out for 1.5 seconds (over twice the mean residence time of flow) using a small time-step interval of Δt=0.0002 sec to develop the flow and temperature fields to the quasi-periodic state.

(3) LES simulation was run for 5.5 seconds to carry out the statistical calculation of unsteady flow and temperature fields, using a small time-step interval of Δt=0.0002 sec. The sampling time interval was 0.001sec, or the sampling was done once every 5 time steps.

The main numerical methods used are shown in **Table 4-2**. LES sub-grid scale (SGS) models and numerical schemes have been described in Section 2 and hence are not repeated here. The 1st-order accurate implicit Eulerian time integration scheme was applied for time advancement. A small time-step interval (Δt=0.0002 sec) was used for the LES analyses to keep the maximal Courant number below 1.0. Based on the finding of Igarashi et al. [74], it was predicted in advance that the order of temperature fluctuation frequency of our interest was around 6.0Hz (below 10.0Hz), or the corresponding time scale being above 0.1sec. Obviously, the time step interval used is sufficiently small relative to the time scale and thus has a sufficient time resolution for the temperature fluctuations of our interest even using the 1st-order Eulerian scheme. Also, the effect of time step interval on the CFD simulation results was investigated by conducting the LES analyses using three different time step intervals of Δt=0.0001 sec,

Δt=0.0002 sec and Δt=0.0004 sec. The LES analysis results for the three different time step intervals are very close, and also near the experimental measurements (see **Appendix 4-1** for the details of investigation results). Hence, it is considered that the chosen time step intervals of Δt=0.0002 sec is sufficiently accurate for the present research.

In every time step, the iterative solution was performed for any quantity ϕ. The root-mean-square (RMS) normalized residual used for the convergence judgment is defined as follows:

$$\varepsilon_{\phi}^{*} = \sqrt{\sum_{i=1}^{N}[(\phi_i^n - \phi_i^{n-1})/\phi_i^n]^2 \Big/ N} \tag{4-6}$$

where N is the total number of cells to be solved, n and $n-1$ represent the current and last iterations, respectively. The convergence criteria were set as 1.0×10^{-5} for each velocity component and temperature, and 1.0×10^{-7} for pressure, respectively.

4-5 LES Simulation Results and Discussions

The scenario of LES benchmark analyses was proposed and shown in **Table 4-5**, based on the fact that the potentially over-evaluated turbulent eddy viscosity by LES SGS turbulence models and numerical diffusion of differencing schemes may remarkably attenuate the predicted fluid temperature fluctuations (FTF). The LES SGS turbulence models chosen were the standard Smagorinsky model (SSM) and the dynamic Smagorinsky model (DSM). The effects of the model parameter on the results were also investigated for the SSM model. Moreover, the effects of the numerical schemes for the convective term in the energy equation were investigated as well, as the numerical schemes for the convective term have a more significant effect on numerical stability of the energy equation than the momentum equations have. LES benchmark analyses of flow and temperature fields at a T-junction were carried out using the modified multi-physics CFD software FrontFlow/Red [138] (see **Appendix A** for its details).

In the following, the simulation results for the flow and temperature fields at the T-junction are presented in comparison with the experimental results. However, the focus was mainly

concentrated on the results of the temperature fields, which are needed for the evaluation of thermal loading. It should be noted that the LES results presented below are those obtained during the period of sampling LES simulation in Step 3 in Section 4-3-3.

Table 4-5 Scenario Proposed for LES Benchmark Analyses

Case No.	LES SGS Turbulence Model	Numerical Scheme for Convective Terms		Sampling Period [sec]
		Momentum Equations	Energy Equation	
Case 1	SSM(Cs=0.1)	HS(α_{bf}=0.9)	1UD	5.5
Case 2	SSM(Cs=0.14)	HS (α_{bf}=0.9)	1UD	5.5
Case 3	SSM(Cs=0.14)	HS (α_{bf}=0.9)	HS (α_{bf}=0.6)	5.5
Case 4	DSM	HS (α_{bf}=0.9)	1UD	5.5
Case 5	DSM	HS (α_{bf}=0.9)	HS (α_{bf}=0.6)	5.5
Case 6	DSM	HS (α_{bf}=0.9)	HS (α_{bf}=0.8)	5.5
Case 7	DSM	HS (α_{bf}=0.9)	TVD	5.5

4-5-1 Flow Velocity Distribution

In **Fig.4-3**, the calculated results for the distribution of the normalized time-averaged axial velocity are compared with the experimental ones obtained in the WATLON test [83]. For clarity, the locations and direction of lines on the plot are indicated with arrowed pink lines in **Fig.4-4. Fig.4-3(a)** and **Fig.4-3(b)** show the distributions of time-averaged axial velocity along the radial direction at x=0.5D_m and 1.0D_m, respectively. The profiles for calculated axial velocity mostly agree well with the experimental ones for each case, although there is a small discrepancy in the central part of the main pipe that is probably attributed to the relatively coarse grid in this part. The distribution of the calculated axial velocity in the DSM model is closer to the experimental one than in the SSM model. In addition, **Fig.4-3(a)** shows that, due to shedding of the complicated vortices in the wake of bent branch jet, there occurs a much turbulent flow near the lower pipe wall at x=0.5D_m, where is near the wake of branch jet. In contrast, as shown in **Fig.4-3(b)**, the effect of vortex shedding in the wake of branch jet decreases and hence, the turbulence of flow becomes relatively weak near the lower pipe wall at x=1.0D_m, where is a little far away from the wake of branch jet.

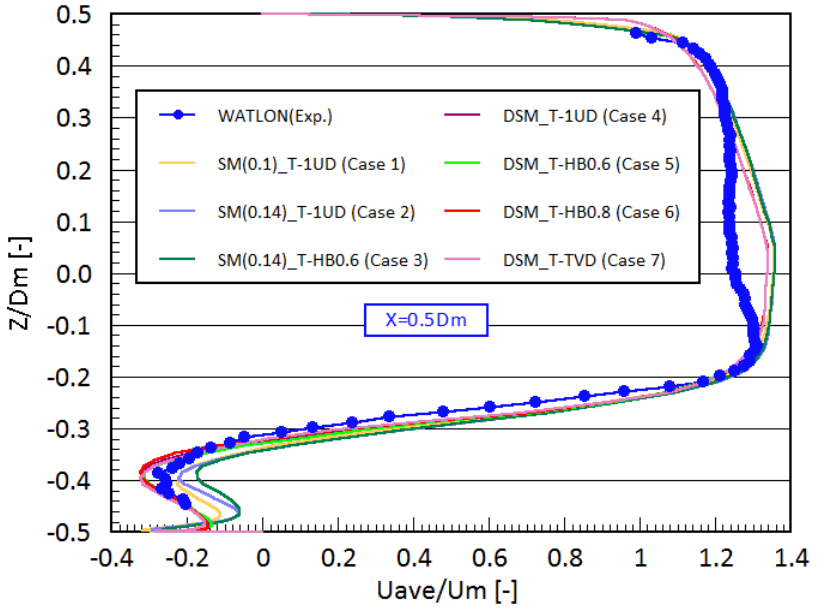

(a) X=0.5D_m

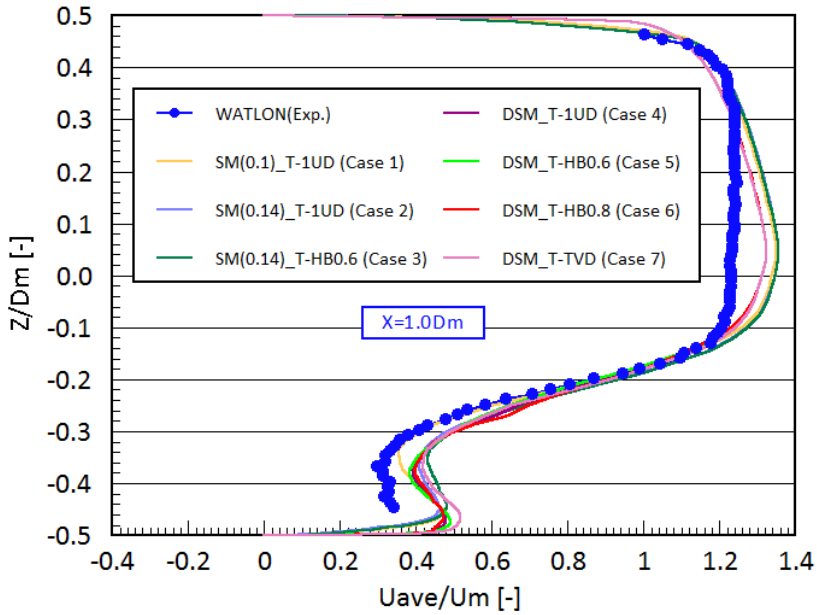

(b) X=1.0D_m

Fig. 4-3 Distribution of Normalized Time-Averaged Axial Velocity along Radial Direction

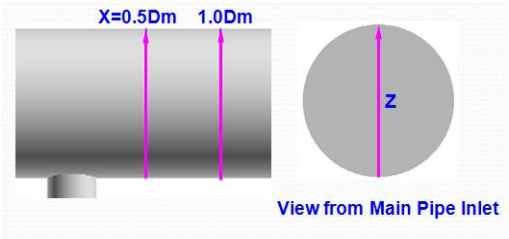

Fig. 4-4 Locations and Direction of the Lines (Pink) on the Plot in Fig. 4-3 and Fig. 4-7

4-5-2 Fluid Temperature and Its Fluctuation Intensity Distributions

The simulation results for the instantaneous fluid temperature and temperature fluctuation intensity distributions on the vertical cross-section along the flow direction are shown in **Fig.4-5** and **Fig.4-6**, respectively. The temperature fluctuation intensity is defined as the normalized standard deviation of temperature with respect to time, as follows:

$$T_{rms}^{*} = \frac{1}{T_m - T_b}\sqrt{\sum_{i=1}^{N_T}(T_i - T_{ave})^2 \Big/ N_T} \qquad (4\text{-}7)$$

where T_m and T_b are the temperatures at the main pipe and branch pipe inlets, respectively; T_i and T_{ave} the instantaneous temperature and time-averaged temperature, respectively, at the center of any mesh cell; and N_T is the number of sampling time-steps.

From the instantaneous fluid temperature contours in **Fig.4-5(a)~(g)**, it was found that the cold stream coming from the branch pipe was bent near the main pipe wall on the side of the branch pipe due to a comparatively fast main pipe jet. Such a flow pattern is characteristic of a wall jet. The strong interaction of flows from the main pipe and branch pipe produces a wavy interface between the hot and cold streams. The intensively wavy interface is closely related to the formation of complex vortex structures in its proximity.

From the fluid temperature fluctuation intensity contours in **Fig.4-6 (a)~(g)**, it was observed that an intensive temperature fluctuation took place at the interface between the hot and cold streams. In both SSM and DSM models, the temperature fluctuation intensity was lower for the cases (**Fig.4-6 (a), (b), (d)**), where the 1st-order upwind difference (1UD) scheme was used for the convective term in the energy equation, than for the cases(**Fig.4-6 (c), (e), (f), (g)**) where the hybrid scheme (HS) or TVD scheme was used. This was attributed to the fact that the 1UD scheme has a much stronger numerical diffusion than the hybrid scheme and TVD scheme, and hence, remarkably damps the temperature fluctuation. This trend can also be observed from the instantaneous fluid temperature distribution in **Fig.4-5.** The interface between the hot and cold streams in **Fig.4-5 (c), (e), (f), (g)** is more intensively fluctuating than in **Fig.4-5 (a), (b), (d)**.

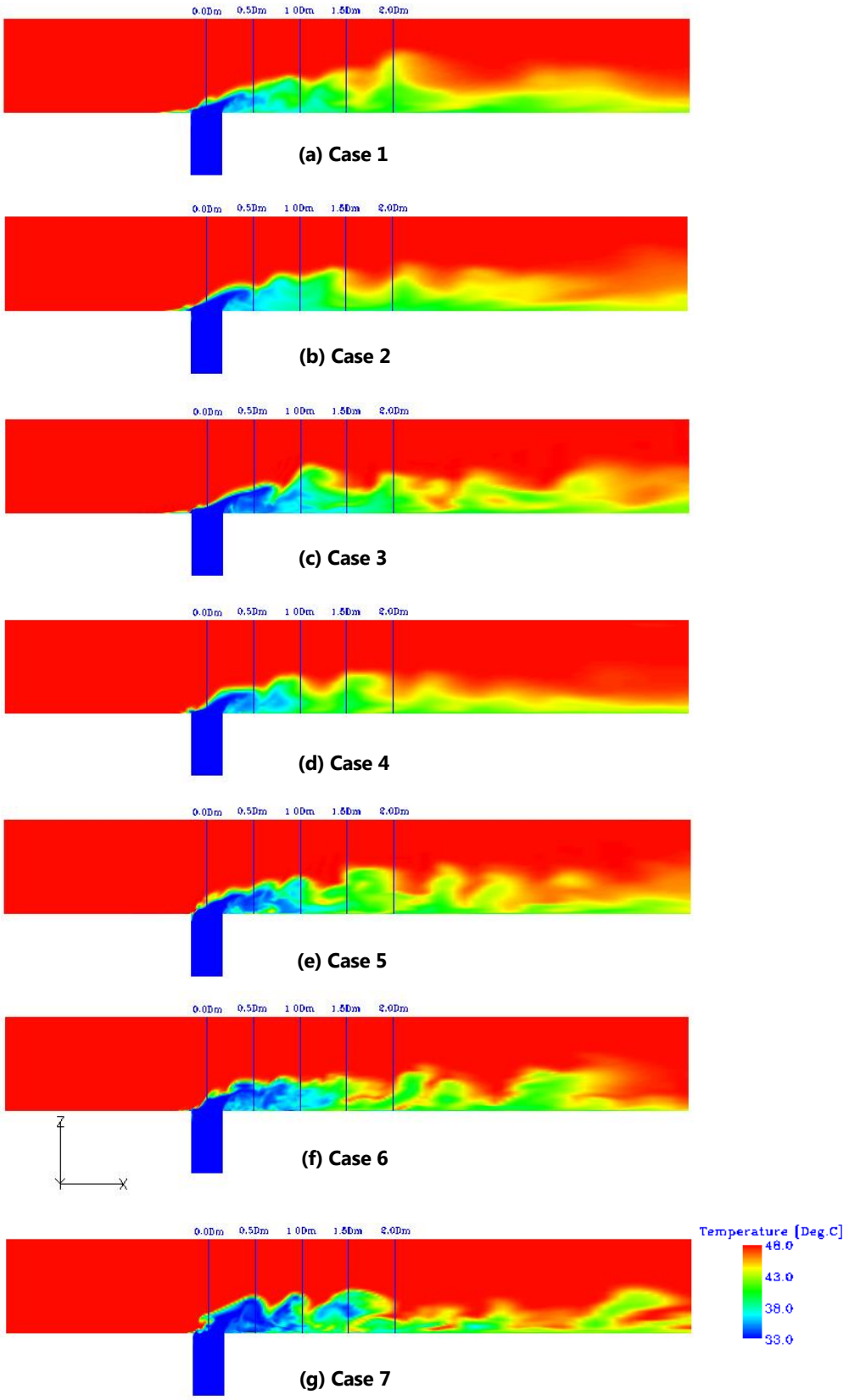

Fig. 4-5 Distribution of Instantaneous Fluid Temperature on the Vertical Cross-section along the Flow Direction at t=11.0sec

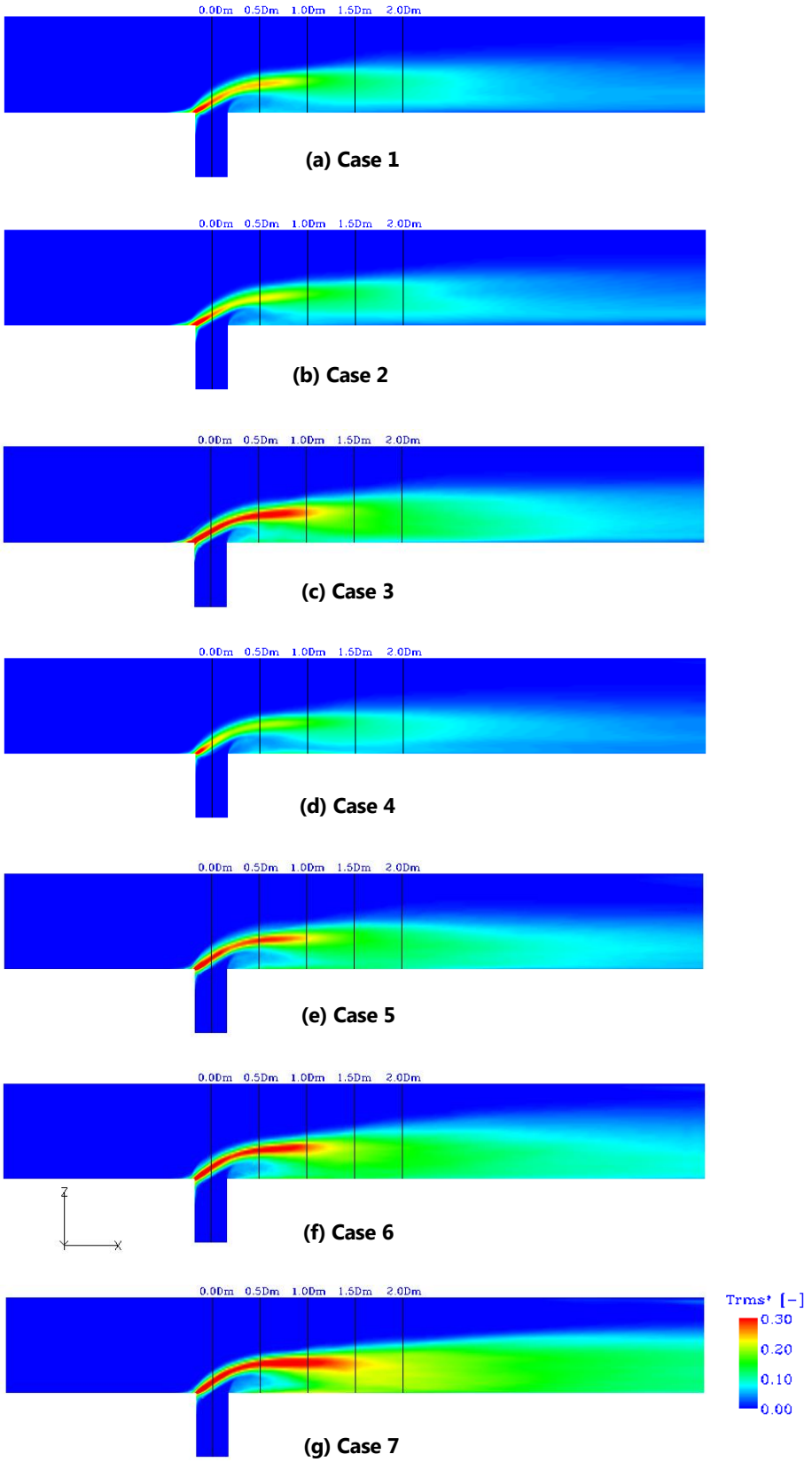

Fig. 4-6 Distribution of Fluid Temperature Fluctuation Intensity on the Vertical Cross-section along Flow Direction at t=11.0sec

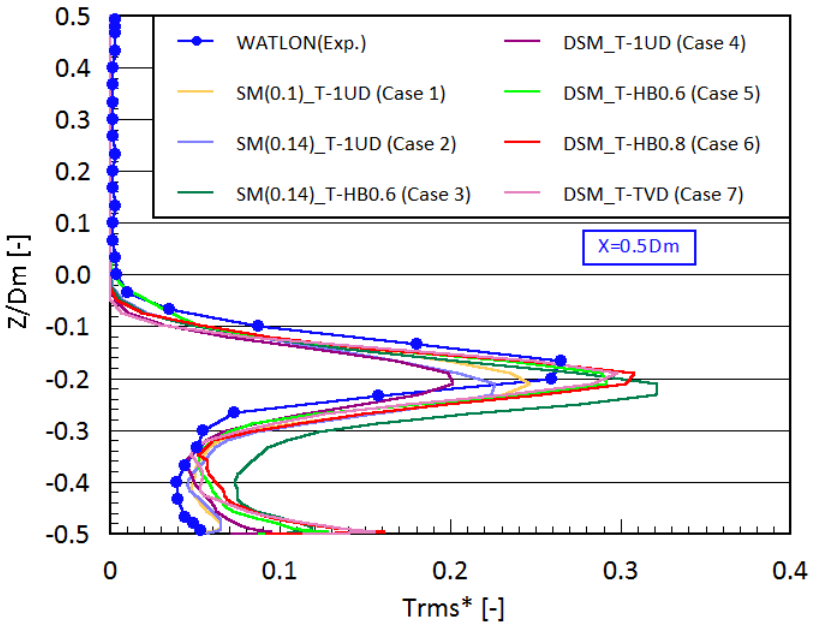

(a) X=0.5D_m

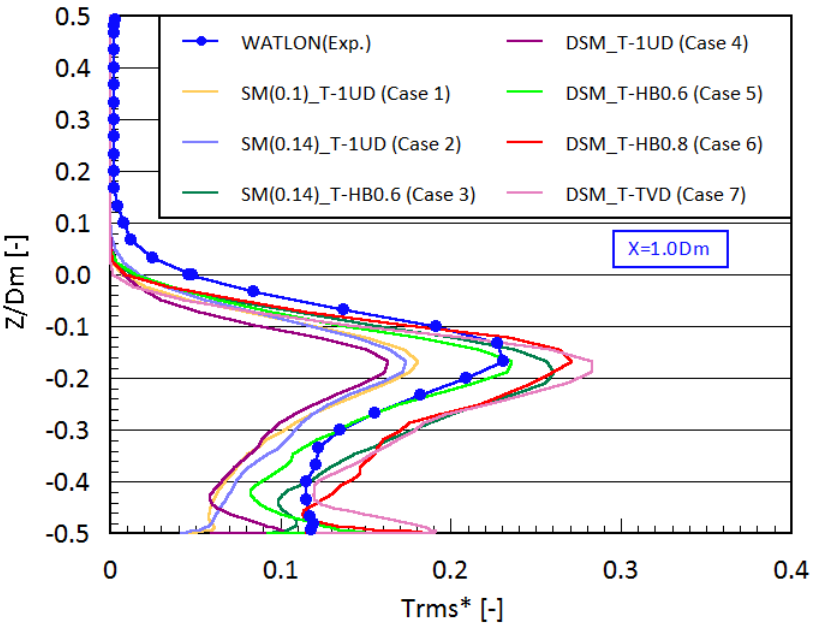

(b) X=1.0D_m

Fig. 4-7 Distribution of Fluid Temperature Fluctuation Intensity along Radial Direction

In **Fig.4-7** and **Fig.4-9**, the calculated results for the fluid temperature fluctuation intensity are compared with the experimental ones obtained in the WATLON test [83]. **Fig.4-7** shows the distributions of fluid temperature fluctuation intensity (TFI) along the radial direction at x=0.5D_m and 1.0D_m. For clarity, the locations and direction of the lines on the plot are indicated with the arrowed pink lines in **Fig.4-3.** **Fig.4-9** shows the distributions of TFI along the

circumferential direction at x=0.5D_m and 1.0D_m. Similarly for clarity, the locations and direction of the lines on the plot are indicated with the pink lines and an arrowed curve in **Fig.4-8**.

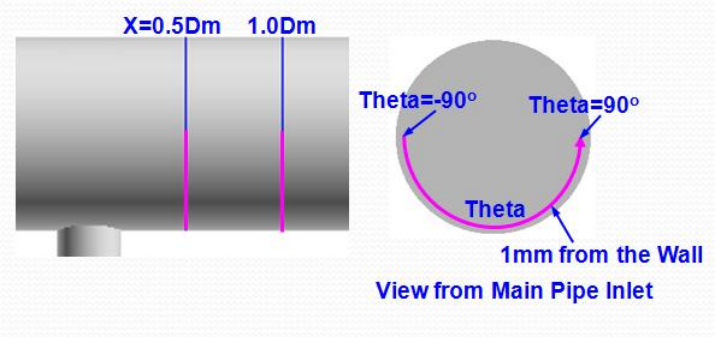

Fig. 4-8 Locations and Direction of the Lines (Pink) on the Plot in Fig. 4-9

From **Fig.4-7** and **Fig. 4-9**, it can be found that, when the 1UD scheme is used for calculating the convective term in the energy equation (Case 1, Case 2 & Case 4), the fluid temperature fluctuation intensity is significantly under-estimated for both, SSM and DSM models, compared with the experimental results. Moreover, almost no effect on the calculated TFI is observed while changing the model constant C_s from 0.1 (Case 1) to 0.14 (Case 2) in the SSM model. This is attributed to the fact that the numerical diffusion is dominant relative to the turbulent diffusion.

It can also be observed from **Fig.4-7** and **Fig. 4-9** that, when the hybrid scheme with a blending factor of $\alpha_{bf} = 0.6$ is used instead of the 1UD scheme (Case 3 & Case 5), the calculated TFI will obviously increases for both SSM and DSM models. However, there still exists a discrepancy between the calculated and experimental results for near-wall TFI along the circumferential direction (**Fig. 4-9**) which is directly related to the thermal fatigue loading. Furthermore, the calculated TFI for the SSM is much smaller than that for the DSM. When the hybrid scheme with a larger blending factor ($\alpha_{bf} = 0.8$) or TVD scheme is used in combination with the DSM model (Case 6 & Case 7), the TFI predictions for the numerical analysis are close to the experimental results along both the radial (**Fig. 4-7**) and circumferential (**Fig. 4-9**) directions and, moreover, are a little conservative (or slightly larger than the experimental results) for the TFI distributions along both the radial and circumferential directions. The

slightly conservative prediction of TFI is more desirable than an underestimation for the thermal fatigue evaluation.

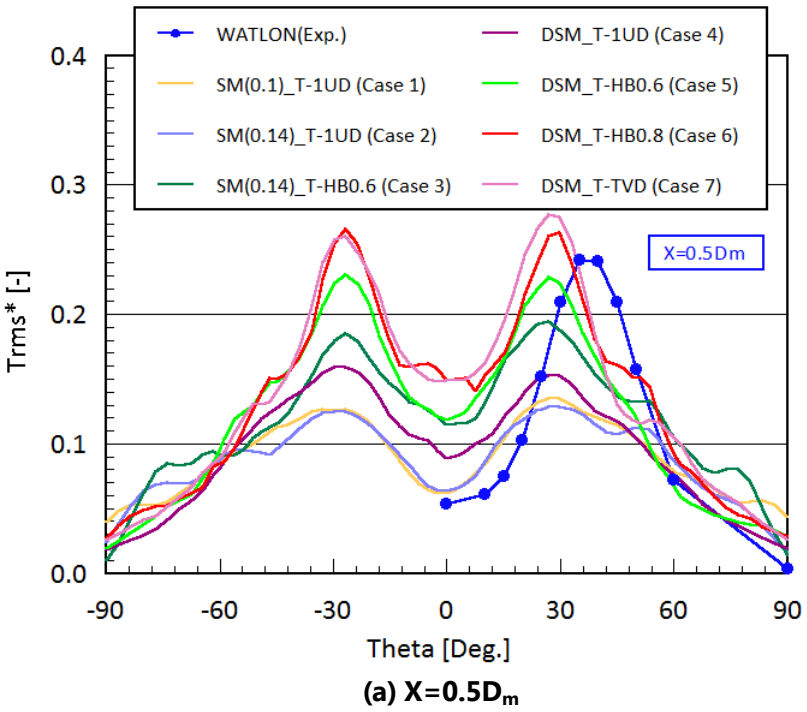

(a) X=0.5D_m

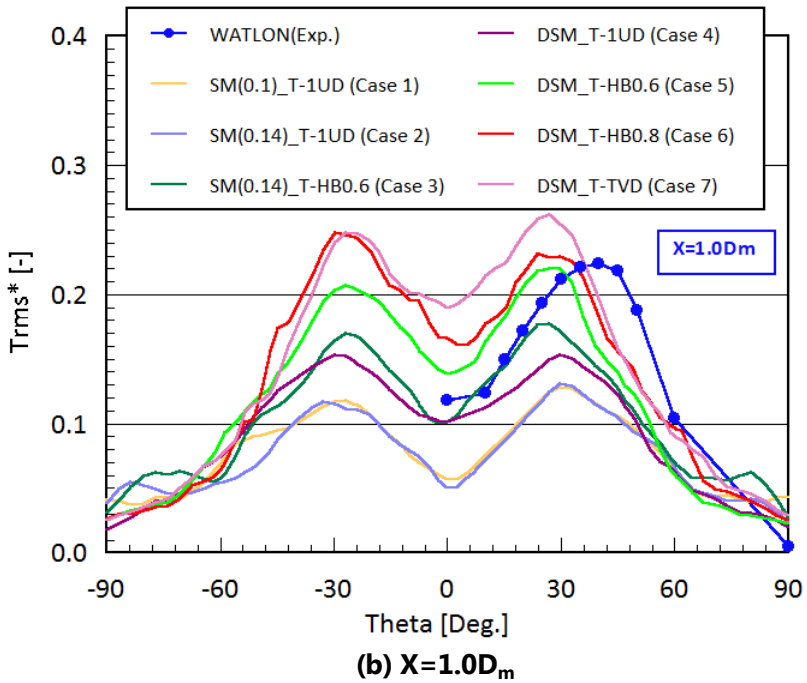

(b) X=1.0D_m

Fig. 4-9 Distribution of Fluid Temperature Fluctuation Intensity along Circumferential Direction

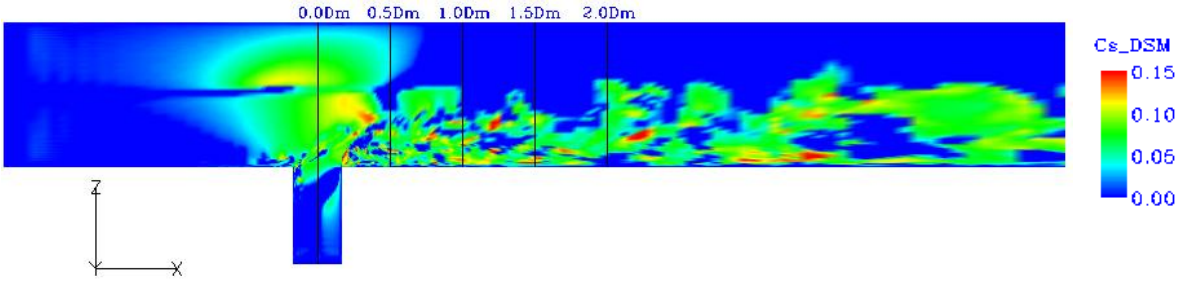

Fig. 4-10 Distribution of the Parameter C_s Evaluated in the DSM model

These results for the numerical analyses show that it is desirable to adopt the DSM model for the turbulence model and the hybrid scheme with a large blending factor or TVD scheme for the calculation of the convective term in the energy equation when carrying out numerical simulations of the fluid temperature fluctuations at T-junctions. For the LES SGS turbulence model, the turbulent eddy viscosity is proportional to the square of the model parameter C_s. The model parameter C_s is treated as a constant (usually with a value above 0.10) in the SSM model, but it is more accurately evaluated as a function of the local flow field in the DSM model. **Fig.4-10** shows distribution of the parameter C_s calculated using the DSM model in Case 6. Obviously, compared with the DSM model, the SSM model over-evaluates the parameter C_s and the turbulent eddy viscosity in most areas of the computational domain. As a result, the fluid temperature fluctuation intensity is numerically attenuated due to the over-evaluated turbulent diffusion in the SSM model. However, the DSM model can more accurately evaluate the turbulent eddy viscosity and, therefore, results in a more accurate prediction of the fluid temperature fluctuation intensity. As for the numerical scheme for calculating the convective term in the energy equation, the hybrid scheme or TVD scheme has a lower numerical diffusion effect than the 1UD scheme has. The larger the blending factor in the hybrid scheme becomes, the smaller the numerical diffusion becomes. Hence, a large blending factor for hybrid scheme can result in predictions of the fluid temperature fluctuation amplitudes close to the experimental results or a little larger than the experimental ones, the latter of which are conservative predictions for thermal fatigue evaluation and, thus, desirable. However, the value of the blending factor used is limited, considering numerical stability. The numerical analysis

becomes unstable if an excessively large blending factor is used with a relatively coarse mesh. On the other hand, the numerical diffusion will become large if a small blending factor is used. The large numerical diffusion can artificially attenuate the predicted fluid temperature fluctuation amplitudes, which will lead to the under-evaluation of thermal fatigue and, hence, be risky. Therefore, it is important to choose a blending factor as large as possible for a specific mesh, on condition that the numerical stability is maintained. In addition, similar to the hybrid scheme with a large blending factor, the TVD scheme also has a very small numerical diffusion and, hence, is suitable for prediction of fluid temperature fluctuations as well.

4-5-3 Fluid Temperature Fluctuation Frequency

Fig.4-12 shows the temporal variation of fluid temperature at the sampling point in Case 6. **Fig.4-11** indicates the location of the sampling point (pink point), which is located 1mm from the pipe wall on the cross-section at $x=1.0D_m$ and at an angle of 30º from the vertical symmetrical plane. The sampling time period is 5.5 seconds, with a sampling time interval of 0.001sec. It can be found from **Fig.4-12** that the fluid temperature irregularly fluctuated with a large amplitude at the sampling point near the wall.

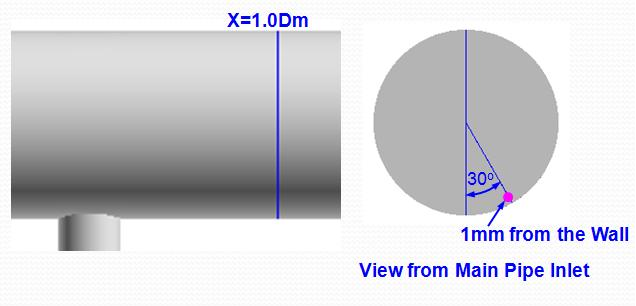

Fig. 4-11 Location of the Temperature Sampling Point

Fig.4-13 shows the power spectrum density (PSD) obtained by a fast Fourier transform (FFT) of the time series of the fluid temperature shown in **Fig.4-12**. There exists a prominent peak at a frequency of 5.86 Hz. This agrees with the frequency of 5.86 Hz predicted by Nakamura et al. [140], who performed the dynamic LES using Fluent Ver.12. In addition, Igarashi et al. [74] found that the peak frequency agreed well with the shedding frequency of a Karman vortex

street in the wake of a cylinder with the same diameter as the branch jet. The shedding frequency f of Karman vortex can be normalized as Strouhal number as follows:

$$St = fD_b / V_m \tag{4-8}$$

The Strouhal number of flow around a circular cylinder can be nearly taken as $St = 0.2$ for $\mathrm{Re} = \rho_m V_m D_b / \mu_m = 9.64 \times 10^4$. As a result, the shedding frequency $f = 5.84 Hz$ is obtained by substituting the value of St into Eq.(4-8). The frequency of the main peak of PSD in **Fig.4-13** is 5.86 Hz, which agrees very well with the value of 5.84 Hz estimated from Eq.(4-8). The results show that the vortex shedding frequencies are almost identical for the flows around a solid circular cylinder and a branch jet of the same diameter, although it is considered that their flow fields are remarkably different.

In addition, the frequency of the main peak of PSD for Case 7 is 5.37 Hz, which is also close to the value of 5.84 Hz estimated from Eq.(4-8).

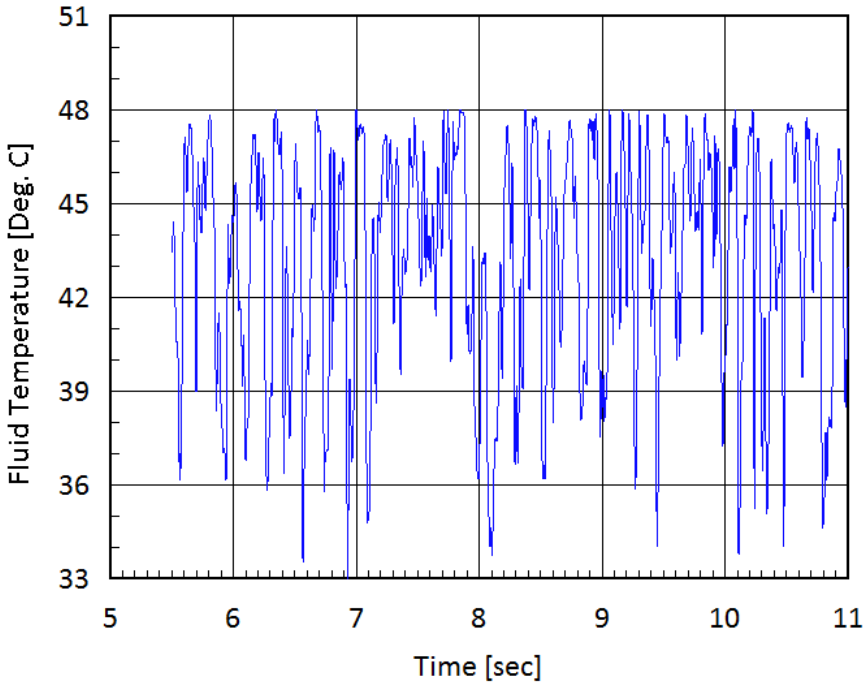

Fig. 4-12 Temporal Variation of Fluid Temperature at the Sampling Point at 1mm from the Pipe Wall, x=1.0D_m, Theta=30° (Case 6)

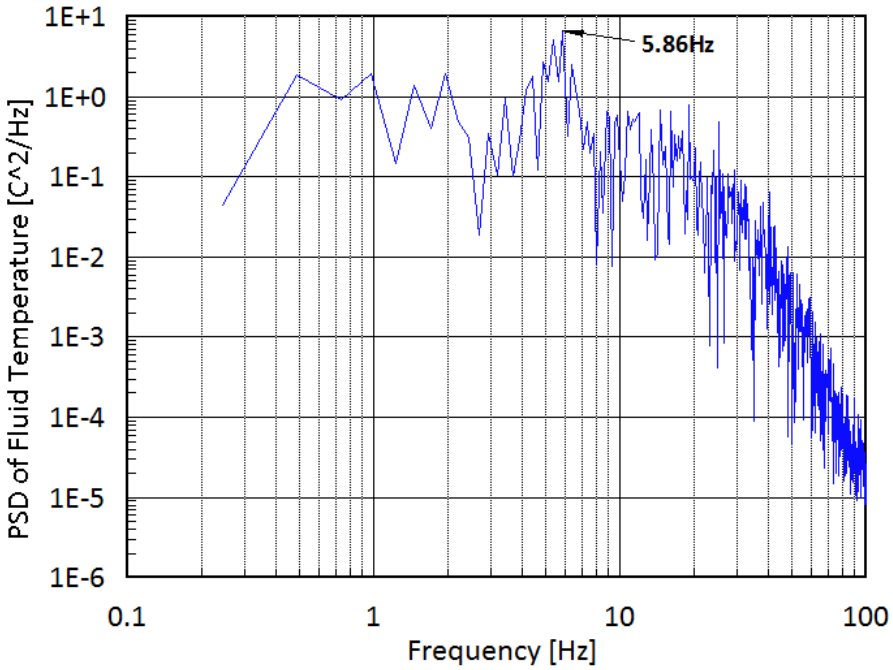

Fig. 4-13 PSD of Fluid Temperature at the Sampling Point at 1mm from Pipe Wall, x=1.0D_m, Theta=30° (Case 6)

4-6. Summary

The scenario of LES benchmark simulations shown in **Table 4-5** was proposed to establish the high-accuracy prediction methods of fluid temperature fluctuations (FTF), considering that the potentially over-evaluated turbulent eddy viscosity by LES turbulence models and numerical diffusion of differencing schemes may remarkably attenuate the predicted FTFs. The LES SGS turbulence models chosen were the standard Smagorinsky model (SSM) and the dynamic Smagorinsky model (DSM). The effects of the model parameter on the results were also investigated for the SSM model. Moreover, the effects of three differencing schemes for calculating the convective term in the energy equation were investigated as well. The LES benchmark simulation results were compared with the experimental ones to verify the prediction accuracy of fluid temperature fluctuations.

For the LES SGS turbulence model, the SSM model can reproduce the fluctuating temperature fields at the T-junction to some extent, but it under-estimates the fluid temperature fluctuation intensity due to the over-evaluated turbulent diffusion. However, the

DSM model is capable of more accurately reproducing the temperature fluctuations than the SSM model, as the model parameter C_s in the DSM model is evaluated as a function of the local flow field, different from that C_s is treated as a constant in the SSM model.

Numerical difference schemes for calculating the convective term in the energy equation have great effects on the predicted results. The hybrid scheme (HS) with a large blending factor and the TVD scheme, which produce much smaller numerical diffusion, is more suitable for simulating unsteady temperature fields than the 1st-order upwind difference (1UD) scheme.

As a result, an approach using the DSM model and the hybrid scheme with a large blending factor or the TVD scheme can predict the fluid temperature fluctuations well, when compared with the experimental results. Moreover, the predicted peak frequency of the temperature fluctuations near the pipe wall is very close to the estimation by Igarashi et al. [74].

Therefore, as shown in **Table 4-6**, it is recommended that the approach using the DSM model and the hybrid scheme with a large blending factor or the TVD scheme be applied for accurately simulating the fluid temperature fluctuations at T-junctions. Moreover, it can be considered that this approach is also applicable to the high-accuracy prediction of any other scalar (for example, concentration), based on the analogy of scalar transport equations.

Table 4-6 High-Accuracy Prediction Methods of Fluid Temperature Fluctuations

LES Turbulence Model	Dynamic Smagorinsky SGS Model (DSM)
Difference Scheme for Calculation of Convective Term	● Hybrid Scheme with a Blending Factor as Large as Possible ● TVD 2nd-Order Upwind Difference Scheme

Appendix 4-1 Investigation of the Effects of Grid Size and Time Step Interval on CFD Simulation Results

LES simulations of flow and temperature fields at a T-junction were carried out to investigate the effects of grid size and time step interval on the CFD-predicted results using three different meshes and three time step intervals, respectively. The computational conditions and numerical

methods used in the LES simulations are the same as those applied for Case 6 shown in **Table 4-5**, except the investigated factor (mesh or time step interval). Case 6 in **Table 4-5** is used as a basic case and here renamed as Case A-1. For Case A-1, the mesh used has about 1,022,000 cells and the time step interval is Δt=0.0002 sec.

For investigating the effect of grid size, LES analyses were performed for additional two different meshes with the number of cells being about 680,000 (Coarser Mesh, Case A-2(CM)), and 1,532,000 (Finer Mesh, Case A-3(FM)), using the same time step interval of Δt=0.0002 sec. The CFD results of fluid temperature fluctuation intensity (TFI) for three different meshes (Case A-1, Case A-2(CM) and Case A-3(FM)) are compared with each other and as well with the experimental ones [83] in **Fig.4-14** and **Fig.4-15**. **Fig.4-14** shows the distributions of TFI along the radial direction at x=0.5D_m (see **Fig.4-3** for the location of plot). **Fig.4-15** shows the distributions of TFI along the circumferential direction at x=0.5D_m (see **Fig.4-8** for the location of plot). It can be found from **Fig.4-14** and **Fig.4-15** that difference between the CFD results for three different meshes is very small, and moreover, the CFD results are close to the experimental ones. Therefore, it is considered that the spatial resolution of the mesh with about 1,022,000 cells is adequate for the present research.

At the same time, for investigating the effect of time step interval, LES simulations were also carried out using additional two different time step intervals of Δt=0.0001 sec (Smaller DT, Case A-4(SDT)) and Δt=0.0004 sec (Larger DT, Case A-5(LDT)) for the same mesh with about 1,022,000 cells. Similarly, the CFD results of fluid temperature fluctuation intensity for three different time step intervals (Case A-1, Case A-4(SDT) and Case A-5(LDT)) are also compared with each other and as well with the experimental ones [83] in **Fig.4-14** and **Fig.4-15**. **Fig.4-14** shows the distributions of TFI along the radial direction at x=0.5D_m. **Fig.4-15** shows the distributions of TFI along the circumferential direction at x=0.5D_m. It can also be found from **Fig.4-14** and **Fig.4-15** that the CFD results for three different time step intervals are very close and, moreover, near the experimental ones. Hence, it is considered that the chosen time step intervals of Δt=0.0002 sec is sufficiently accurate for the present research.

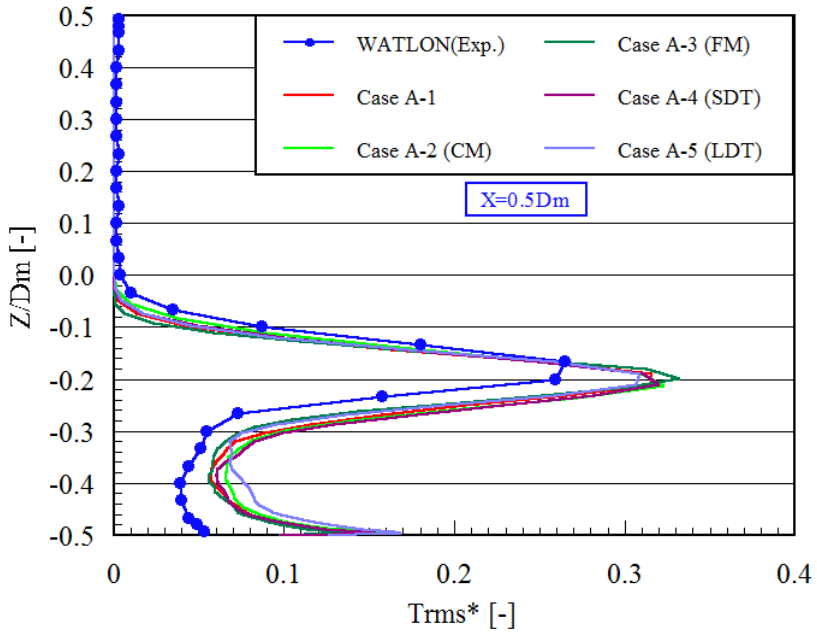

Fig. 4-14 Distribution of Fluid Temperature Fluctuation Intensity along Radial Direction

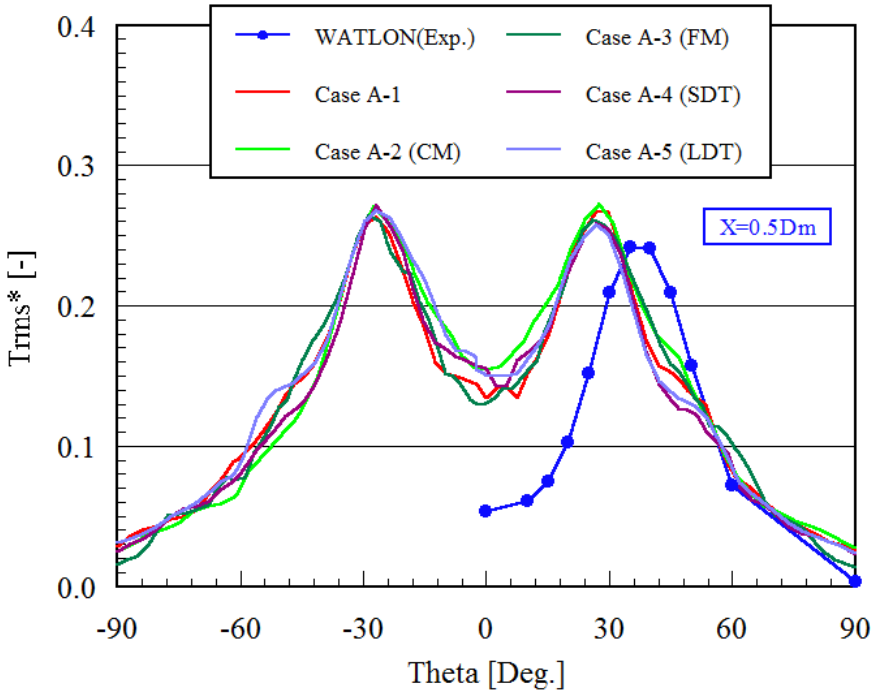

Fig. 4-15 Distribution of Fluid Temperature Fluctuation Intensity along the Circumferential Direction

Chapter 5 High-Accuracy Prediction Methods of Structure Temperature Fluctuations as Thermal Loading

5-1 Introduction

As described before, the goal of this study is to establish an integrated evaluation method of high-cycle thermal fatigue based on CFD/FEA coupling analysis. It is necessary to predict the fluctuation amplitudes and cycle numbers (or frequencies) of thermal stress caused by the structure temperature fluctuations using FEA, for evaluating thermal fatigue damage. The structure temperature fluctuations are induced through heat transfer from fluid to structure. Therefore, it is very important to predict accurately the fluid and structure temperature fluctuations (or thermal loadings) for high-accuracy evaluation of thermal fatigue.

In **Chapter 4**, the high-accuracy prediction methods of fluid temperature fluctuations at a T-junction have been established, by comprehensively investigating the effects of LES sub-grid scale (SGS) turbulence models, and numerical difference schemes of calculating the convective term in the energy equation on the simulation results for fluid temperature fluctuations. Specifically, the approach using DSM-based LES in combination with a hybrid scheme (HS) with a sufficiently large blending factor or a 2nd-order accurate TVD scheme can predict the fluid temperature fluctuations with high accuracy and slight conservativeness. In view of this, it is further needed to establish high-accuracy methods of predicting the structure temperature fluctuations at a T-junction for more accurate evaluation of thermal fatigue.

As described in **Chapter 1**, so far the predictions of structure temperature fluctuations (or thermal fatigue loading) were almost performed either using a constant heat transfer coefficient evaluated from the empirical equation (e.g. Dittus-Boelter equation) [42] [55], or using the wall functions [72] [84] [85]. However, such evaluation methods of heat transfer coefficient between fluid and structure are not sufficiently accurate for thermal fatigue evaluation because the former method based on the empirical equation is incapable of considering the unsteady heat transfer and the latter method based on the wall functions usually under-evaluate the heat

transfer coefficient. It is considered that CFD simulation of both fluid flow and thermal interaction between fluid and structure at a T-junction can provide high-accuracy predictions of fluid and structure temperature fluctuations if adopting proper numerical methods (see **Fig. 5-1** and relevant descriptions in **Section 5-2** for the details). As the thermal loading, the time series of structure temperatures obtained by CFD simulation is needed as the input for an FEA analysis of thermal stress fluctuation. It is very important to verify the numerical accuracy for the simulation results of fluid and especially structure temperature fluctuations by CFD benchmark analysis, prior to the CFD/FEA coupling analysis, for more accurate evaluation of HCTF. It is expected that as a tool of numerical fluid experiment, such high-accuracy prediction methods are able to not only enhance the prediction accuracy of fluid and structure temperature fluctuations (or thermal loadings) but also to expand the application area of thermal loading evaluation and take into account the dependency of attenuation of structure temperature fluctuations on the frequency of fluid temperature fluctuations.

The present investigation aims to establish high-accuracy CFD prediction methods of structure temperature fluctuations at T-junction through the benchmark simulation of fluid flow and thermal interaction between fluid and structure, using the proposed high-accuracy numerical methods, which include some numerical methods established in **Chapter 4**. The temperature fluctuations in structure are directly used for the thermal stress analysis and, consequently, affect the accuracy of the thermal fatigue evaluation. Hence, it is important to calculate accurately the heat transfer between a fluid and a structure. In this investigation, a fine mesh with near-wall grid points being allocated within the thermal boundary sub-layer is used, in order to evaluate the heat transfer between fluid and structure with high accuracy. The obtained CFD results, especially for the temperature fluctuations in structure, are compared with the experimental results by Kimura et al. [87] to verify the accuracy of CFD predictions.

5-2 Proposal of High-Accuracy Numerical Methods

5-2-1 Application of High-Accuracy Prediction Methods of Fluid Temperature Fluctuations

As noted above, it is very important to predict accurately both the fluid and structure temperature fluctuations for the accurate evaluation of thermal fatigue at T-junctions because temperature fluctuation of the fluid leads to temperature fluctuation in the structure, which may induce thermal fatigue. The high-accuracy numerical methods established in **Chapter 4** are applied to predict the fluid temperature fluctuations in the present research, as shown in **Table 5-3**. Specifically, a dynamic Smagorinsky SGS model (DSM) is applied for the LES SGS turbulence model, as it can predict the turbulent eddy viscosity well. At the same time, a hybrid scheme, which is mainly a 2nd-order central differencing (2CD) scheme blended with a small fraction of a 1st-order upwind difference (1UD) scheme, is applied for calculation of convective terms in momentum and energy equations, as such a scheme is capable of both reducing the numerical (or artificial) diffusion as much as possible and maintaining the numerical stability. The main features for the dynamic Smagorinsky SGS model and the hybrid scheme have been described in **Chapter 2**.

In summary, the high-accuracy numerical methods chosen to predict the fluid temperature fluctuations are concisely described as follows:

(1). Dynamic Smagorinsky SGS model (DSM) for LES SGS turbulence model

(2). Hybrid scheme with a large blending factor for differencing scheme of convective terms

5-2-2 Proposal of High-Accuracy Analysis Methods of Fluid-Structure Thermal Interaction

It is necessary to calculate accurately the heat transfer between a fluid and a structure for the accurate prediction of temperature fluctuations in the structure. As shown in **Fig. 5-1**, it is considered that usually the two approaches can be chosen for the CFD/FEA coupling analysis.

- Approach 1: For the traditional Approach 1 shown in **Fig. 5-1 (a)**, only the fluid temperature fluctuations are simulated by CFD, and the structure temperature fluctuations are predicted through FEA using the CFD-predicted near-wall fluid temperature data as

thermal boundary conditions, as well as the heat transfer coefficients. However, the heat transfer coefficients between fluid and structure need to be evaluated utilizing an empirical or semi-empirical formulation [42] [55] and hence, it is difficult to reach a sufficiently high accuracy especially for the highly fluctuating unsteady temperature fields at a T-junction.

- Approach 2: On the other hand, for Approach 2 shown in **Fig. 5-1 (b)**, fluid flow and thermal interaction between fluid and structure are simultaneously simulated by CFD. Hence, a high-accuracy prediction of structure temperature fluctuations can be reached if using proper numerical methods. Therefore, Approach 2 was chosen in the present investigation.

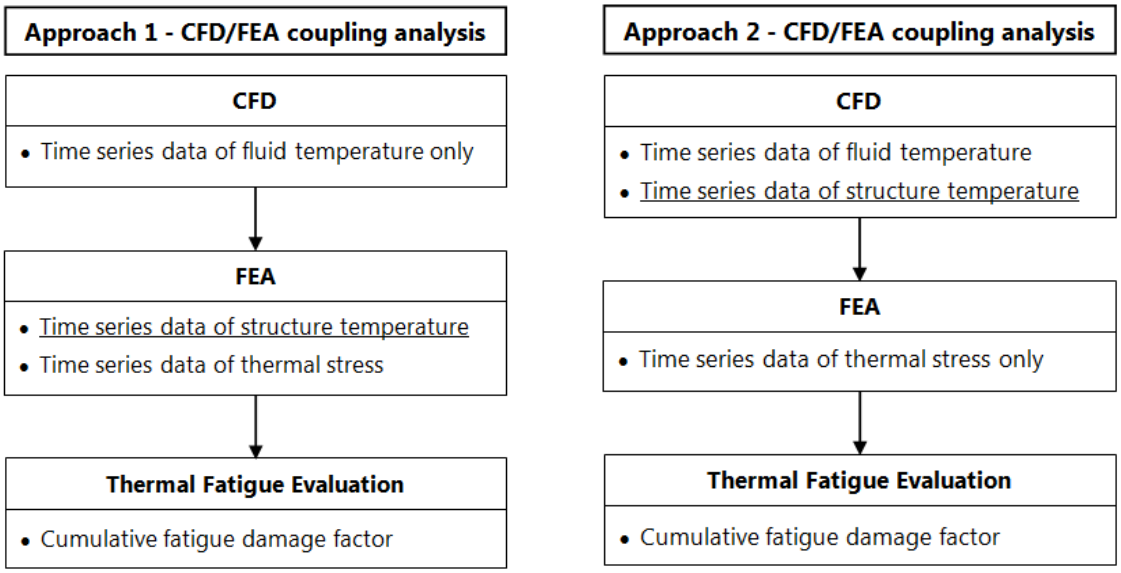

(a) Approach 1 **(b) Approach 2**

Fig. 5-1 Two Approaches for CFD/FEA Coupling Analysis

Even if Approach 2 is chosen, the prediction accuracy of structure temperature fluctuations still depends on the evaluation method of heat transfer between fluid and structure. There are the following two methods for calculating heat transfer between fluid and structure.

- Wall functions based method: To date, the heat transfer between fluid and structure were almost evaluated using wall functions for a relatively coarse near-wall mesh [72] [84] [85], as described above. However, such evaluation method of heat transfer coefficient between fluid and structure is not sufficiently accurate for thermal fatigue evaluation of T-junctions, as the

flow separation take places in the mixing zone and wall functions are not suitable for prediction of separation flow [123]. In view of this, a preliminary investigation shown in **Appendix 5-1** was carried out using the wall functions for a relatively coarse near-wall mesh, in order to confirm the prediction accuracy of structure temperature fluctuations for such method. The investigation results show that the predicted maximal amplitude of structure temperature fluctuations based on wall functions is just about 55% of the experimental results and the CFD-predicted results for a fine mesh with near wall resolution (NWR).

- **Near wall resolution (NWR) based method:** Another method is that the near-wall grid points are allocated within the thermal boundary sub-layer (or thermal conduction layer) by generating a fine mesh with near wall resolution (NWR), and consequently, heat transfer between fluid and structure can be calculated directly through thermal conduction for both sides of fluid and structure. Therefore, it is expected that this method is able to evaluate more accurately the heat transfer between fluid and structure. In view of this, such a method was proposed to predict accurately the structure temperature fluctuations here.

At the same time, the following two methods were proposed to evaluate accurately the thermal interaction between the fluid and the structure.

- A coarse mesh of the structure region can lead to numerical attenuation of the structure temperature fluctuations. Hence, besides the fluid region, a very fine mesh near the inner wall of pipe was also created for the structure region, in order to predict accurately the near-wall structure temperature fluctuations (see **Section 5-4-1** for the details).
- Energy equations for the fluid and structure regions were coupled through heat flux across the interface between fluid and structure, and moreover, were simultaneously solved in a fully implicit numerical scheme in order to predict accurately the structure temperature fluctuations (see **Section 5-4-3** for the details).

In summary, the three numerical methods proposed above to evaluate accurately the heat transfer between fluid and structure are concisely described below, following the numbering in **Section 5-2-1**.

(3). Direct calculation of heat flux between fluid and structure through thermal conduction by allocating all the near-wall grid points within thermal boundary sub-layer

(4). Creation of a very fine mesh for structure region near the inner wall of pipe

(5). Coupled and simultaneous solution of energy equations for the fluid and structure regions in a fully implicit scheme

5-2-3 Proposal of Estimation Method of Thickness of Thermal Boundary Sub-layer

It is necessary to know the thickness of thermal boundary sub-layer to ensure that all the near-wall grid points were located within the thermal boundary sub-layer for creating an NWR mesh. The dimensionless thickness of thermal boundary sub-layer is dependent on the Prandtl number of a fluid, different from that of flow boundary sub-layer, which is a constant independent of the type of a fluid (taken as $y_F^+ = 5.5$ in the present study). In case of $\mathrm{Pr} \le 1.0$, the thickness of thermal boundary sub-layer is equal to or larger than that of flow boundary sub-layer and, hence, the latter can be used for a basis when creating an NWR mesh. As a result, it is not necessary to estimate the thickness of thermal boundary sub-layer for the case of $\mathrm{Pr} \le 1.0$. However, if $\mathrm{Pr} > 1.0$, the thermal boundary sub-layer is thinner than the flow boundary sub-layer and, thus, it is necessary to estimate the thickness of thermal boundary sub-layer to ensure that all the near-wall grid points were located within the thermal boundary sub-layer for creating an NWR mesh. The Prandtl number for water used here is about 4.4 (shown in **Table 5-2** later) and, thus, larger than 1.0. Hence, it was necessary to estimate the thickness of thermal boundary sub-layer. In view of this, a generalized estimation method of the thickness of the thermal boundary sub-layer was proposed below, by using the wall functions for the temperature profile in the thermal boundary layer [141].

The linear law (equivalent to thermal conduction) for a laminar region and the logarithmic law (also called the wall function) for a turbulent region are, respectively,

$$T^+ = \mathrm{Pr}\, y^+ \qquad (y^+ < y_{MT}^+) \tag{5-1}$$

$$T^+ = (\mathrm{Pr}_t/\kappa)\ln y^+ + B \qquad (y^+ \ge y_{MT}^+) \tag{5-2}$$

with the dimensionless temperature $T^+=(T_w-T)/T_\tau$, the dimensionless distance $y^+=u_\tau y\rho/\mu$, $B=(3.85\mathrm{Pr}^{1/3}-1.3)^2+(\mathrm{Pr}_t/\kappa)\ln\mathrm{Pr}$, $T_\tau=q_w/(\rho c_p u_\tau)$, $u_\tau=\sqrt{\tau_w/\rho}$, $Pr_t=0.85$ and $\kappa=0.42$. Here, T_w and T are the temperature on the pipe wall surface and the fluid temperature at the center of the cell nearest to the wall, respectively; q_w is the heat flux across the wall; T_τ and u_τ are called the friction temperature and velocity, respectively; τ_w is the shear stress near the wall; and Pr_t is the turbulent Prandtl number. The intercept of the linear law and the logarithmic law can be obtained for a specific Prandtl number (Pr), by simultaneously solving equations (5-1) and (5-2), and then, the dimensionless thickness of its thermal boundary sub-layer can empirically be estimated as below.

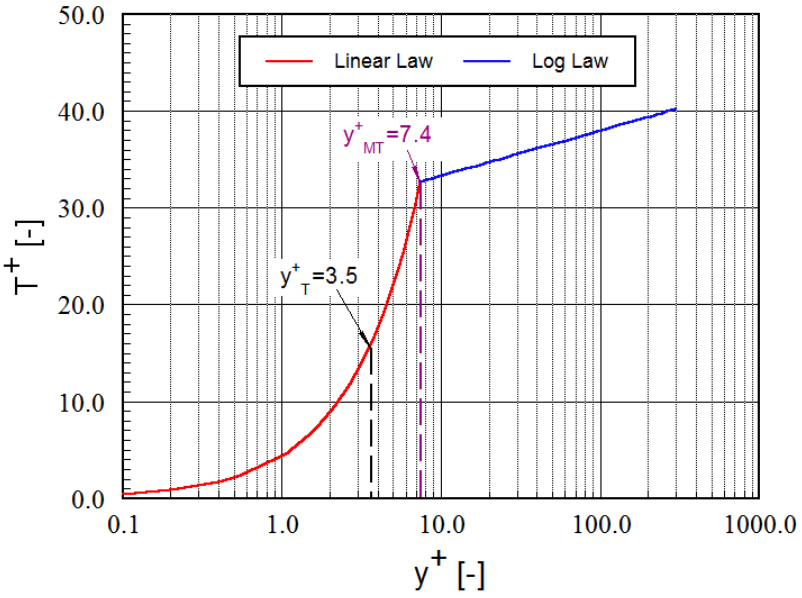

Fig. 5-2 Estimation of Thickness of Thermal Boundary Sub-layer for Pr=4.4

The dimensionless temperature profile in the thermal boundary layer is plotted in **Fig. 5-2** for Pr=4.4 of the water used here, based on equations (5-1) and (5-2). Their intercept was obtained as $y_{MT}^+=7.4$ by simultaneously solving equations (5-1) and (5-2). When calculating the near-wall heat transfer coefficient based on the wall function, usually the intercept value (y_{MT}^+) is used as the bound between the equations (5-1) and (5-2). That is to say, y_{MT}^+ is regarded as

the thickness of the thermal boundary sub-layer. However, the temperature profile around the intercept deviates from equation (5-1) to some extent for the laminar region. It is empirically proper to take about half of y^+_{MT} as the thickness of the thermal boundary sub-layer, similar to that for the flow boundary layer. Hence, $y^+_T = 3.5$ can be taken as a slightly safe estimation of the thickness of the thermal boundary sub-layer here. That is to say, $y^+_T = 3.5$ is surely located within the thermal boundary sub-layer for the case of Pr=4.4.

5-3 Experimental Conditions for Benchmark Simulation

The present investigation aims at establishing high-accuracy prediction methods of fluid and structure temperature fluctuations (or thermal loading) through CFD benchmark simulation. For the sake of comparison, the adopted simulation conditions were the same as one case among the experiments conducted by Kimura et al. [87]. The test section comprised a horizontal main pipe and a vertical branch pipe with the inner diameters being 150 mm and 50 mm, respectively. The part of the main pipe used for measuring the temperature in the structure was made of the stainless steel, SUS304. The fluid temperature distribution in the radial direction of the main pipe was measured using a thermocouple tree with 17 thermocouples. The measuring point in the structure was located at 0.125mm from the inner wall surface. The flow velocity distribution at the T-junction was measured using a particle image velocimetry (PIV) system.

Kimura et al. [87] performed a series of tests under 6 different conditions. In the present investigation, the conditions of Case 3 for the flow pattern of wall jet were chosen for the numerical simulations because the experimental conditions and results for this case have previously been reported in detail. The detailed conditions are shown in **Table 5-1**. The flow pattern at a T-junction can be classified by the following criteria (or the Criteria 3 in **Chapter 3**), based on the interacting momentum ratio (M_R) between the main pipe and branch pipe streams.

Wall Jet $4.0 < M_R$

Deflecting Jet $0.35 < M_R < 4.0$

Impinging Jet $M_R < 0.35$

where the momentum ratio M_R is defined [19] as follows:

$$M_m = D_m D_b \rho_m V_m^2 \tag{5-3}$$

$$M_b = \pi D_b^2 \rho_b V_b^2 / 4 \tag{5-4}$$

$$M_R = M_m / M_b \tag{5-5}$$

The fluid used was water. The temperatures of the water at the inlets of the main pipe and the branch pipe were $T_m = 48^\circ C$ and $T_b = 33^\circ C$, respectively. The dependence of the physical properties of the fluid and structure on temperature was negligible, as the range of temperature variation was narrow ($15^\circ C$) in the present simulations. Specifically, the variation of the fluid density was less than 0.5% between $33^\circ C$ and $48^\circ C$. As shown in **Table 5-2**, the physical properties of water and the structure material (SUS304) at the temperature of $(T_m+T_b)/2$ were used for the simulations.

Table 5-1 Main Simulation Conditions

	Main Pipe	Branch Pipe
Inflow Velocity at Inlet [m/s]	1.46	1.00
Reynolds Number [-]	3.8×10^5	6.6×10^4
Temperature of Inflow Fluid [$^\circ C$]	48	33
Inner Diameter of Pipe [mm]	150	50
Thickness of Pipe [mm]	5.0	5.0
Momentum Ratio(M_R) [-]	8.14 (Wall Jet)	

Table 5-2 Physical Properties of Fluid and Structure

	Fluid	Structure
Density [kg/m3]	991.71	8000
Viscosity [Pa.s]	0.0006652	-
Specific Heat [J/kg.K]	4179.68	499.8
Thermal Conductivity [W/m.k]	0.62849	16.3
Prandtl Number [-]	4.424	-

5-4 Computational Model and Boundary Condition and CFD Simulation Methods

5-4-1 Computational Model

The computational model and main boundary conditions for the T-junction are shown in **Fig. 5-3**. The lengths of the inlet section were set as $2D_m$ (D_m=150 mm) for the main pipe and $2D_b$ (D_b =50 mm) for the branch pipe, and the length of the outlet section was set as $5D_m$ to reduce the number of cells in the mesh to reduce the computation time. These settings were reasonable because the reducer nozzles and sufficiently long straight pipes were installed upstream of the main pipe and branch pipe for straightening the flow into the T-junction in the experimental apparatus [87], and the fully developed turbulent flow profiles were applied for the main pipe and branch pipe inlets in the present investigation (see below for details). The present investigation was intended to simulate the temperature fluctuations of both fluid and structure using the LES SGS turbulence model, and hence the pipe thickness was also included in the simulations. It should be pointed out that all parts of test pipes were treated as stainless steel in the LES simulation, in order to perform FE analysis of thermal stress of the entire pipes using the time series of structure temperature obtained by CFD simulation and then carry out thermal fatigue evaluation using the obtained thermal stresses, although only one part of the test pipes was made of stainless steel for measuring the temperature in structure and the rest were made of acrylic resin for visualization in the experiment of [87]. The heat flux exchanged between fluid and the wall of thin pipe is very small relative to the strong convective heat transport of fluid and, hence, has a very little effect on the fluid temperature, even though all parts of test pipes are treated as stainless steel in the LES simulation. Meanwhile, the measuring point in structure is near the inner wall of pipe and, moreover, far away from the cut edges of the metal test plate in the axial and circumferential directions. Therefore, it is considered that our LES simulation results can still be compared with the experimental results.

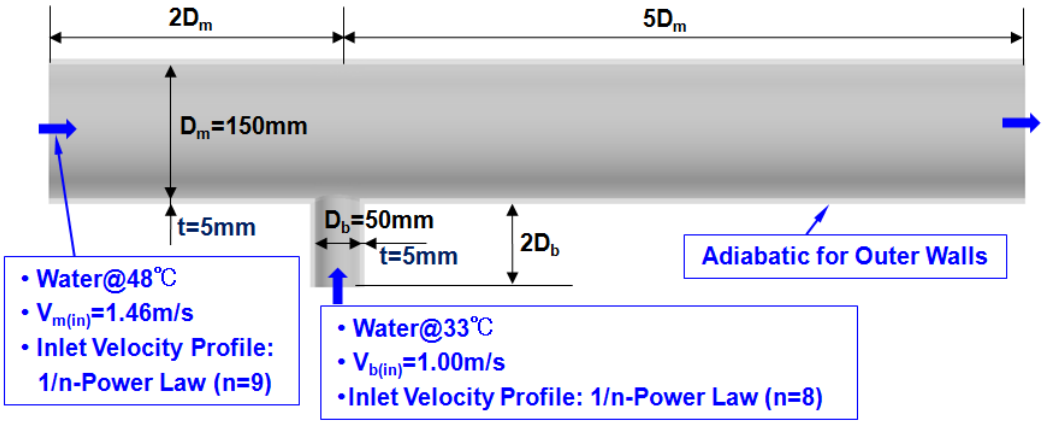

Fig. 5-3 Geometry of Computational Model and Boundary Conditions

The meshes used for the simulations comprised a fluid region (pink part) and a structure region (blue part), as shown in **Fig. 5-4**. As described in **Section 5-2-3**, the dimensionless thickness of thermal boundary sub-layer was estimated as $y_T^+ = 3.5$ for Pr=4.4 of the water used. A rather fine mesh near the inner wall of pipe was generated for the fluid region, and the near-wall cell size was uniformly 0.0348 mm, which kept the dimensionless cell size $y^+ < 3.5$ (in fact, y^+ for most of near-wall cells is below 2.0), to ensure that all the grid points nearest to the wall were located within the thermal boundary sub-layer for creating an NWR mesh. As a result, all the grid points nearest to the wall were also located within the viscous sub-layer for the flow field because the thermal boundary layer is thinner than the flow boundary layer for water with Pr > 1.0.

At the same time, a very fine mesh near the inner wall of pipe was also created for the structure region, as a coarse mesh of the structure region can lead to numerical attenuation of the structure temperature fluctuations, which are very important for thermal fatigue evaluation. The near-wall cell size was uniformly 0.0342 mm, which was almost the same as the neighboring cell size on the fluid side. The total number of cells in the mesh was about 1,990,000, which comprised about 1,620,000 cells in the fluid region and about 370,000 cells in the structure region.

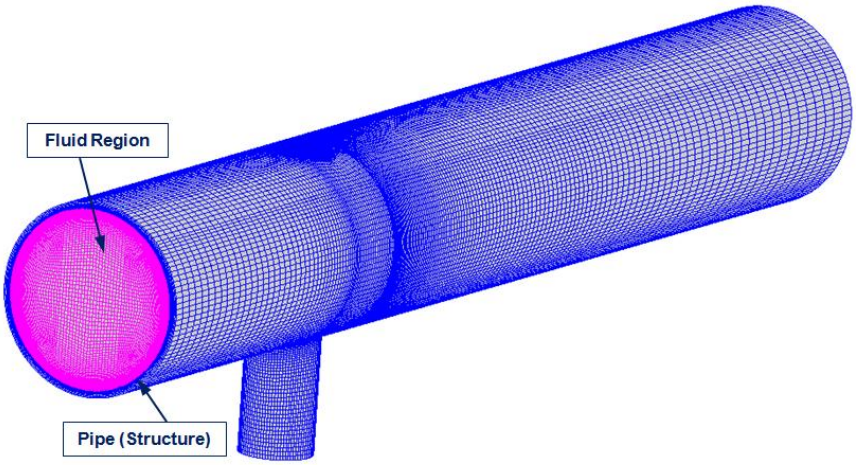

Fig. 5-4 Meshes for Computational Model

5-4-2 Boundary Conditions

As shown in **Fig. 5-3,** all the outer pipe walls were set as adiabatic for the thermal boundary condition, as the outside was thermally insulated. For the flow boundary condition, no slip was applied for all the inner pipe walls, as all the near-wall grid points were located within the viscous sub-layer.

The mean flow velocities and water temperatures at inlets of the main and branch pipes are shown in **Table 5-1** and **Fig.5-3**. In view of the fact that the lengths of the inlet and outlet sections were relatively short, some measures were taken when setting the inlet and outlet conditions. For a fully developed turbulent flow, a 1/n-power law [137] was applied for the inlet velocity profile to reduce the effects of the short inlet section as far as possible. The 1/n-power law can be written as follows:

$$u/u_{\max} = (y/R)^{1/n} \tag{5-6}$$

$$n = 3.45\,\mathrm{Re}^{0.07} \tag{5-7}$$

where u is the time-averaged velocity at a distance of y to the pipe wall, $u_{\max}$ the velocity at the center of pipe inlet, R the inside radius of the pipe and Re the Reynolds number based on the averaged velocity. The values, $n_m = 9$ and $n_b = 8$, can be obtained by substituting the Reynolds numbers in **Table 5-1** into Eq. (5-7) and rounding off to the nearest whole number. However, the

turbulence intensity at the inlet was not considered in the present simulations because the temperature fluctuations downstream of the mixing tee were dominantly caused by the fierce mixing of the cold and hot fluids coming from the main and branch pipes. In fact, Nakamura et al. [139] performed the LES analyses of a T-junction for two cases, with and without consideration of the turbulence intensity at the inlet, respectively. Also, Majander et al. [26] carried out the large-eddy simulations (LES) of a round jet in a crossflow for two cases using steady and unsteady inlet boundary conditions separately. Both their results showed that the difference of the results between two cases was relatively small and, thus, negligible.

In addition, a free outflow condition was applied at the outlet. Specifically, the condition of zero-gradient along the direction normal to the outlet for each quantity (including velocity components, pressure and temperature) was applied.

5-4-3 CFD Simulation Methods

LES simulations of fluid and structure temperature fluctuations at a T-junction were carried out using the modified multi-physics CFD software FrontFlow/Red [138] (see **Appendix A** for its details) for the evaluation of thermal fatigue loading. Some modifications were added to the original source code of FrontFlow/Red to evaluate accurately the thermal interaction between fluid and structure for the present research. Specifically, energy equations for the fluid and structure regions were coupled through heat flux across the interface between fluid and structure (or pipe wall), and were simultaneously solved in a fully implicit numerical scheme in order to enhance the prediction accuracy of structure temperature fluctuations, which is very important for evaluation of thermal fatigue. This can also enhance the stability of numerical solution and accelerate the convergence of the solution of energy equation.

The main numerical methods proposed are shown in **Table 5-3**. LES sub-grid scale (SGS) models and numerical schemes have been described in Section 2 and, hence, are not repeated here. A 1st-order accurate implicit Eulerian time integration scheme was applied for time advancement. A small time-step interval (Δt=0.0001 sec) was used for the LES analyses to keep

the maximal Courant number below 1.0. Based on the finding of Igarashi et al. [74], it was predicted in advance that the order of the temperature fluctuation frequency of interest was around 6.0 Hz, or the corresponding time scale was above 0.1 sec. Obviously, the time step interval used was sufficiently small relative to the time scale and, thus, had a sufficient time resolution for the temperature fluctuations of interest, even though the 1st-order Eulerian scheme was used.

Table 5-3 Main Numerical Methods Proposed

CFD Code		Modified FrontFlow/Red
Simulation Mode		Unsteady Simulation
Turbulence Model		LES SGS Turbulence Model: Dynamic Smagorinsky Model (DSM)
Spatial Discretization Method	Momentum Equations	Convective Terms: Hybrid Scheme (HS) : α*2CD +(1-α) *1UD where α is blending factor (α=0.9), 2CD stands for 2nd-order accurate central differencing, 1UD for 1st-order accurate upwind differencing Other Terms: 2nd-order accurate central differencing (2CD)
	Energy Equation	Convective Term: Hybrid Scheme (HS) : α*2CD +(1-α) *1UD where blending factor is taken as α=0.8 Other Terms: 2nd-order accurate central differencing (2CD)
Evaluation Approach for Heat Transfer between Fluid & Structure		● Direct calculation of heat flux through thermal conduction by allocating all the near-wall grid points within thermal boundary sub-layer ● Creation of a very fine mesh for structure region near inner wall of pipe ● Coupled and simultaneous solution of energy equations for the fluid and structure regions in a fully implicit scheme
Time Integration		1st-order accurate implicit time integration (backward Eulerian method)

In every time step, the iterative solution was performed for any quantity ϕ. The normalized RMS residual used for convergence judgment is defined as follows:

$$\varepsilon_{\phi}^{*} = \sqrt{\sum_{i=1}^{N}[(\phi_i^n - \phi_i^{n-1})/\phi_i^n]^2 \Big/ N} \qquad (5\text{-}8)$$

where N is the total number of cells to be solved, n and $n-1$ represent the current and last iterations, respectively. The convergence criteria were set as 1.0×10^{-5} for each velocity component and temperature, and 1.0×10^{-7} for pressure, respectively.

Procedures for simulations of flow and temperature fields included the following 3 steps:

(1) As the initial conditions of unsteady LES analysis, the flow and temperature fields were first calculated for 4.0 seconds using the realizable $k-\varepsilon$ turbulence model with a large time-step interval of Δt=0.0001 sec.

(2) LES simulation was carried out for 3.0 seconds (over 4 times the mean residence time of flow) using a small time-step interval of Δt=0.0001 sec to develop the flow and temperature fields to the quasi-periodic state.

(3) LES simulation was run for 18 seconds to carry out the statistical calculation of unsteady flow and temperature fields, using a small time-step interval of Δt=0.0001 sec. The sampling time interval was 0.001 sec, or the sampling was done once every 10 time steps.

5-5 Numerical Simulation Results and Discussions

LES simulation of fluid and structure temperature fluctuations at a T-junction was carried out for the evaluation of thermal fatigue loading, using the proposed numerical methods shown in **Table 5-3**. In the following, the simulation results for the flow field and temperature distributions of both fluid and structure at the T-junction are presented mainly through comparison with the experimental results [87]. Focus is placed on the results for the temperature distributions of fluid and especially structure, which are subsequently necessary for thermal fatigue evaluation of our interest.

5-5-1 Flow Patterns and Flow Velocity Distribution

Fig. 5-5 show the LES results for the instantaneous flow velocity vectors and temperature distribution on the vertical cross-section along the flow direction at 5 time steps. The LES results indicate that the branch jet is deflected near the main pipe wall on the branch pipe side by the relatively strong main pipe flow. This is the typical flow pattern of a wall jet and agrees with the prediction of flow pattern based on the momentum ratio and also the experimental observations by Kimura et al. [87]. The cold and hot fluids, after the meeting of the branch jet

and main pipe stream, are gradually mixed while flowing downstream along the main pipe wall on the branch pipe side. In the mixing zone, the flow is very unstable and strongly fluctuating due to the interaction between the branch jet and the crossflow from the main pipe, and consequently, the temperature field also strongly fluctuates. This kind of flow instability is very similar to that found in crossflow jets and is usually called as Kelvin-Helmholtz instability [21]. It induces three-dimensional complex vortex structures at the T-junction. The vortex structures for the LES-predicted flow field can be visualized using the iso-surface of second invariant of the velocity gradient tensor (usually called Q-value, see **Appendix B**). **Fig. 5-6** shows the iso-surface of Q=1000 and the temperature distribution on the walls of the lower half of the main pipe. The vortex structures indicated in **Fig. 5-6** are very similar to those demonstrated by Blanchard et al. [21]. Several arched vortices can be easily identified in the downstream mixing zone. Such arched vortex structures for similar crossflow jets were also reported by Fric et al. [20]. Also, close to the bottom wall of the main pipe and upstream of the branch jet exit, a reverse flow resulting from obstruction of the main pipe stream by the branch jet occurs and forms a horseshoe-shaped vortex structure around the jet injection location. Kelso & Smits [23] investigated such horseshoe-shaped vortex structure systems in detail. Particularly, periodical vortex-shedding in the wake of the branch jet occurs near the lower wall of the main pipe and, hence, leads to a nearby fluid temperature fluctuation, which is a cause of thermal fatigue.

In **Fig. 5-8**, the calculated results for the distribution of the normalized time-averaged axial velocity are compared with the experimental results. For clarity, the locations and direction of lines on the plot are indicated with pink arrowed lines in **Fig. 5-7**. **Fig. 5-8 (a)** and **Fig. 5-8 (b)** show the distributions of time-averaged axial velocity along the radial direction at $x=0.5D_m$ and $1.0D_m$, respectively. The profiles for calculated axial velocity mostly agree well with the experimental results, although there is a small discrepancy in the central part of the main pipe that is attributable to the relatively coarse grid in this part.

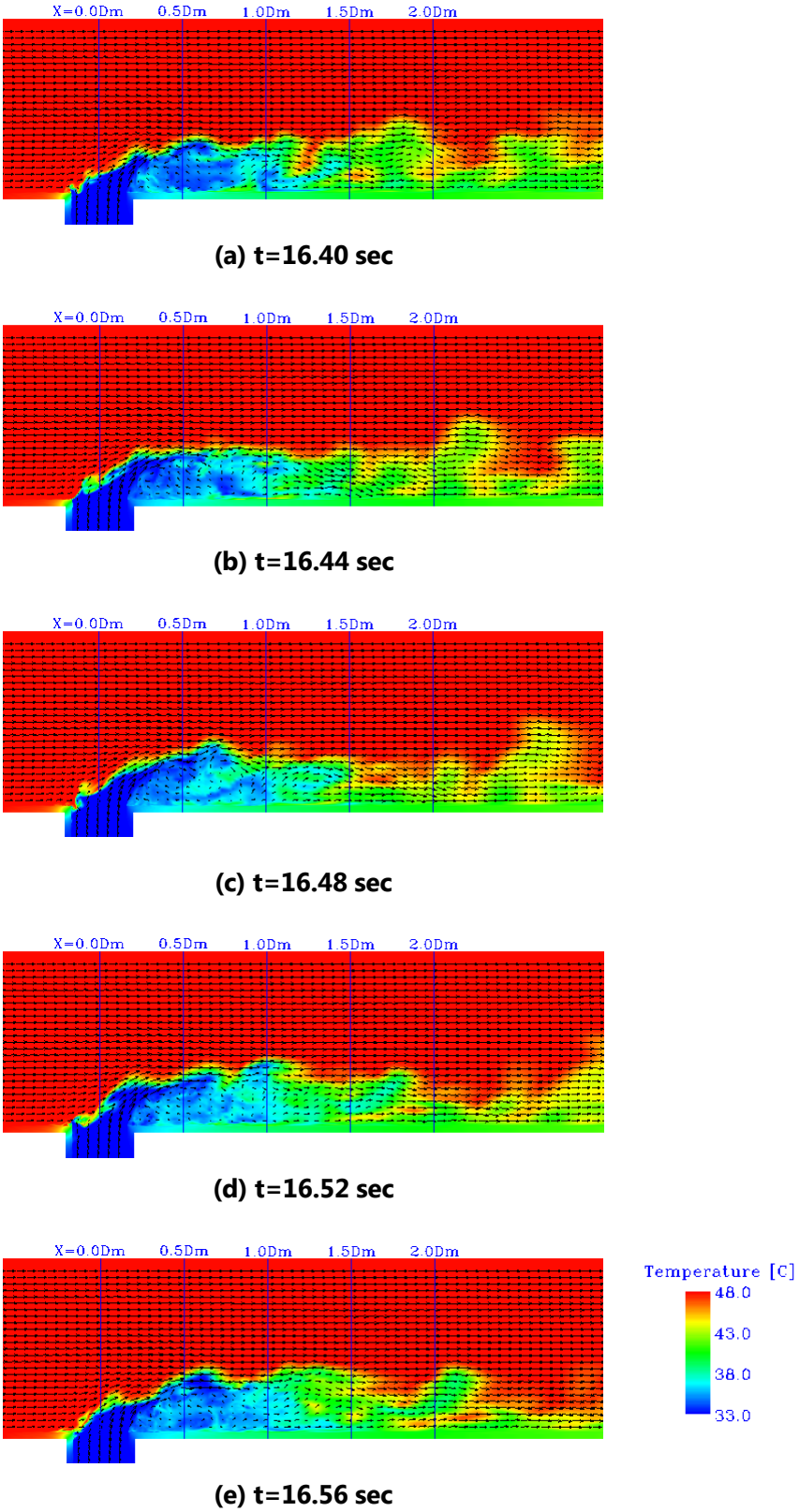

(a) t=16.40 sec

(b) t=16.44 sec

(c) t=16.48 sec

(d) t=16.52 sec

(e) t=16.56 sec

Fig. 5-5 Instantaneous Flow Velocity Vectors and Temperature Distribution on Vertical Cross-section along Flow Direction in Mixing Zone at 5 Time Steps

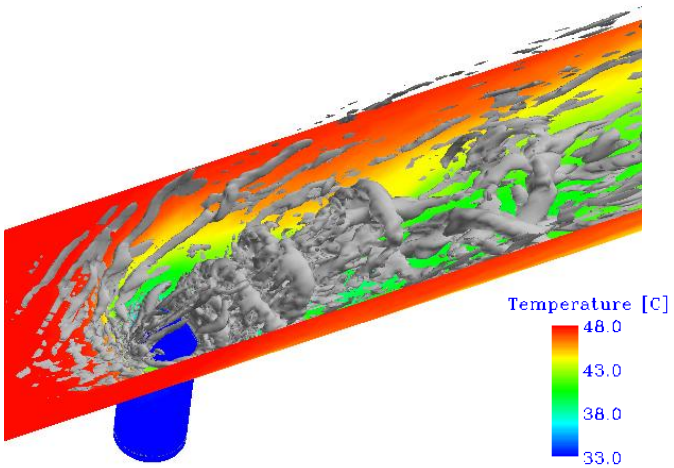

Fig. 5-6 Vortex Structures in the Mixing Zone at t=16.4 sec (Vortex: Iso-Surface of Q=1000; Contour: Wall Temperature)

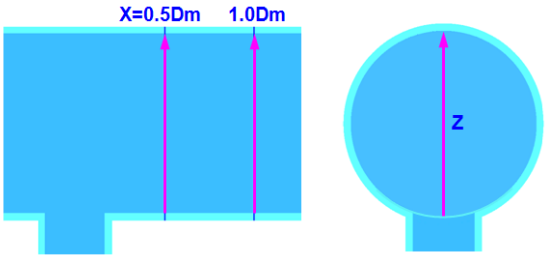

Fig. 5-7 Locations and Direction of the Lines (Pink) on Plot in Fig. 5-8, Fig. 5-10 and Fig. 5-11

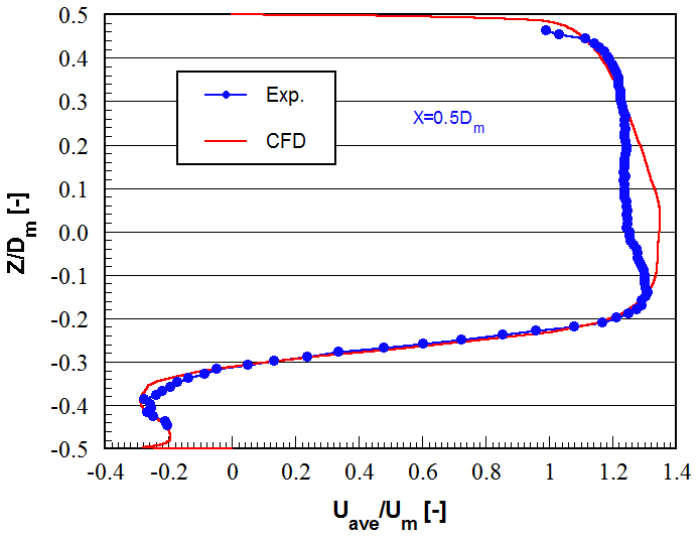

(a) X=0.5D_m

Fig. 5-8 Distribution of Normalized Time-Averaged Axial Velocity along the Radial Direction Shown in Fig. 5-7 (Continued on Next Page)

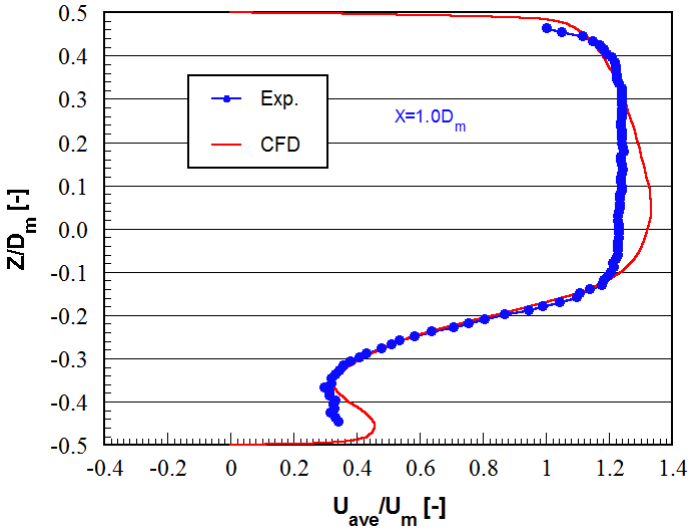

(b) X=1.0D_m

Fig. 5-8 (Continued from Previous Page)

5-5-2 Fluid Temperature and Its Fluctuation Intensity Distributions

The simulation results for the temperature fluctuation intensity distributions on the vertical cross-sections along and perpendicular to the flow direction are shown in **Fig. 5-9 (a)** and **(b)**, respectively. The temperature fluctuation intensity is defined as the normalized standard deviation of temperature with respect to time, as follows:

$$T_{rms}^{*} = \frac{1}{T_m - T_b}\sqrt{\sum_{i=1}^{N}(T_i - T_{ave})^2 / N} \qquad (5\text{-}9)$$

where T_m and T_b are the temperatures at the main and branch pipe inlets, respectively; T_i and T_{ave} the instantaneous temperature and time-averaged temperature, respectively, at the center of any mesh cell; and N is the number of sampling time-steps. The fluid temperature fluctuation intensity was obtained through a statistical calculation during a time period of 18 seconds (t=3~21 sec), based on Eq. (5-9). From the fluid temperature fluctuation intensity contours in **Fig. 5-9 (a)** and **(b)**, it is observed that the intensive temperature fluctuations take place at the interface between the hot and cold streams and are greatly attenuated beyond the distance of 2.0D_m from the center of the branch pipe. Particularly, it can be seen that strong temperature fluctuations are very close to the main pipe wall at the cross-sections of 0.0 D_m, 0.5 D_m and 1.0

D_m in **Fig. 5-9 (b)**. Hence, strong temperature fluctuations within the structure of the main pipe can be induced through the heat transfer between the fluid and the structure, and as a result, thermal fatigue may occur if the temperature fluctuations in the structure are sufficiently strong.

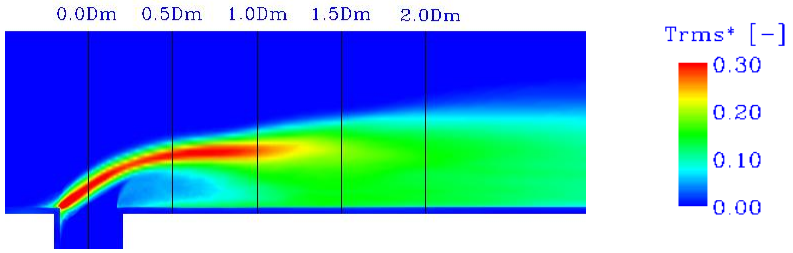

(a) Cross-section along the Flow Direction

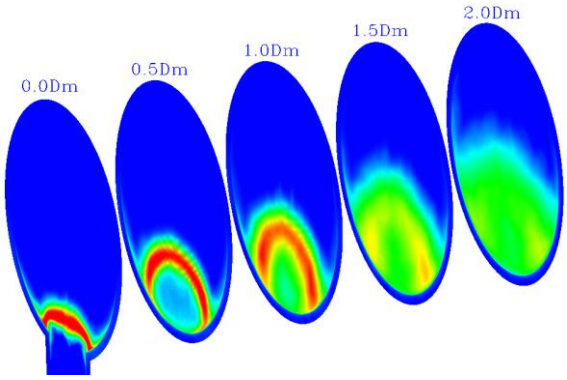

(b) Cross-sections Vertical to the Flow Direction

Fig. 5-9 Distribution of Normalized Temperature Fluctuation Intensity on the Cross-section along the Flow Direction in the Mixing Zone

In **Fig. 5-10**, the calculated results for the distribution of normalized time-averaged fluid temperature are compared with the experimental results. For clarity, the location and direction of lines on the plot are indicated with pink arrowed lines in **Fig. 5-7**. **Fig. 5-10** shows the distribution of normalized time-averaged fluid temperature along the radial direction at $x=0.5D_m$, as only the experimental data at this location are available. It can be seen that the distribution of LES-predicted fluid temperature agrees well with the experimental results.

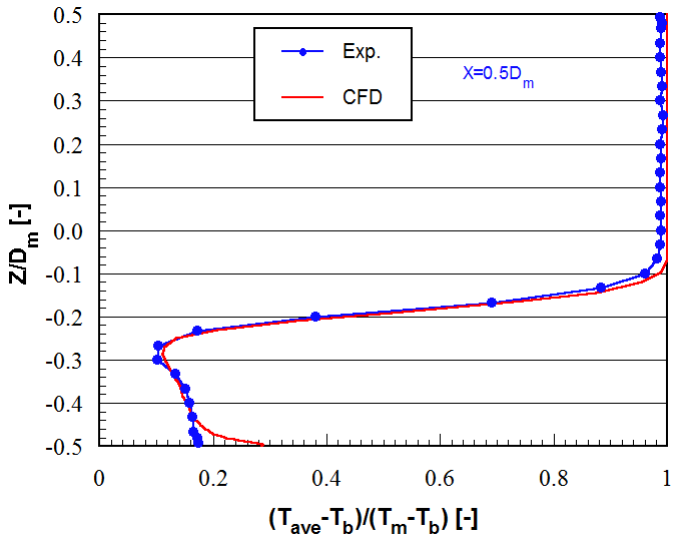

Fig. 5-10 Distribution of Normalized Time-Averaged Fluid Temperature along the Radial Direction Shown in Fig. 5-7

In **Fig. 5-11** and **Fig. 5-13**, the calculated results for the fluid temperature fluctuation intensity are compared with the experimental results. **Fig. 5-11** shows the distributions of normalized fluid temperature fluctuation intensity (TFI) along the radial direction at $x=0.5D_m$ and $1.0D_m$. For clarity, the locations and direction of the lines on the plot are indicated with the pink arrowed lines in **Fig. 5-7**. **Fig. 5-13** shows the distributions of TFI along the circumferential direction at $x=0.5D_m$ and $1.0D_m$. Similarly for clarity, the locations and direction of the lines on the plot are indicated with the pink lines and arrowed curve in **Fig. 5-12**. It can be observed from **Fig. 5-11** and **Fig. 5-13** that the LES-predicted TFI distributions are close to the experimental results for both the radial direction and the circumferential direction and, moreover, are a little conservative (or slightly larger than the experimental results). The slightly conservative prediction of TFI on the safe side is more desirable than an underestimation for the thermal fatigue evaluation.

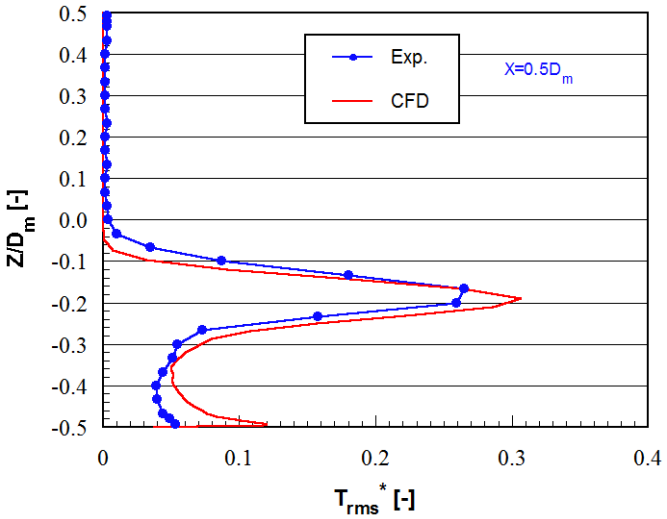

(a) X=0.5D_m

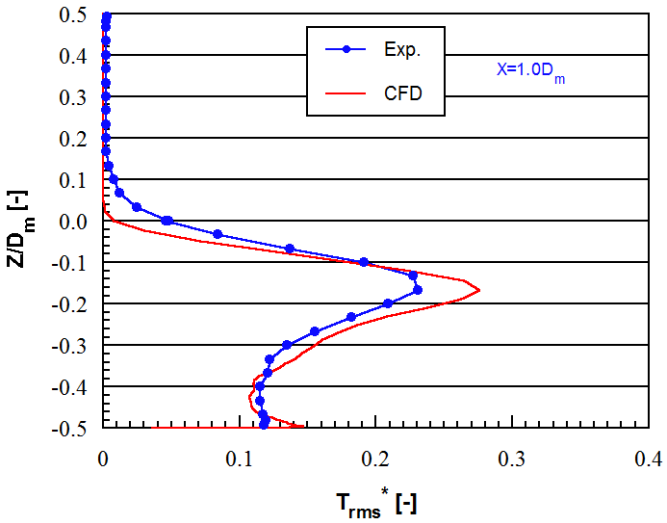

(b) X=1.0D_m

Fig. 5-11 Distribution of Fluid Temperature Fluctuation Intensity along the Radial Direction Shown in Fig. 5-7

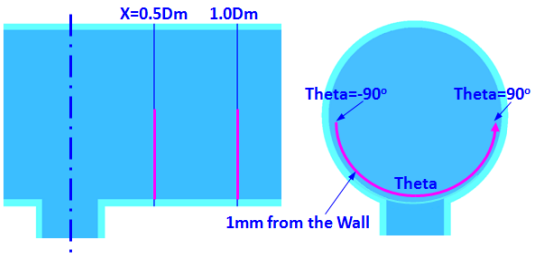

Fig. 5-12 Locations and Direction of the Lines (Pink) for the Plot in Fig. 5-13

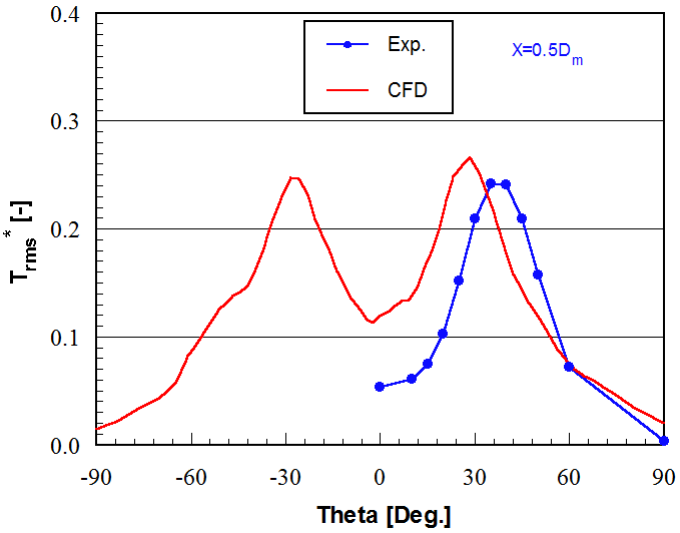

(a) X=0.5D_m

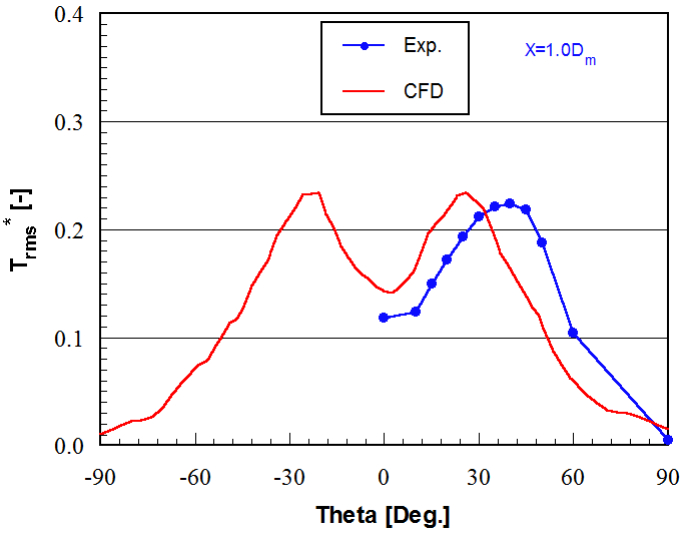

(b) X=1.0D_m

Fig. 5-13 Distribution of Normalized Fluid Temperature Fluctuation Intensity along the Circumferential Direction Shown in Fig. 5-12

5-5-3 Fluid and Structure Temperature Fluctuations

Fig. 5-14 compares the LES predictions and the experimental results for the temporal variation of fluid and structure temperatures at the sampling points. **Fig. 5-15** indicates the locations of two sampling points (pink points), which are located 1 mm away from the pipe wall for fluid side and 0.125 mm into the pipe wall for the structure side, respectively, with x=1.0D_m and at an angle of 30° from the vertical symmetrical plane. The total sampling time is 18.0

seconds, with a sampling time interval of 0.001 sec. However, only the data during 2.0 seconds are shown in **Fig. 5-14** for comparison with the experimental data. It can be seen that the amplitudes of LES-predicted fluid and structure temperature fluctuations shown in **Fig. 5-14(a)** are close to those in the experimental measurements in **Fig. 5-14(b)**.

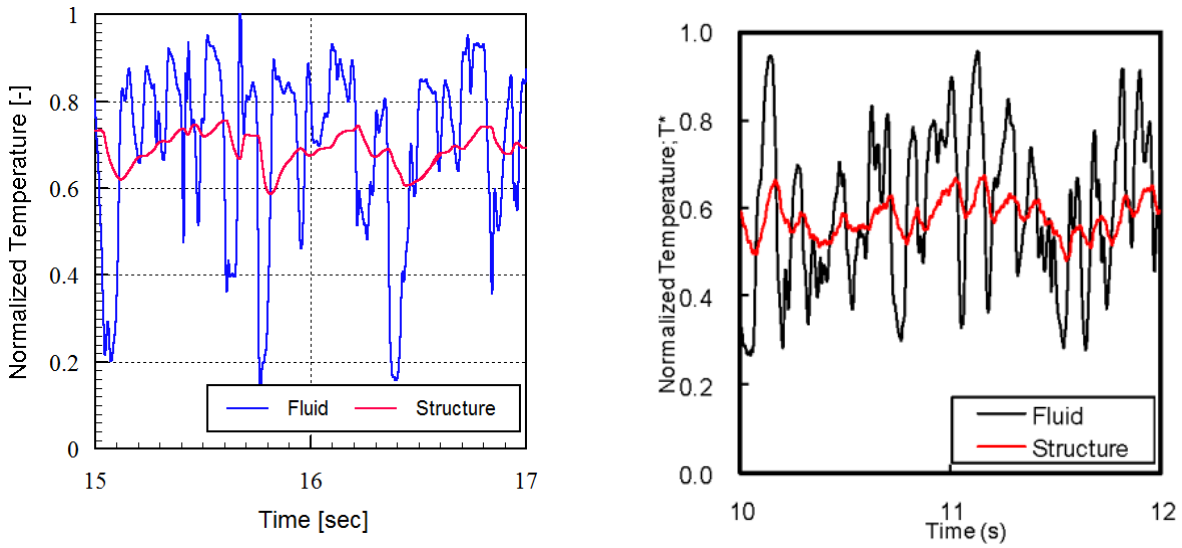

(a) CFD Results

(b) Experimental Results [87]

Fig. 5-14 Temporal Variation of Normalized Fluid and Structure Temperatures at Sampling Points Shown in Fig. 5-15

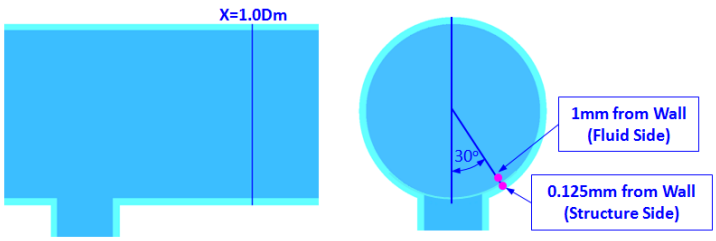

Fig. 5-15 Locations of Temperature Sampling Points

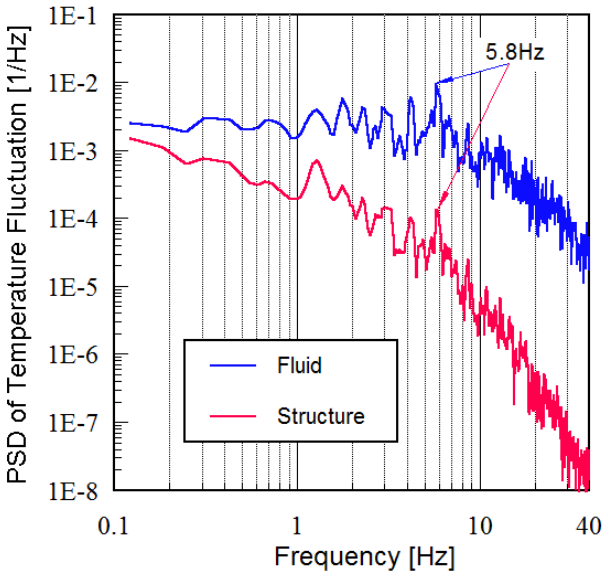

(a) CFD Results

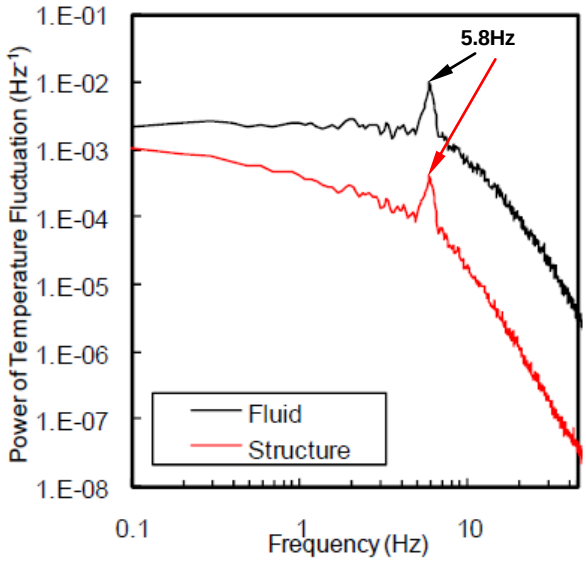

(b) Experimental Results [87]

Fig. 5-16 PSD of Normalized Fluid and Structure Temperatures Shown in Fig. 5-14

Fig. 5-16 (a) and **(b)** show the power spectrum density (PSD) obtained by a fast Fourier transform (FFT) of the time series of the fluid and structure temperatures in **Fig. 5-14** for the LES predictions and the experimental results, respectively. **Fig. 5-16 (a)** indicates that there exists a dominant peak at a frequency of 5.80 Hz for the PSD of both the fluid and structure temperatures predicted by LES simulation, which evidently agree well with the experimental results shown in **Fig. 5-16 (b)**. Igarashi et al. [74] found that the peak frequency for a T-junction

agreed well with the shedding frequency of a Karman vortex street in the wake of a cylinder with the same diameter as the branch jet. In addition, Kelso & Smits [23] also showed that the Strouhal numbers of the observed oscillating vortex systems for a circular jet in a crossflow, which has vortex structures similar to a T-junction, agree reasonably well with those appearing in the previous literature for wall-mounted circular cylinders. The shedding frequency f of Karman vortex can be normalized as a Strouhal number as follows:

$$St = fD_b / V_m \tag{5-10}$$

The Strouhal number of the vortex-shedding in the wake of a circular cylinder with a diameter of D_b can be nearly taken as $St = 0.2$ for $\mathrm{Re} = \rho_m V_m D_b / \mu_m = 9.64 \times 10^4$. As a result, the vortex-shedding frequency is evaluated as $f = 5.84Hz$ from Eq. (5-10). Obviously, the frequency (5.80 Hz) of the dominant peak of PSD shown in **Fig. 5-16** is very close to the value of 5.84 Hz estimated from Eq. (5-10). The results show that the vortex shedding frequencies in the wake are almost identical for the flows past a solid circular cylinder and a branch jet of the same diameter, although their flow fields, particularly the vortex structures, are remarkably different. This suggests that the numerical analysis predicted the frequency of vortex shedding around the branch jet well, and the PSD peak frequency of temperature fluctuations corresponds to the vortex shedding frequency in the wake of the branch jet.

5-6 Summary

Numerical methods for simulating fluid and structure temperature fluctuations at a T-junction were proposed and applied to evaluate thermal fatigue loading. The proposed numerical methods mainly included:

(1). Dynamic Smagorinsky model (DSM) for the LES SGS turbulence model

(2). Hybrid scheme with a large blending factor for calculation of the convective terms in the governing equations

(3). Direct calculation of heat transfer between a fluid and a structure through thermal conduction

(4). Creation of a very fine mesh for the structure region near inner wall of pipe and

(5) Coupled and simultaneous solution of energy equations for the fluid and structure regions in a fully implicit scheme

At the same time, a generalized estimation method of thickness of thermal boundary sub-layer was also proposed to ensure that all the near-wall grid points are surely located within thermal boundary sub-layer to calculate directly heat transfer between a fluid and a structure through thermal conduction. Then, the dimensionless thickness of thermal boundary sub-layer was estimated as $y_T^+ = 3.5$ for Pr=4.4 of the water used here, using such estimation method. The simulation results were compared with the experimental results to identify the prediction accuracy of thermal loading.

The simulation results show that the distributions of time-averaged flow velocity and fluid temperature predicted by LES simulation are remarkably close to the experimental results. Particularly, the distribution of fluid temperature fluctuation intensity and the range of structure temperature fluctuation are very close to the experimental results. Moreover, the predicted peak frequencies of power spectrum density (PSD) of both fluid and structure temperature fluctuations also agree well with the experimental results. As a result, it has been proven that the numerical methods (1)~(5) proposed here are of high accuracy. Therefore, as a guide, it is recommended that the high-accuracy numerical methods (1)~(5), as shown in **Table 5-4**, be applied for the prediction of structure temperature fluctuations, which is needed as the input of thermal stress FE analysis in thermal fatigue evaluation based on CFD/FEA coupling analysis.

Table 5-4 Numerical Methods Recommended for Evaluation of Thermal Loadings

LES Turbulence Model	Dynamic Smagorinsky SGS model (DSM)
Differencing Scheme for Calculation of Convective Term	Hybrid scheme with a blending factor as large as possible
Evaluation Approach for Heat Transfer between Fluid and Structure	● Direct calculation of heat transfer through thermal conduction by allocating the near-wall grid points within thermal boundary sub-layer ● Creation of a very fine mesh for the structure region near the inner wall of pipe ● Coupled and simultaneous solution of energy equations for the fluid and structure regions in a fully implicit scheme

Appendix 5-1 Preliminary Investigation of CFD Prediction Accuracy of Structure Temperature Fluctuations Using a Coarse Mesh and Wall Functions

As a preliminary investigation, LES simulation of fluid and structure temperature fluctuations at a T-junction was carried out using a coarse mesh and wall functions to confirm the prediction accuracy of structure temperature fluctuations. The mesh used for the simulation comprised a fluid region (pink part) and a structure region (blue part), as shown in **Fig. 5-17**. The mesh for the fluid region was relatively coarse. The near-wall cell size was uniformly 0.4992mm, which kept the dimensionless near-wall cell size $y^+ > 12$ for the mixing zone. On the other hand, a very fine mesh near the inner wall of pipe was generated for the structure region to reach the high prediction accuracy of the structure temperature fluctuations, as a coarse mesh may damp the near-wall structure temperature fluctuations. The near-wall cell size was uniformly 0.0562mm. The total number of cells in the mesh was about 1,266,000, which comprised about 846,000 cells in the fluid region and about 420,000 cells in the structure region.

The computational conditions used are the same as those shown in **Table 5-1** and **Table 5-2**, and numerical methods are the same as those shown in **Table 5-3**, except the calculation method of heat transfer between fluid and structure. The heat transfer coefficient between fluid and structure was evaluated using the wall function for the temperature field [141]. In addition, the

wall function for the flow field was also applied. The time step interval used was $\Delta t=0.0005$ sec.

The simulation results for the coarse mesh are compared with those for the fine mesh and the experiment measurement. **Fig. 5-18** shows the distributions of normalized fluid temperature fluctuation intensity (TFI) along the radial direction at $x=0.5D_m$ (see **Fig. 5-7** for the locations and direction of the lines on the plot). **Fig. 5-19** shows the TFI distributions along the circumferential direction at $x=0.5D_m$ (see **Fig. 5-12** for the locations and direction of the lines on the plot). It can be observed from **Fig. 5-18** and **Fig. 5-19** that the CFD TFI distributions predicted by the coarse mesh are close to the experimental results and the CFD results predicted by the fine mesh.

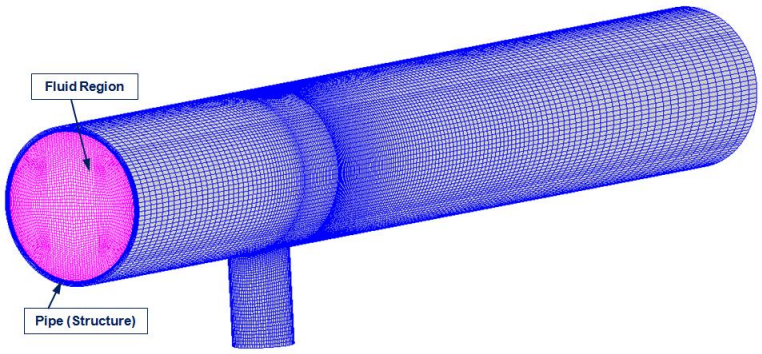

Fig. 5-17 Meshes for Computational Model

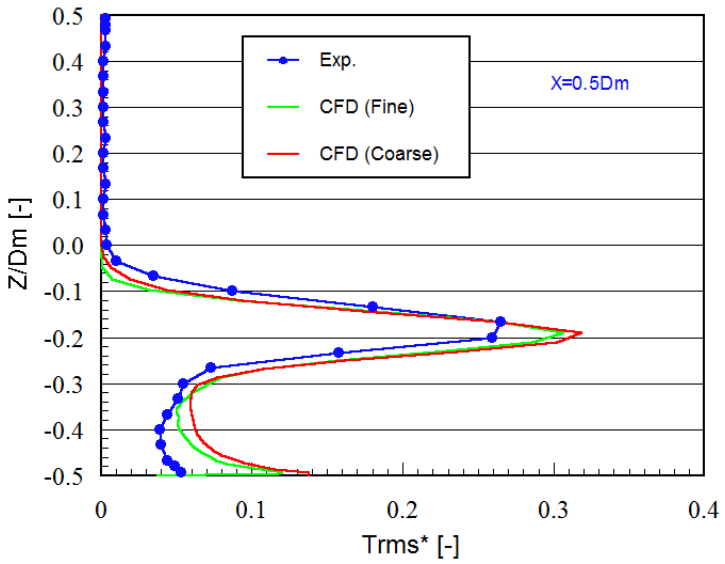

Fig. 5-18 Distribution of Fluid Temperature Fluctuation Intensity along the Radial Direction Shown in Fig. 5-7

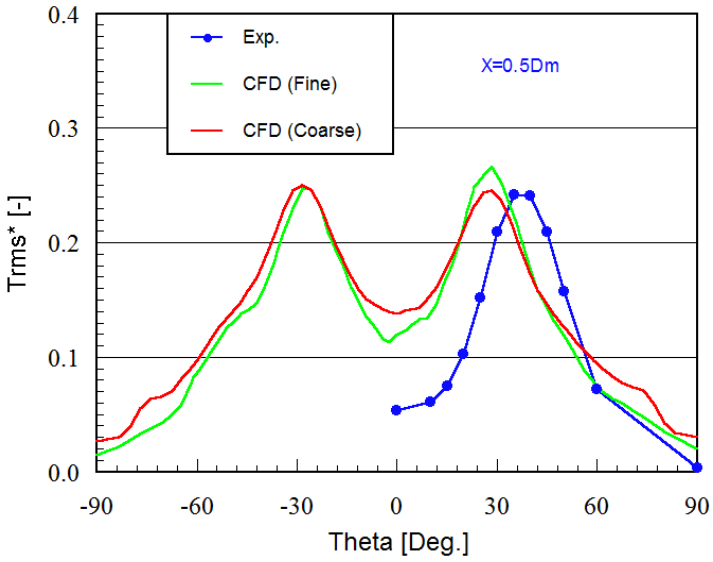

Fig. 5-19 Distribution of Normalized Fluid Temperature Fluctuation Intensity along the Circumferential Direction Shown in Fig. 5-12

Fig. 5-20 compares the LES predictions for the temporal variation of fluid and structure temperatures at the sampling points shown in **Fig. 5-15**, using the fine mesh (FM) and the coarse mesh (CM). It can be seen that the amplitudes of LES-predicted fluid temperature fluctuations for the coarse mesh are close to those for the fine mesh. However, the amplitudes of LES-predicted structure temperature fluctuations for the coarse mesh are remarkably smaller than those for the fine mesh and the experimental results shown in **Fig. 5-14 (b)**, and the former is about 55% of the latter two. This is probably because the wall functions largely under-evaluate the heat transfer coefficient between fluid and structure in the mixing zone, where the flow separation occurs.

Fig. 5-21 shows the power spectrum density (PSD) obtained by a fast Fourier transform (FFT) of the time series of the fluid and structure temperatures for the fine mesh (FM) and the coarse mesh (CM), as shown in **Fig. 5-20**. **Fig. 5-21** indicates that there exist the dominant peaks at a frequency of 5.8 Hz for the PSD of both the fluid and structure temperatures predicted by the fine mesh, and at a frequency of 6.0 Hz for those predicted by the coarse mesh. Their peak frequencies are very close.

In a summary, the amplitudes and frequencies of the fluid temperature fluctuations, as well as the frequencies of the structure temperature fluctuations could also be predicted with high accuracy, even using a relatively coarse mesh and the wall functions. However, the amplitudes of the structure temperature fluctuations were significantly under-predicted.

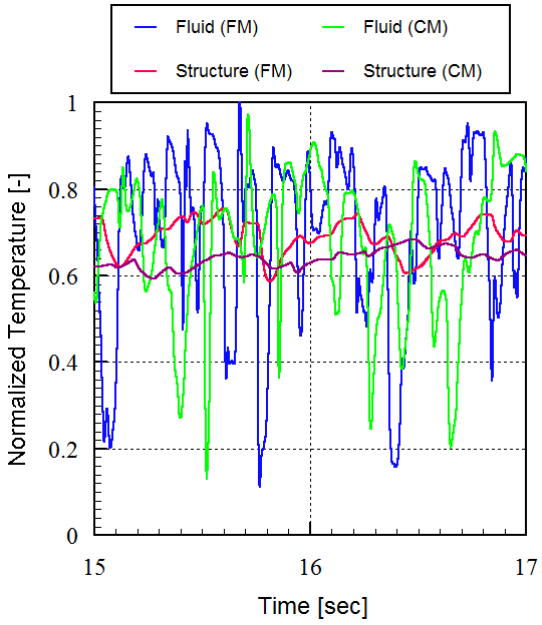

Fig. 5-20 Temporal Variation of Normalized Fluid and Structure Temperatures at Sampling Points Shown in Fig. 5-15

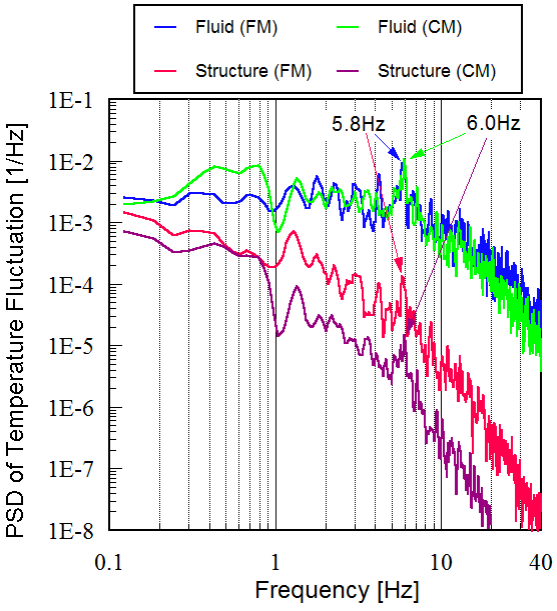

Fig. 5-21 PSD of Normalized Fluid and Structure Temperatures Shown in Fig. 5-20

Chapter 6 Proposal of Applications of the Research Results

6-1 Extension of Application Area of JSME S017

As described in Section 1.4 in **Chapter 1**, it is necessary to perform flow pattern classification to evaluate the attenuation factor of fluid temperature fluctuations and heat transfer coefficient in Step 2~4, when evaluating thermal loading using JSME S017. The conventional characteristic equations of flow pattern classification used in JSME S017 are only applicable to 90º tee junctions (T-junctions). However, angled tee junctions other than 90º (Y-junctions), are also used for mixing hot and cold fluids in process plants (such as petrochemical plants, refineries and LNG plants), although it seems that almost only 90º T-junctions are used in nuclear power plants. Therefore, it is essential to establish a generalized classification method of flow patterns applicable to both T-junctions and Y-junctions, in order to evaluate the structural integrity of Y-junctions by extending the conventional guideline JSME S017.

In **Chapter 3**, the generalized characteristic equations have been proposed to classify flow patterns for T-junctions and Y-junctions, and verified to be valid for flow pattern classification of tee junctions with branch angle of 30º ~ 90º by CFD simulations. As mentioned in **Chapter 3**, the Y-junctions with branch angle below 45º are not used in process plants, and hence, this applicable range of branch angle is sufficient for practical use. Therefore, applicable area of the conventional JSME S017 can be extended to T-junctions and Y-junctions for evaluation of the structural integrity in Step 2~4, by applying the generalized characteristic equations proposed for flow pattern classification.

6-2 Upgrade of JSME S017 and Direct Application of CFD/FEA Coupling Analysis to Thermal Fatigue Evaluation

As described above, JSME S017 was developed based on limited experimental data and a simplified one-dimensional FEA. As a result, there are the following issues to be solved:

- The accuracy of thermal fatigue evaluation based on JSME S017 is not high and especially the evaluation margin varies greatly from one case to another case [120].
- Its application is limited to the range where the experimental data were obtained.
- Dependence of thermal stress attenuation on the frequency of fluid temperature fluctuations was not considered in Step 4 of evaluation procedures in JSME S017.

In view of this, the high-accuracy CFD prediction methods of thermal loadings at a tee junction have been established through the systematic benchmark investigations in **Chapters 4** and **5**. The structure temperature fluctuations or thermal loadings predicted by CFD can be used as input of the FEA analysis of thermal stress. And then, time series of the obtained thermal stresses can be used for thermal fatigue evaluation. Therefore, it is expected that CFD/FEA coupling analysis is able to be used as numerical experiment for evaluating thermal fatigue with high accuracy.

The CFD/FEA coupling analysis can provide the high-accuracy prediction of thermal stress fluctuations in structure for more accurate evaluation of thermal fatigue. At the same time, a number of case studies (for example, for various different flow patterns and diameter ratios of branch pipe to main pipe) can be carried out. Therefore, it is expected that the CFD/FEA coupling analysis is able to be applied to the following two aspects:

- As shown in **Fig. 6-1**, the CFD/FEA coupling analysis can be used to upgrade Step 4 in JSME S017, instead of the experimental data used in Step 4 (see **Fig. 1-12** in **Chapter 1**).
- Moreover, as shown in **Fig. 6-2**, it can also directly be applied to perform a detailed evaluation (see **Fig. 1-12** in **Chapter 1**) of thermal fatigue for a specific case, after JSME S017 is used as an initial screening guideline and the evaluation cannot be passed.

As a result, the CFD/FEA coupling analysis will be able to enhance the accuracy of thermal fatigue evaluation and extend the application area of thermal fatigue evaluation and consider the dependence of thermal stress attenuation on the fluctuation frequency of fluid temperature.

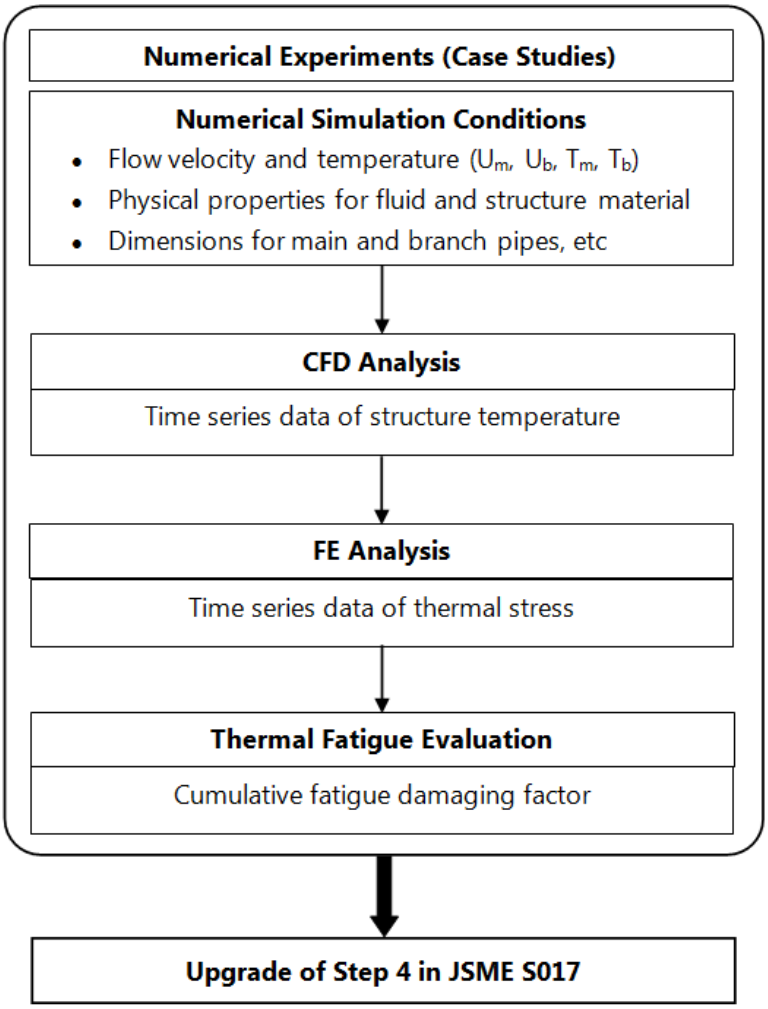

Fig. 6-1 Flow Chart for Upgrade of Step 4 in JSME S017

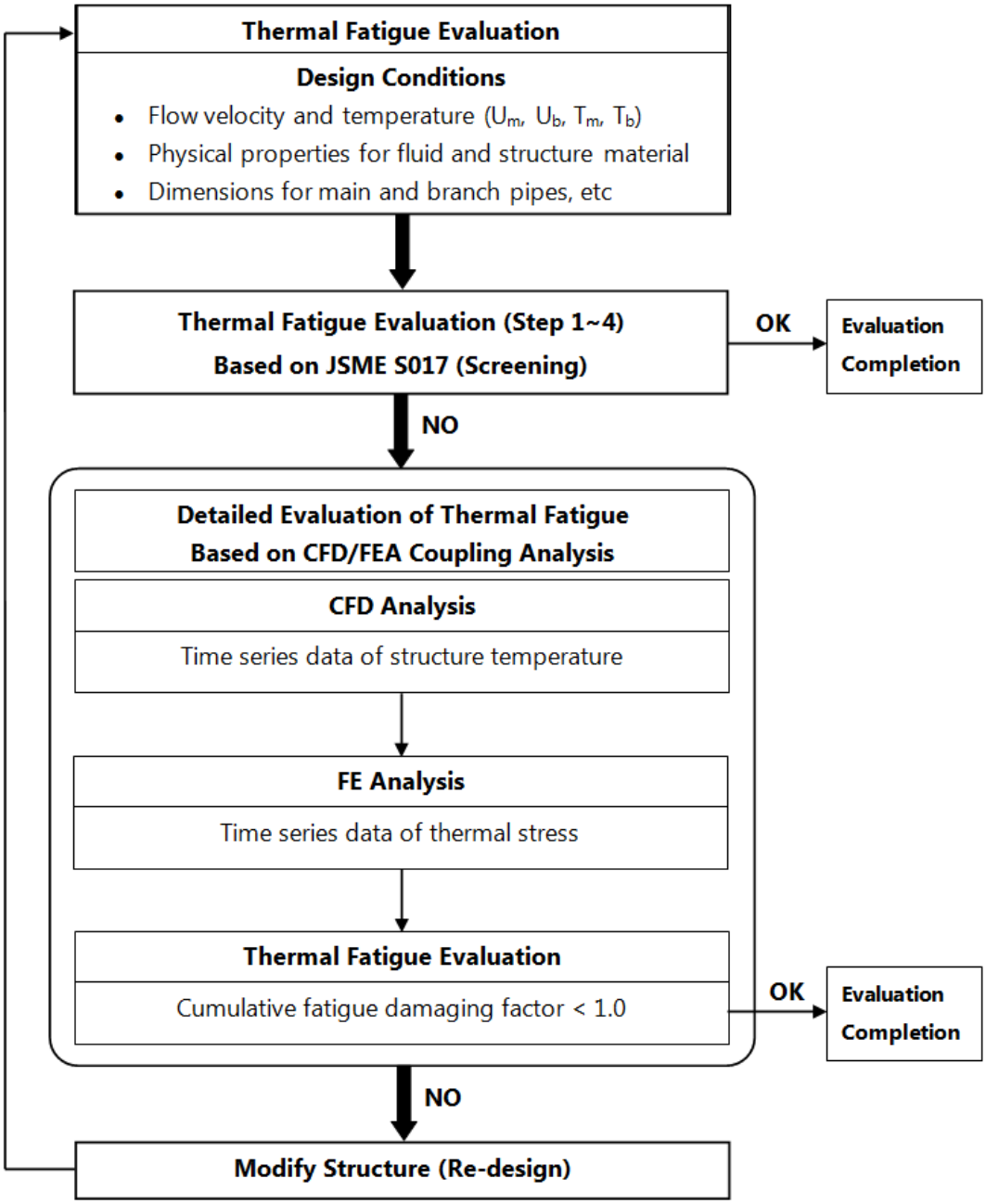

Fig. 6-2 Flow Chart for Thermal Fatigue Evaluation Based on JSME S017 and CFD/FEA Coupling Analysis

Chapter 7 Conclusions and Future Work

7-1 Conclusions

The aim of this study is to establish CFD prediction methods of thermal loadings at tee junctions for thermal fatigue evaluation. The following conclusions have been drawn.

In **Chapter 3**, the generalized characteristic equations were proposed to classify flow patterns for T-junctions and Y-junctions for evaluation of thermal loadings, by investigating the mechanism of the interaction of momentum between main and branch pipes. The proposed equations, which are Eqs.(3-7)~(3-9) in **Chapter 3** and shown again below, have been proven to be valid for predicting the flow patterns for T- and Y-junctions of 30° ~ 90°, which are sufficient for practical use in industrial plants, by CFD simulations of the flow and temperature fields.

$$M_m = D_m D_b \rho_m V_m^2 \tag{7-1}$$

$$M_b = \frac{\pi}{4} D_b^2 \rho_b V_b^2 \sin\alpha \tag{7-2}$$

$$M_R = M_m / M_b \tag{7-3}$$

In addition, the criteria shown in **Table 7-1**, which are identical to those currently used in JSME S017 and are on the safe side, are recommended for classification of the flow patterns at T- and Y-junctions of 30° ~ 90° when applying JSME S017 to evaluate thermal fatigue.

Table 7-1 Criteria Recommended for Flow Pattern Classification of T- and Y-junctions of 30° ~ 90°

Wall jet	$1.35 \leq M_R$
Deflecting jet	$0.35 < M_R < 1.35$
Impinging jet	$M_R \leq 0.35$

In **Chapter 4**, the scenario of LES benchmark simulations was proposed to establish the high-accuracy prediction methods of fluid temperature fluctuations, considering that the potentially over-evaluated turbulent eddy viscosity by LES turbulence models and numerical diffusion of differencing schemes may remarkably attenuate the predicted fluid temperature

fluctuations. The LES SGS turbulence models chosen were the standard Smagorinsky model (SSM) and the dynamic Smagorinsky model (DSM). The effects of the model parameter on the results were also investigated for the SSM model. Moreover, the effects of three differencing schemes for calculating the convective term in the energy equation were investigated as well. The LES benchmark simulation results were compared with the experimental ones to verify the prediction accuracy of fluid temperature fluctuations.

The simulation results showed that the turbulence model and differencing scheme had significant effects on the accuracy of the CFD simulations. The 1st-order upwind differencing scheme (1UD) significantly underestimates the fluid temperature fluctuation intensity (TFI) for the same LES sub-grid scale (SGS) model. However, the hybrid scheme, which is mainly the 2nd-order central differencing scheme (2CD) blended with a small fraction of 1UD, and the total variation diminishing (TVD) scheme can better predict the fluid TFI for each LES SGS model. For the LES SGS turbulence model, the DSM model gives a prediction closer to the experimental results than the SSM model, while using the same scheme. As a result, the approach using the DSM model and the hybrid scheme with a large blending factor or the TVD scheme could provide high-accuracy predictions of the fluid temperature fluctuations with a slight conservativeness.

In **Chapter 5**, based on the research results obtained in **Chapter 4**, numerical methods of predicting both fluid and structure temperature fluctuations at a T-junction were proposed and applied to perform the benchmark simulation for evaluating thermal fatigue loading. The proposed numerical methods mainly included:

(1). Dynamic Smagorinsky model (DSM) for the LES SGS turbulence model,

(2). Hybrid scheme with a large blending factor for calculation of the convective terms in the governing equations

(3). Direct calculation of heat transfer between a fluid and a structure through thermal conduction

(4). Creation of a very fine mesh for the structure region near inner wall of pipe

(5). Coupled and simultaneous solution of energy equations for the fluid and structure regions in a fully implicit scheme.

At the same time, a generalized estimation method of thickness of thermal boundary sub-layer was proposed to ensure that all the near-wall grid points are surely located within thermal boundary sub-layer for directly calculating heat transfer between a fluid and a structure through thermal conduction. Then, the dimensionless thickness of thermal boundary sub-layer was estimated as $y_T^+ = 3.5$ for Pr=4.4 of the water used here, based on such estimation method. The simulation results were compared with the experimental results to identify the prediction accuracy of thermal loading.

The simulation results showed that the distributions of time-averaged flow velocity and fluid temperature predicted by LES simulation are remarkably close to the experimental results. In particular, the predicted fluid TFI and range of structure temperature fluctuation are very close to the experimental results with a slight conservativeness. Moreover, the predicted peak frequencies of power spectrum density (PSD) of both fluid and structure temperature fluctuations also agree well with the experimental results. As a result, it has been proven that the proposed numerical methods (1)~(5) are capable of predicting thermal fatigue loading with a high accuracy and a slight conservativeness. Therefore, as a guide, it is recommended that the numerical methods (1)~(5), as shown in **Table 7-2**, be applied for the prediction of structure temperature fluctuations, which are used as the input of thermal stress FEA analysis in thermal fatigue evaluation based on CFD/FEA coupling analysis.

Table 7-2 Numerical Methods Recommended for Evaluation of Thermal Loadings

LES Turbulence Model	Dynamic Smagorinsky SGS model (DSM)
Differencing Scheme for Calculation of Convective Term	Hybrid scheme with a blending factor as large as possible
Evaluation Approach for Heat Transfer between Fluid and Structure	● Direct calculation of heat transfer through thermal conduction by allocating the near-wall grid points within thermal boundary sub-layer ● Creation of a very fine mesh for the structure region near the inner wall of pipe ● Coupled and simultaneous solution of energy equations for the fluid and structure regions in a fully implicit scheme

In **Chapter 6**, some applications of the outcomes obtained in this study were proposed, which are summarized as follows:

- The applicable range of conventional JSME S017 can be extended to all angles of tee junctions for evaluation of the structural integrity, by applying the generalized characteristic equations for flow pattern classification.
- Instead of experiment, case studies can be performed using CFD/FEA coupling analysis, and then, the simulation results obtained can be used to upgrade Step 4 in JSME S017.
- CFD/FEA coupling analysis can also be directly applied to evaluate thermal fatigue in combination with JSME S017, which is used as an initial screening guideline.

7-2 Future Work

To upgrade JSME S017, future work will focus on the following aspects:

- As a part of CFD/FEA coupling analysis, thermal stress FE analysis will be performed using the structure temperature data obtained in **Chapter 5**.
- Further, the thermal stress results will be used for thermal fatigue evaluation.
- Case studies for different flow patterns and diameter ratio of main pipe to branches will be performed using the numerical simulation methods verified in the present study, in order to upgrade JSME S017.

Appendix A: Main Features of Modified CFD Software FrontFlow/Red

In the present study, all the CFD simulations were performed using the modified multi-physics CFD software FrontFlow/Red, which was developed as a part of the Frontier Simulation Software for Industrial Science (FSIS) project funded by a grant from the Ministry of Education, Culture, Sport, Science and Technology of Japan. Its source code is open and available from a website [138].

Some modifications and customizations were added to the original source code of FrontFlow/Red to reach the strong thermal coupling between fluid and pipe and facilitate the output of simulation results for the present research. Specifically, an implicit numerical method for solving the energy equation was introduced when calculating the heat flux across the interface between fluid and structure (or pipe wall) in order to enhance the prediction accuracy of structure temperature fluctuation, which is very important for evaluation of thermal fatigue, and accelerate the convergence of the solution of energy equation as well. At the same time, a function capable of calculating and outputting the second invariant (usually called Q value, see **Appendix B**) of the velocity gradient tensor was added to the CFD code for visualizing the vortex structures of flow field.

In the modified FrontFlow/Red, the solution algorithm used is SIMPLE method [142]. The discretization of the governing equations is based on finite volume method (FVM) using co-located grid arrangement [123] and hence, the interpolation method proposed by Rhie and Chow [143] is adopted for calculating the pressure gradient to prevent pressure oscillation from occurring. In addition, the correction formula proposed by Muzaferija [144] is applied for enhancing the numerical differencing accuracy of diffusion term (or viscous term).

Appendix B: Equation for Calculating the Q-Value

The flow velocity gradient tensor can be written as:

$$D=\{d_{i,j}\}=\left\{\frac{\partial u_i}{\partial x_j}\right\}\quad (i=1,2,3;\ j=1,2,3) \tag{B-1}$$

The Q-value is the second invariant of above tensor and hence can be expressed as follows [145]:

$$\begin{aligned} Q(D)&=\frac{1}{2}\left\{[tr(D)]^2+tr(D^2)\right\}=\frac{1}{2}\left[(d_{i,i})^2-d_{i,j}d_{j,i}\right] \\ &=\frac{1}{2}\left[(\frac{\partial u_i}{\partial x_i})^2-\frac{\partial u_i}{\partial x_j}\frac{\partial u_j}{\partial x_i}\right] \end{aligned} \tag{B-2}$$

where $tr(D)$ is the trace of tensor D. $Q(D)$ is used for the visualization of vortex structures in the turbulent flow. $Q(D)>0$ stands for the vortex tube, and $Q(D)<0$ for the vortex sheet.

References

[1] Wood, D. S., “Proposal for design against thermal striping”, Nuclear Energy, 19, No. 6, 433-437 (1980).

[2] Brunings, J. E., “LMFBR thermal-striping evaluation”, Interim report, Research Project 1704-11, prepared by Rockwell International Energy Systems Group, 8900 De Soto Avenue, Canoga Park, CA, USA, 91304, EPRI-NP-2672, October, 1982.

[3] Betts, C., Bourman C. and Sheriff, N., “Thermal striping in liquid metal cooled fast breeder reactors”, 2nd Int. Topical Mtg. on Nuclear Reactor Thermal Hydraulics, NURETH-2, Santa Barbara, CA, USA, Vol. 2, 1292-1301 (1983).

[4] Moriya, S., Ushijima, S., Tanaka, N., Adachi, S. and Ohshima, I., “Prediction of thermal striping in reactors”, Int'l Conf. Fast Reactors and Related Fuel Cycles, Oct. 28- Nov. 1, Kyoto, Japan, Vol. 1, 10.6.1 -10.6.10 (1991).

[5] EPRI Report TR-103581, “Thermal stratification, cycling and striping (TASCS)”, March, 1994.

[6] Kasahara, N., Kawasaki, N., Kamide, H., Sakai, S. and Okajima, S., “Thermal fatigue evaluation method considering fluid-structure interaction against fluid temperature fluctuation”, Proceedings of the International Symposium on Research for Aging Management of Light Water Reactors, Oct. 22-23, 2007, Fukui City, Japan, 23-1~16 (2007).

[7] Chapuliot, S., Gourdin, C., Payen, T., Magnaud, J. P. and Monavon, A., “Hydro-thermal-mechanical analysis of thermal fatigue in a mixing tee”, Nuclear Engineering and Design, 235, 575-596 (2005).

[8] Lu, T., Jiang, P., Guo, Z., Zhang, Y and Li, H., “Large-eddy simulations (LES) of temperature fluctuations in a mixing tee with/without a porous medium”, International Journal of Heat and Mass Transfer, 53, 4458-4466 (2010).

[9] Shibamoto, H., Kasahara, N., Morishita, M., Inoue, K. and Jimbo, M., “Research and developments of guidelines for the thermal load modeling”, Nuclear Engineering and Design, 238, 299-309 (2008).

[10] Wakamatsu, M., Nei, H. and Hashiguchi, K. “Attenuation of temperature fluctuations in thermal striping”, J. Nucl. Sci. Tech., 32(8), 752-762 (1995).

[11] Jungclaus, D., Voswinkel, A. and Negri, P., “Common IPSN/GRS safety assessment of primary coolant unisolable leak incidents caused by stress cycling”, NEA/CSNI Specialist

Meeting on Experience with Thermal Fatigue in LWR Piping caused by Mixing and Stratification, OECD/NEA, Paris France, 7-12 June, 1998.

[12] Gelineau, O. and Sperandio, M., Martin, P. and Ricard, J.P., "Thermal fluctuation problems encountered in LMFBRs", Proc. IAEAIWGFR/90, Specialist meeting on correlation between material properties and thermo-hydraulics conditions in LMFBRs, Aix-en-Provence, France 22–24, 1994.

[13] Faidy, C., Courtois, T., Fraguier, E., Leduff, J., Lefrancois, A. and Dechelotte, J., "Thermal fatigue in French RHR system", Int. Conference on Fatigue of Reactor Components, Napa, CA (2000).

[14] Edited by Japan Nuclear Energy Safety Organization (JNES), "Troubles in the nuclear power plants in Japan", http://www.nsr.go.jp/archive/jnes/kouhou/anzen-pamphlet.html, (2003).

[15] Okuda, Y., "Analysis of thermal fatigue events in light water reactors", Nuclear Viewpoints, Vol.47, No.5, 60-64 (2001).

[16] Metzner, K. J. and Wilke, U., "European THERFAT project- thermal fatigue evaluation of piping system tee connections," Nuclear Engineering and Design, 235, 473-484 (2005).

[17] Maegawa, M., "Thermal fatigue of quench hydrogen piping", Proc. of 19th Symposium on the Maintenance of Equipments (The Japan Petroleum Institute), Tokyo, Japan, pp.12-17 (2006).

[18] Fukushima, N., Fukagata, K., Kasagi, N., Noguchi, H. and Tanimoto, K., "Numerical and experimental study on turbulent thermal mixing in a T-junction flow", The 6th ASME-JSME Thermal Engineering Joint Conference, March 16-20, TED-AJ03-582 (2003).

[19] Igarashi, M., Kamide, H., Tanaka, M. and Kimura, N., "Study on temperature fluctuation characteristics for high cycle thermal fatigue in a mixing tee", Trans. Japan Soc. Mech. Eng., B, Vol. 70, No. 700, 3150-3157 (2004).

[20] Fric, T. F. and Roshko, A., "Vortical structure in the wake of a transverse jet", Journal of Fluid Mechanics, Vol. 279, 1-47 (1994).

[21] Blanchard, J. N., Brunet, Y. and Merlen, A., "Influence of a counter rotating vortex pair on the stability of a jet in a cross flow: an experimental study by flow visualizations", Experiments in Fluids, Vol. 26, 63-74 (1999).

[22] Landman, M. J. and Saffman, P. G., "The three-dimensional instability of strained

vortices in a viscous fluid", Phys. Fluids, 30, 2339-2342 (1987).

[23] Kelso, R. M. and Smits, A. J., "Horseshoe vortex systems resulting from the interaction between a laminar boundary layer and a transverse jet", Phys. Fluids, 7 (1), 153-158 (1995).

[24] Yuan, L. L., Street, R. L., and Ferziger, J. H., "Large eddy simulations of a round jet in crossflow", J. Fluid Mech., 379, 71-104 (1999).

[25] Schluter, J. U. and Schonfeld, T., "LES of jets in cross flow and its application to a gas turbine burner", Flow, Turbulence and Combustion, 65, 177-203 (2000).

[26] Majander, P. and Siikonen, T., "Large-eddy simulation of a round jet in a cross-flow", Int. J. of Heat and Fluid Flow, 27, 402–415 (2006).

[27] Babu, P. and Mahesh, K., "Upstream entrainment in numerical simulations of spatially evolving round jets", Physics of Fluids, 16(10), 3699-3705 (2004).

[28] Muppidi, S. and Mahesh, K., "Study of trajectories of jets in crossflow using direct numerical simulations", J. Fluid Mech., Vol.530, 81-100 (2005).

[29] Muppidi, S. and Mahesh, K., "Direct numerical simulation of round turbulent jets in crossflow", J. Fluid Mech., Vol.574, 59-84 (2007).

[30] Sau, R. and Mahesh, K., "Dynamics and mixing of vortex rings in crossflow", J. Fluid Mech., Vol. 604, 389-409 (2008).

[31] Kasza, K.E. and Colwell, W.S., "Characterization of the temperature fluctuations generated mixing tee (sodium versus water behavior)", ANS/ASME Topical Meeting on Nuclear Reactor Thermal Hydraulics, Saratoga, USA, 1852-1870 (1980).

[32] Betts, C., Boorman, C. and Sheriff, N., "Thermal striping in liquid metal cooled fast breeder reactors", 2rd International Topical Meeting on Nuclear Reactor Thermal-Hydraulics, Santa Barbara, ANS. Vol. 2, 1292-1301 (1983).

[33] Wakamatsu, M., Ito, A. and Mawatari, K., "Comparison of sodium and water thermal striping in coaxial jets", IAHR Specialist Meeting, Sunnyvale, USA, Session IV-B (1983).

[34] Moriya, S. and Ohshima, I., "Hydraulic similarity in the temperature fluctuation phenomena of non-isothermal coaxial jets", Nuclear Engineering and Design, 120, 385-393 (1990).

[35] Tokuhiro, A. and Kimura, N., "An experimental investigation on thermal striping - Mixing phenomena of a vertical non-buoyant jet with two adjacent buoyant jets as measured by ultrasound Doppler velocimetry", Nuclear Engineering and Design, 188,

49-73 (1999).

[36] Tenchine, D. and Nam, H. Y., “Thermal hydraulics of co-axial sodium jets”, Am. Inst. Chem. Engrs. Symp. Ser. 83, No. 257, 151-156 (1987).

[37] Tenchine, D. and Moro, J. P., “Mixing of coaxial jets: Comparison of sodium and air experiments”, IAEA International Working Group on Fast Reactors, Specialist Meeting on Correlation Between Material Properties and Thermo-Hydraulics Conditions in LMFBRs, pp.1/16-6/16 (1994).

[38] Tenchine, D. and Moro, J. P., “Experimental and numerical study of coaxial jets”, NURETH-8, Kyoto, Japan, Vol. 3, 1381-1387 (1997).

[39] Tenchine, D. and Moro, J. P., “Experimental and computational study of turbulent mixing jets for nuclear reactors applications”, ISTP-12, 16-20 July, Istanbul, Turkey, 2000.

[40] Tenchine, D., “Some thermal hydraulic challenges in sodium cooled fast reactors”, Nuclear Engineering and Design, 240, 1195-1217 (2010).

[41] Kawasaki, N., Kobayashi, S., Hasebe, S. and Kasahara, N., “SPECTRA thermal fatigue tests under frequency controlled fluid temperature variation - transient temperature measurement tests -”, ASME, PVP2006-ICPVT11-93548 (2006).

[42] Oumaya, T., Nakamura, A. and Takenaka, N., “Approach to a method of integrated evaluation of thermal fatigue and its validation using SPECTRA”, J. of Power and Energy Systems, Vol.2, No.4, 1150-1165 (2008).

[43] Lejeail, Y. and Kasahara, N., “Thermal fatigue evaluation of cylinders and plates subjected to fluid temperature fluctuations”, International Journal of Fatigue, 27, 768–772 (2005).

[44] Fukuda, Y., Satoh, Y., Abe, H. and Madokoro, M., “Crack propagation and arrest behavior under thermal striping in liquid sodium”, J. Soc. Mat. Sci. Japan, Vol.43, No.295, 1591-1596 (1994).

[45] Muramatsu, T. and Ninokata, H., “Development of Analytical Method for Thermal Striping Phenomena”, Trans. Japan Soc. Mech. Eng., B, Vol. 57, No. 540, 2708-2715 (1991).

[46] Muramatsu, T., “Development of thermohydraulics computer programs for thermal striping phenomena”, Specialists meeting on correlation between material properties and thermohydraulics conditions in LMFRs, IAEA Working Group on Fast Reactors, IWGFR/90, Aix-en-Provence, France, November 22-24,1994.

[47] Muramatsu, T. and Ninikata, H., “Development of thermohydraulics computer programs for thermal striping phenomena”, Nuclear Technology, 113, 54–72 (1996).

[48] Muramatsu, T., “Numerical analysis of nonstationary thermal response characteristics for a fluid-structure interaction system”, Journal of Pressure Vessel Technology, Vol. 121, 276-282 (1999).

[49] Muramatsu, T., “Evaluation of thermal striping phenomena at a tee junction of LMFR piping system with numerical methods (1): Thermohydraulic Calculations”, SMiRT15, F05/6 (1999).

[50] Kasahara, N., “Evaluation of thermal striping phenomena at a tee junction of LMFR piping system with numerical methods (2): Thermomechanical Calculations”, SMiRT15, F05/5 (1999).

[51] Nishimura, M., Tokuhiro, A., Kimura, N. and Kamide, H., “Numerical study on mixing of oscillating quasi-planer jets with low Reynolds number turbulent stress and heat flux equation models”, Nuclear Engineering and Design, 202, 77-95 (2000).

[52] Nishimura, M., “Development of a low Reynolds number turbulence stress and heat flux equation model - A new type wall boundary condition for dissipation rate of turbulent kinetic energy aided by DNS data base”, ICONE-7, Apr. 20-22, Tokyo, Japan, ICONE-7106 (1999).

[53] Kimura, N., Nishimura, M. and Kamide, H., “Study on convective mixing for thermal striping phenomena”, JSME International Journal Series B, Fluids and Thermal Engineering, 45(3), 592-599 (2002).

[54] Choi, S.K. and Kim, S.O., “Evaluation of turbulence models for thermal striping in a triple jet”, ASME J. Pressure Vessel Technology, Vol. 129, 583-592 (2007).

[55] Velusamy, K., Natesan, K., Selvaraj, P., Chellapandi, P. and Chetal, S.C., “CFD studies in the prediction of thermal striping in an LMFBR”, Proceedings of the workshop on Benchmarking of CFD Codes for Application to Nuclear Reactor Safety (CFD4NRS), Munich, Germany, 5-7 September, 253-264 (2006).

[56] Moriya, S., “Prediction Methods of Metal Surface Temperature Fluctuation for Evaluation of High-Cycle Thermal Fatigue”, Trans. Japan Soc. Mech. Eng., B, Vol. 70, No. 694, 1547-1554 (2004).

[57] Jones, I.S. and Lewis, M.W.J., “A frequency response method for calculating stress intensity factors due to thermal striping loads”, Fatigue & Fracture of Engineering Materials & Structures, Vol. 17, 709-720 (1994).

[58] Jones, I.S. and Lewis, M.W.J., "The effect of various constraint conditions in the frequency response method of thermal striping", Fatigue & Fracture of Engineering Materials & Structures, Vol. 18, 489-502 (1995).

[59] Jones, I.S., "The frequency response model of thermal striping for cylindrical geometries", Fatigue & Fracture of Engineering Materials & Structures, Vol. 20, 871-882 (1997).

[60] Galvin, S. B. J., Graham, I. D., Jones, I. S. and Rothwell, G., "A comparison between the finite element and frequency response methods in the assessment of thermal striping damage", Int. J. Pressure Vessel & Piping, 74, 205-212 (1997).

[61] Jones, I.S. and Lewis, M.W.J., "An impulse response model for the prediction of thermal striping damage", Engineering Fracture Mechanics, Vol. 55, No. 5, 795-812 (1996).

[62] Jones, I. S., "Impulse Response Model of Thermal Striping for Hollow Cylindrical Geometries", Theoretical & Applied Fracture Mechanics, 43, 77–88 (2005).

[63] Jones, I. S., "Thermal striping fatigue damage in multiple edge-cracked geometries", Fatigue & Fracture of Engineering Materials & Structures, Vol. 29, 123-134 (2006).

[64] Kasahara, N., Yacumpai, A. and Takasho, H., "Structural response diagram approach for evaluation of thermal striping phenomenon", SMiRT15, F05/4 (1999)

[65] Kasahara, N., Takasho, H. and Yacumpai, A., "Structural response function approach for evaluation of thermal striping phenomena", Nuclear Engineering and Design, 212, 281-292 (2002).

[66] Kasahara, N. and Takasho, H., "Stress response functions to multi-dimensional spatial fluctuations of fluid temperature", ASME PVP, Vol. 443-1, 25-31 (2002).

[67] Kasahara, N., "Thermo-mechanical and fracture mechanics analysis on a tee junction of LMFR secondary circuit due to thermal striping phenomena", Final Report of a Coordinated Research Project (CRP), IAEA-TECDOC-1318, 89-116 (2002).

[68] Kasahara, N., "Frequency response function of structures to fluid temperature fluctuations", Proceedings of the Computational Mechanics Conference of JSME, Paper No.301 (2000).

[69] Meshii, T. and Watanabe, K., "Normalized stress intensity factor range solutions of an inner-surface circumferential crack in thin- to thick-walled cylinder under thermal striping by semi-analytical numerical method", Journal of Thermal Stresses, Vol. 27, No. 3, 253-267 (2004).

[70] Meshii, T. and Watanabe, K., "Stress intensity factor of a circumferential crack in a

thick-walled cylinder under thermal striping", Journal of Pressure Vessel Technology, Vol.126, 157-162 (2004).

[71] Lee, H.Y., Kim, J.B., Kim, S.H. and Yoo, B., "Evaluation of crack propagation under thermal striping load using Green's function approach", SMiRT-15, F06/1 (1999).

[72] Pasutto, T., Peniguel, C and Sakiz, M., "Chained computations using an unsteady 3D approach for the determination of thermal fatigue in a T-junction of a PWR nuclear plant", Nuclear Engineering and Technology, Vol.38, No.2, 147-154 (2006)

[73] Taheri, S., "Some Advances on Understanding of High Cycle Thermal Fatigue Crazing", ASME J. Pressure Vessel Technology, Vol. 129, 400-410 (2007).

[74] Igarashi M., Tanaka, M., Kawashima, M. and Kamide, H., "Experimental study on fluid mixing for evaluation of thermal striping in T-pipe junction", ICONE-10, ICONE10-2225 (2002).

[75] Anderson, U., Westin, J. and Eriksson, J., "Thermal mixing in a T-junction model tests", Report Number U 06:66, Vattenfall R&D AB, Alvkarleby, Sweden, pp.1-68 (2006).

[76] Zboray, R., Manera, A., Niceno, B. and Prasser, H.-M., "Investigations on mixing phenomena in single-phase flows in a T-junction geometry", NURETH-12, Paper No. 71 (2007).

[77] Smith, B. L., Hassan, Y., "CFD4NRS: Benchmarking of CFD Codes for Application to Nuclear Reactor Safety", Special Issue, Nuclear Engineering and Design, 238(3), 443-785 (2008).

[78] Smith, B. L., "Assessment of CFD Codes Used in Nuclear Reactor Safety Simulations", Nucl. Eng. Tech., Vol.42, No.4, 339-364 (2010).

[79] Igarashi, M., Tanaka, M., Kimura, N. and Kamide, H., "Study on fluid temperature fluctuation and transfer to wall in a mixing tee", ICONE-11, ICONE-36299 (2003).

[80] Kimura, N., Ogawa, H., Kamide, H., "Experimental study on fluid mixing phenomena in T-pipe junction with upstream elbow", Nuclear Engineering and Design, 240, 3055–3066 (2010).

[81] Tanaka, M., Oshima, H. and Monji, H., "Numerical simulation of thermal striping phenomena in a T-junction piping system using larger eddy simulation", J. of Power and Energy Systems, 3(1), 237-248 (2009).

[82] Tanaka, M., Oshima, H. and Monji, H., "Thermal Mixing in T-Junction Piping System Related to High-Cycle Thermal Fatigue in Structure", Journal of Nuclear Science and

Technology, Vol. 47, No. 9, 790–801 (2010).

[83] Kamide, H., Igarashi, M., Kawashima, S., Kimura, N. and Hayashi, K., “Study on mixing behavior in a tee piping and numerical analyses for evaluation of thermal striping”, Nuclear Engineering and Design, 239, 58–67 (2009).

[84] Kamaya, M. and Nakamura, A., “Thermal stress analysis for fatigue damage evaluation at a mixing tee”, Nuclear Engineering and Design, 241, 2674-2687 (2011).

[85] Miyoshi, K., Nakamura, A and Takenaka, N., "Numerical evaluation of wall temperature measurement method developed to estimate thermal stress at T-junction pipe", JSME Mechanical Engineering Journal, Vol.1, No.2, 1-14 (2014)

[86] Nakamura, A., Oumaya, T. and Takenaka, N., "Numerical investigation of thermal striping at a mixing tee using detached eddy simulation", The 13th International Topical Meeting on Nuclear Reactor Thermal Hydraulics (NURETH-13), N13P1074 (2009).

[87] Kimura, N., Ono, A., Miyakoshi, H. and Kamide, H., “Experimental study on high cycle thermal fatigue in T-junction – effect of local flow velocity on transfer of temperature fluctuation from fluid to structure”, NURETH-13, Kanazawa, Japan, N13P1169 (2009).

[88] Westin, J., Alavyoon, F., Andersson, L., Veber, P., Henriksson, M. and Andersson, C., “Experiments and unsteady CFD-calculations of thermal mixing in a T-junction”, Proc. Benchmarking of CFD Codes for Application to Nuclear Reactor Safety (CFD4NRS), Garching, Munich, Germany, 5-7 September, 2006.

[89] Westin J., Veber P., Andersson L., Mannetje C., Andersson U., Eriksson J., Hendriksson M., Alavyoon F. and Andersson C., “High-cycle thermal fatigue in mixing tees - large-eddy simulations compared to a new validation experiment”, ICONE16, ICONE16-48731 (2008).

[90] Jayaraju, S.T., Komen, E.M.J. and Baglietto, E., “Suitability of wall-functions in Large Eddy Simulation for thermal fatigue in a T-junction”, Nuclear Engineering and Design, 240, 2544–2554 (2010).

[91] Kuczaj, A.K., Komen, E.M.J. and Loginov, M.S., “Large Eddy Simulation study of turbulent mixing in a T-junction”, Nuclear Engineering and Design, 240, 2116–2122 (2010).

[92] Vreman, A.W., "An eddy-viscosity subgrid-scale model for turbulent shear flow: algebraic theory and applications", Phys. Fluids, 16(10), 3670-3681 (2004).

[93] Kim, J. and Jeong, J., “Large Eddy Simulation of a Turbulent Flow in a T-Junction”,

Numerical Heat Transfer, Part A: Vol. 61, Issue 3, 180-200 (2012).

[94] Obabko, A.V., Fischer, P.F., Tautges, T.J., Karabasov, S., Goloviznin, V.M., Zaytsev, M.A., Chudanov, V.V., Pervichko, V.A. and Aksenova, A.E., "CFD validation in OECD/NEA T-junction benchmark", ANL/NE11/25 (2011)

[95] Ayhan H. and Sökmen C. N., "CFD Modeling of Thermal Mixing in a T-junction Geometry Using LES Model", Nuclear Engineering and Design, 253, 183-191 (2012).

[96] Hohne, T., "Scale resolved simulations of the OECD/NEA Vattenfall T-junction benchmark", Nuclear Engineering and Design, 269, 149-154 (2014).

[97] Walker, C., Simiano, M., Zboray, R. and Prasser, H.-M., "Investigations on mixing phenomena in single-phase flow in a T-junction geometry", Nuclear Engineering and Design, 239(1), 116-126 (2009).

[98] Manera, A., Prasser, H.-M., Lechner, R. and Frank, T., "Toward the prediction of Temperature Fluctuations by means of Steady RANS for the Estimation of Thermal Fatigue", NURETH-13, N13P1110 (2009).

[99] Frank, T., Lifante, C., Prasser, H. M. and Menter, F., "Simulation of turbulent and thermal mixing in T-junctions using URANS and scale-resolving turbulence models in ANSYS CFX", Nuclear Engineering and Design, 240, 2313–2328 (2010).

[100] Li, C., Tsai, Y., Tsai, T. and Wang, L., "Two different turbulence models in comparison with experiments on thermal mixing phenomenon in a tee piping", WSEAS Transactions on Fluid Mechanics, Issue 2, Vol.5, 45-54 (2010).

[101] Tanaka, M., Kurokawa, K., Takita, H. and Monji, H., "Experimental Study on Thermal Mixing Related to Eddy Structure in T −Junction", Trans. Japan Soc. Mech. Eng., B, Vol. 76, No. 763, 101-103 (2010)

[102] Tanaka, M., Kurokawa, K., Takita, H., Monji, H. and Ohshima, H., "Numerical Investigation on Thermal Mixing Related to Eddy Structure in T-Junction", Trans. Japan Soc. Mech. Eng., B, Vol. 77, No. 776, 60-64 (2011)

[103] Tanaka, M., Takita, H., Monji, H. and Ohshima, H., "Investigation on Fluid-Structure Thermal Interaction Related to Eddy Structure on Branch Jet in T-Junction", Trans. Japan Soc. Mech. Eng., B, Vol. 78, No. 792, 113-116 (2012).

[104] Tanaka, M., "Investigation of V&V process for thermal fatigue issue in a sodium cooled fast reactor - Application of uncertainty quantification scheme in verification and validation with fluid-structure thermal interaction problem in T-junction piping system",

Nuclear Engineering and Design, Vol. 279, Pages 91-103 (2014)

[105] Takahashi, S., Shiina, K., “Characteristics of Fluid Temperature Fluctuation in a Mixing Tee Pipe with Hot and Cold Water Flows”, Trans. Japan Soc. Mech. Eng., B, Vol. 66, No. 651, 2905-2911 (2000).

[106] Hibara, H., Iwamoto, Y., Sogo, M and Ochi, J., “Elucidation of fluid vibration phenomenon causing thermal striping of T-junction piping system”, Annual Journal of Engineering, Ehime University, Vol. 4, 21-27 (2005).

[107] Shigeta, A., Nakamori, K., Senda, M. and Inaoka, K., “Thermal and hydraulic characteristics in a mixing tee pipe with fluid temperature fluctuation”, The Science and Engineering Review of Doshisha University, Vol. 49, No. 2, 51-57 (2008).

[108] Kuhn, S., Braillard, O., Niceno, B. and Prasser, H.M., “Computational study of conjugate heat transfer in T-junctions”, Nuclear Engineering and Design, 240, 1548-1557 (2010).

[109] Hu, L., and Kazimi, M.S., “LES benchmark study of high cycle temperature fluctuations caused by thermal striping in a mixing tee”, Int. J. of Heat and Fluid Flow, 27, 54-64 (2006).

[110] Lee, J.K., Hu, L., Saha, P., and Kazimi, M.S., “Numerical analysis of thermal striping induced high cycle thermal fatigue in a mixing tee”, Nuclear Engineering and Design, 239, 833–839 (2009).

[111] Wakamatsu, M., Hirayama, H., Kimura, K., et al., “Study on high-cycle fatigue evaluation for thermal striping in mixing tees with hot and cold water (1)”, ICONE-11, Tokyo, Japan, ICONE11-36208 (2003).

[112] Hosseini, S.M., Yuki, K., and Hashizume, H., “Classification of turbulent jets in a T-junction area with a 90-deg bend upstream”, Int. J. of Heat and Mass Transfer, 51, 2444-2454 (2008).

[113] Oka, K., and Ito, H., “Energy loss at tees with large area ratios”, Transactions of the ASME, 127, 110-116 (2005).

[114] Fukuda, T., Sakashita, A., Mizutani, J., Matsunaga, T., Ogura, K., Shiina, K., Tanimoto, K., Moriya, S. and Madarame, H., “Current effort to establish a JSME code for the evaluation of high-cycle thermal fatigue”, ICONE11, Tokyo, Japan, April 20–23 (2003).

[115] Wakamatsu, M., Hirayama, H., Kimura, K., Ogura, K., Shiina, K., Tanimoto, K., Mizutani, J., Minami, Y., Moriya, S. and Madarame, H., “Study on high-cycle fatigue evaluation for thermal striping in mixing tees with hot and cold water (1)”, ICONE11,

Tokyo, Japan, ICONE11-36208 (2003).

[116] Kawamura, T., Shiina, K., Ohtsuka, M., Mizuno, T., Kurosaki, M., Ogura, K., Tanimoto, K., Fukuda, T., Minami, Y., Moriya, S. and Madarame, H., "Thermal striping tests in mixing tees with same pipe diameters (1), characteristics of flow patterns and fluid temperature fluctuations", Trans. Japan Soc. Mech. Eng., B, Vol. 69, No. 682, 1445-1452 (2003).

[117] Kawamura, T., Shiina, K., Ohtsuka, M., Mizuno, T., Kurosaki, M., Ogura, K., Tanimoto, K., Fukuda, T., Minami, Y., Moriya, S. and Madarame, H., "Thermal striping tests in mixing tees with same pipe diameters (2), characteristics of heat transfer of temperature fluctuations", Trans. Japan Soc. Mech. Eng., B, Vol. 70, No. 696, 2083-2088 (2004).

[118] Kasahara, N., Furuhashi, I. and Takasho, H., "Crack propagation of structures against fluid temperature fluctuations", JSME M&M Conference 2003, No.03-11, 395-396 (2003).

[119] The Japan Society of Mechanical Engineers (JSME), "Guideline for Evaluation of High-Cycle Thermal Fatigue of a Pipe" (in Japanese), JSME S017 (2003).

[120] Suzuki, T. and Kasahara, N., "Thermal fatigue evaluation method of pipes by equivalent stress amplitude", ASME PVP2012, PVP2012-78347 (2012).

[121] Kasahara, N., Itoh, T., Okazaki, M., Okuda, Y., Kamaya, M., Nakamura, A., Nakamura, H., Machida, H., and Matsumoto, M., "Development of thermal fatigue evaluation methods of piping systems", E-Journal of Advanced Maintenance, Vol.6, No.1, 14-23 (2014).

[122] Nakamura, A., Utanohara, Y., Miyoshi, K. and Kasahara, N., "A review of evaluation methods developed for numerical simulation of the temperature fluctuation contributing to thermal fatigue of a T-junction pipe", E-Journal of Advanced Maintenance, Vol.6, No.4, 118-130 (2015).

[123] Ferziger, J.H. and Peric, M., "Computational Methods for Fluid Dynamics (3rd Edition)", Springer-Verlag Berlin Heidelberg GmbH, ISBN 978-3-540-42074-3 (2002).

[124] Bardina, J., Ferziger, J.H. and Reynolds, W.C., "Improved subgrid models for large eddy simulation", AIAA paper 80-1357 (1980).

[125] Miyata, H. (Ed.), "Analysis of Turbulent Flows (Computational Fluid Dynamics Series 3)", The University of Tokyo Press, ISBN4-13-065103-X (1995).

[126] Hinze, J.O., "Turbulence", McGraw-Hill Publishing Co., New York, 1975.

[127] Launder, B.E. and Spalding, D.B., "Mathematical Models of Turbulence", Academic

Press, London, England, 1972.

[128] Launder, B.E. and Spalding, D.B., "The numerical computation of turbulent flows", Comp. Meth. Appl. Mech. Eng., 3, 269-289 (1974).

[129] Shih, T.H., Liou, W.W., Shabbir, A. Yang, Z. and Zhu, J., "A new $k-\varepsilon$ eddy-viscosity model for high Reynolds number turbulent flows - model development and validation", Computers Fluids, 24(3), 227-238 (1995).

[130] Kim, S.E., Choudhury, D. and Patel, B., "Computations of complex turbulent flows using the commercial code ANSYS FLUENT", Proceedings of the ICASE/LaRC/AFOSR Symposium on Modeling Complex Turbulent Flows, Hampton, Virginia, Kluwer Academic Publishers, pp.259-276 (1997).

[131] Roy, S. and Saha, U.K., "Computational study to assess the influence of overlap ratio on static torque characteristics of a vertical axis wind turbine", Procedia Engineering, 51, 694–702 (2013).

[132] Smagorinsky, J., "General circulation experiments with the primitive equations, Part 1: the basic experiment", Mon. Weather Rev., 91, 99-164 (1963).

[133] Germano, M., Piomelli, U., Moin, P. and Cabot, W. H., "A dynamic sub-grid scale eddy viscosity model", Physics of Fluids, A, 3, 1760-1765 (1991).

[134] Lilly, D. K., "A proposed modification of the Germano subgrid-scale closure method", Phys. Fluids A, 4, 633-635 (1992).

[135] Kawamura, T., Kawahara, M., Hirano, H., Tosaka, N. and Ikegawa, M., "Analysis of Incompressible Flows", The University of Tokyo Press, Japan, ISBN 4-1306510-1-3 (1995).

[136] Kobayashi, T. (Ed.), "Numerical Simulations Using CFD Software Advance/FrontFlow/Red" (in Japanese), ISBN 4-9902143-3-1 (2004).

[137] De Chant, L.J., "The venerable 1/7th power law turbulent velocity profile: a classical nonlinear boundary value problem solution and its relationship to stochastic processes", Applied Mathematics and Computation, **161**(2), 463-474 (2005).

[138] Frontier Simulation Software for Industrial Science, http://www.ciss.iis.u-tokyo.ac.jp /fsis/en /index.html

[139] Nakamura, A., Utanohara, Y. and Miyoshi, K., "Effects of mesh and inlet boundary conditions on CFD for thermal load evaluation", Proceedings of the JSME 2013 Annual Meeting, Okayama, Japan, J032011 (2013).

[140] Nakamura, A., Ikeda, H., Qian, S., Tanaka, M. and Kasahara, N., "Benchmark simulation of temperature fluctuation using CFD for the evaluation of the thermal load in a T-junction pipe", Proc. of the 7th Korea-Japan Symposium on Nuclear Thermal Hydraulics and Safety (NTHAS-7), Chuncheon, Korea, N7P-0011 (2010).

[141] Bredberg, J., Peng, S., Davidson, L., "On the wall boundary condition for computing turbulent heat transfer with $k-\varpi$ models", Proc. of the ASME Heat Transfer Division Conference, Orlando, FL, HTD-Vol. 366-5 (2000).

[142] Patankar, S. V., "Numerical Heat Transfer and Fluid Flow", Taylor & Francis, ISBN 978-0-89116-522-4 (1980).

[143] Rhie, C.M., Chow, W.L., "Numerical study of the turbulent flow past an airfoil with trailing edge separation", AIAA Journal, 21, 1525–1532 (1983).

[144] Muzaferija, S., "Adaptive finite volume method for flow predictions using unstructured meshes and multi-grid approach", PhD Thesis, University of London (1994).

[145] Chakrabotry, P., Balachandar, S. and Adrian R.J., "On the relationships between local vortex identification schemes", J. Fluid Mech., Vol. 535, 189-214 (2005).

Publication List

- Peer-Reviewed Journal Papers

1. Qian, S. and Kasahara, N.: "LES Analysis of Temperature Fluctuations at T-Junctions for Prediction of Thermal Loading", **ASME Journal of Pressure Vessel Technology**, 137(1), 011303, doi:10.1115/1.4028067 (2015).
2. Qian, S., Frith, J. and Kasahara, N.: "Classification of Flow Patterns in Angled T-Junctions for the Evaluation of High Cycle Thermal Fatigue", **ASME Journal of Pressure Vessel Technology**, 137(2), 021301, doi:10.1115/1.4027903 (2015).
3. Qian, S., Kanamaru, S. and Kasahara, N.: "High-Accuracy Analysis Methods of Fluid and Structure Temperature Fluctuations at T-junction for Thermal Fatigue Evaluation", **Nuclear Engineering & Design (Elsevier)**, Vol. 288, pp.98-109, doi:10.1016/j.nucengdes. 2015. 04.006 (2015).

- Peer-Reviewed International Conference Papers

1. Qian, S., S. Kanamaru and N. Kasahara: "High-Accuracy Analysis Methods of Fluid and Structure Temperature Fluctuations at T-junction for Thermal Fatigue Evaluation", **Proceedings of the ASME 2012 Pressure Vessels & Piping Division Conference,** July 15~19, 2012, Toronto, Ontario, CANADA, PVP2012-78159 (2012).
2. Qian, S. and N. Kasahara: "LES Analysis of Temperature Fluctuations at T-Junctions for Prediction of Thermal Loading", **Proceedings of the ASME 2011 Pressure Vessels & Piping Division Conference,** July 17~21, 2011, Baltimore, MD, USA, PVP2011-57292 (2011). (**ASME PVP Division Outstanding FSI Technical Paper Award**)
3. Qian, S., J. Frith and N. Kasahara: "Classification of Flow Patterns in Angled T-Junctions for the Evaluation of High Cycle Thermal Fatigue", **Proceedings of the ASME 2010 Pressure Vessels & Piping Division/K-PVP Conference,** July 18~22, 2010, Bellevue, WA, USA, PVP2010-25611 (2010).
4. Nakamura, A., H. Ikeda, S. Qian, M. Tanaka and N. Kasahara: "Benchmark Simulation of Temperature Fluctuation Using CFD for the Evaluation of the Thermal Load in a T-Junction Pipe", **Proceedings of the 7th Korea-Japan Symposium on Nuclear Thermal Hydraulics and Safety (NTHAS-7)**, Nov. 14~17, Chuncheon, Korea, N7P-0011 (2010).

- Domestic Conference Papers

1. Qian, S., S. Kanamaru and N. Kasahara: "High-Accuracy Analysis Methods of Fluid and Structure Temperature Fluctuations at T-junction for Thermal Fatigue Evaluation", **Proceedings of the JSME 2013 Annual Meeting,** September, 2013, Okayama, Japan (2013).
2. Qian, S., S. Kanamaru and N. Kasahara: "LES Analysis of Fluid and Structure Temperature Fluctuations at T-junction for Thermal Fatigue Evaluation", **Proceedings of the 78th Annual Meeting of the Society of Chemical Engineers of Japan**, March, 2013, Osaka, Japan (2013).
3 Nakamura, H., H. Kawahara, B. Li, S. Qian, M. Suzuki and N. Kasahara: "CFD Predictions of Thermal Striping at Piping Junction", **Proceedings of the 17th Conference of The Japan Society for Computational Engineering & Science, Vol.17**, May, 2012, Kyoto, Japan.
4 Nakamura, A., S. Qian, M. Tanaka and N. Kasahara: "Benchmark Simulation of Temperature Fluctuation Using CFD for the Evaluation of the Thermal Load in a T-Junction Pipe", **Proceedings of M&M2010 Material Mechanics Conference (Japan Society of Mechanical Engineers)**, October, 2010, Nagaoka, Japan, pp.1205-1207.

Acknowledgements

First and foremost, I would like to express my heartfelt gratitude to my thesis advisor, Prof. Naoto Kasahara for his invaluable advice during the preparation of this thesis and his careful guidance during the thermal striping collaborative research, which had been performed between JGC Corporation and Prof. Kasahara's lab for 4 years since April 2009. This thesis is a part of the collaborative research outcome. Prof. Kasahara provided me with a precious chance of joining the thermal fatigue research project under the NRA-sponsored JAMPSS program during the collaborative research. Also, it was very impressive that Prof. Kasahara provided not only the guidance of specialized knowledge and research but also the moral education to his lab members. I have benefitted much from these.

At the same time, I am also very grateful to the Board of Thesis Examiners members, Prof. Koshizuka, Prof. Okamoto, Prof. Demachi and Prof. Sakai for their invaluable advice and comments, which were very helpful for the completion of my thesis.

I deeply appreciate Prof. Demachi and Dr. Suzuki in Prof. Kasahara's lab, for their invaluable advice, comments and help during this collaborative research. Furthermore, the collaborative research with Prof. Kasahara's lab was not only fruitful but also very joyful. This is attributed to the help from every lab member, open discussions, and formation of a relaxed multicultural atmosphere in the lab. I would like to deeply appreciate every lab member during the collaborative research.

During the collaborative research with Prof. Kasahara's lab, I joined the thermal fatigue research project under the NRA-sponsored JAMPSS program. I would also like to express my deep gratitude to the thermal fatigue research committee members, especially Dr. A. Nakamura and Dr. Y. Utanohara (INSS), Dr. M. Tanaka (JAEA), Mr. H. Nakamura (CTC) and Mr. H. Ikeda (Toshiba), for their joyful collaboration, helpful discussions and advice.

Moreover, I want to deeply appreciate my colleagues and co-researchers, Mr. Kanamaru (now the leader of the Structural Analysis and CFD Group (SCG)), and Mr. Frith for their collaboration and support. Also, I would like to deeply appreciate Chief Engineer, Dr. Sato in EN Technology Center (ENT), JGC Corporation, for his support in realizing the collaborative research with Prof. Kasahara's lab, and invaluable advice and comments on thermal striping research. Furthermore, I would like to express my heartfelt gratitude to ENT Senior Manager, Dr. Hosoya and Manager, Mr. Kado for their constant support. In addition, I would also like to express my deep appreciation to all the SCG members for their support and encouragement.

Finally, I want to express my heartfelt thanks to my wife, Zhuxi, my son, Yang and other family members for their understanding, support and encouragement.